DEVELOPMENT AND APPLICATION OF NOVEL FIBRE-BASED LASER SOURCES FOR COHERENT RAMAN BASED BIO-IMAGING

Krzysztof P. Herdzik

SUPERVISORS

Prof. David J. Richardson

Dr. Jonathan H.V. Price

Prof. Sumeet Mahajan

Dedicated

To Gdynia, my city

To Poland, my country

To Europe, my homeland

Print name: Krzysztof Paweł Herdzik
Title of thesis: DEVELOPMENT AND APPLICATION OF NOVEL FIBER-BASED LASER SOURCES FOR COHERENT RAMAN BASED BIO-IMAGING

I declare that this thesis and the work presented in it is my own and has been generated by me as the result of my own original research.

I confirm that:

1. This work was done wholly or mainly while in candidature for a research degree at this University;

2. Where any part of this thesis has previously been submitted for a degree or any other qualification at this University or any other institution, this has been clearly stated;

3. Where I have consulted the published work of others, this is always clearly attributed;

4. Where I have quoted from the work of others, the source is always given. With the exception of such quotations, this thesis is entirely my own work;

5. I have acknowledged all main sources of help;

6. Where the thesis is based on work done by myself jointly with others, I have made clear exactly what was done by others and what I have contributed myself;

7. Parts of this work have been published as:

a) *''Multimodal spectral focusing CARS and SFG microscopy with a tailored coherent continuum from a microstructured fiber'',* K. Herdzik et al., Appl. Phys. B 126, 84 (2020), DOI: 10.1007/s00340-020-7406-6

b) *''Comparison of SC Fibers for fs Ti:Sapphire Based Hyperspectral CARS Microscopy''*, K. Herdzik et al., conference paper for European CLEO, Munich 2019, DOI: 10.1109/CLEOE-EQEC.2019.8873199

Signed electronically 17/10/2020

Krzysztof Herdzik

Abbreviations

ANDi- All Normal (negative) DIspersion

CARS- Coherent Anti-Stokes Raman Scattering

CGCRI- Central Glass and Ceramic Research Institute

IDRI- Intensity Dependent Refractive Index

IfLS- Institute for Life Sciences

fs- femtosecond

M-CARS- Multiplex CARS

MOPA- Master Oscillator Power Amplifier

OPO- Optical Parametric Amplifier

ORC- Optoelectronic Research Centre

ps- picosecond

TPACS- Two-Photon Absorption Cross Section

TPEF- Two Photon Excited Fluorescence

SC- Supercontinuum

SHG- Second Harmonic Generation

SPM- Self Phase Modulation

SRG- Stimulated Raman Loss

SRL- Stimulated Raman Gain

SRS- Stimulated Raman Scattering

XPM- Cross Phase Modulation

ZDW- Zero Dispersion Wavelength

ABSTRACT

Early and accurate detection of cancerous tissue is key to increasing patient survival rates. Spontaneous Raman spectroscopy could potentially provide a useful imaging tool for that purpose, as it is a vibrational finger-printing technique with a highly chemically specific signal. It is, however, characterised by a very low signal-to-noise ratio which makes it unsuitable for rapid microscopic imaging as required in biomedical applications. This can be overcome by using nonlinear techniques based on Raman scattering such as Coherent Anti-Stokes Raman Scattering (CARS) and Stimulated Raman Scattering (SRS), making them increasingly applicable to medical diagnostic imaging.

Coherent Raman Scattering (CRS) techniques require synchronized, multi-wavelength laser sources. Such sources can be provided by fibre-based supercontinuum (SC) generation, which allows multiple vibration frequencies to be addressed and thus helps increase chemical specificity. However, commercially available fibre-based broadband sources currently have quite low Power Spectral Density (PSD) levels. In this work, coherent SC generation from fibres has been investigated in order to overcome this problem. The investigation has been conducted across wide parameter space for two fibre types: a Central Glass and Ceramic Research Institute (CGCRI) manufactured fibre (exhibiting both normal and anomalous dispersion), and a NKT-1050-NEG1 fibre (All Normal Dispersion [ANDi] profile). The SC output from the fibres was then compared with results from a NKT femtoWHITE CARS fibre. It was found that for the CGCRI fibre an optimal length of 17 mm gave a tailored spectral profile spread over 200 nm. The NKT ANDi fibre on the other hand resulted in 200 nm broadening after propagation along 85 mm of fibre. The spectra from both fibres had higher PSD in the required spectral ranges than the femtoWHITE CARS fibre.

Using NKT ANDI output, a hyperspectral CARS imaging system has been developed, and successfully used for imaging of animal tissue also enabling other concurrent modalities, such as SHG or TPEF. The acquisition time for these images was comparable or better than sources

currently used by the bioimaging community, at the same time providing significant technological improvements, stepping closer toward ultimate goal of the use of fibre-based sources in clinical environment.

To investigate potential low-cost multi extension to that setup, enabling efficient fs multi-photon TPEF imaging over a broadband range, the Supercontinuum has been compressed using a prism-based system, using the intensity of the Second Harmonic Generation (SHG) generated with $BaTiO_2$ crystal as a metric of compression of the SC pulse. The registered signal intensity has been compared with the benchmark of a Ti:Sapph 100 fs laser oscillator.

In total, therefore, a robust fibre-based broadband laser source has been designed, optimised, characterized and applied for hyperspectral, multimodal imaging.

ACKNOWLEDGMENTS

I would like to extend thanks to my supervisors: Jonathan Hugh Vaughnan Price, PhD, for all of his advice based on his wide knowledge and skills; Professor Sumeet Mahajan, for all his mentoring support and useful comments on the direction of the research; Professor David J. Richardson, for his keen supervision and taking consideration in both my and the project's best interest.

I also wish to express my gratitude to Kostas Bourdakos, PhD, for his continuous help throughout my project, which would not come to fruition if not for him, and to all of the other members of Molecular BioPhotonics and Imaging group for creating a very pleasant, yet fully science-focused work environment.

Special thanks to Barbara and Dariusz Herdzik, for equipping me with necessary skills to progress in my life- which brought me here, and- I hope-will bring me even further. I am incredibly lucky to have them as my parents.

And big thank you to: my friends from my High School years, for still being a part of my life; my friends and colleagues from Gdansk University of Technology, always ready to change plans in order to meet with me during one of my short stays in Poland; fellow foreigners at the University of Southampton who, like me, immigrated to UK from a different country, for providing me with sort of family during these trying times of adjusting to PhD life; level 2 gremlins, level 3 Normies, and the other denizens of Building 85, for all the fun stuff we went through, out of which the Golden Summer 2018 was the greatest.

And a special word of appreciation to anyone reading these words, as I hope there will be many, but I know there will be only a few.

TABLE OF CONTENTS

1. INTRODUCTION

It is strongly believed that a large number of deaths caused by cancer could be avoided by better means of detecting tumours early, as there is strong correlation between early diagnosis of cancer and survival rate [1]. Provision of rapid and precise diagnostic techniques could thus help increase worldwide survival rates. Moreover, surgical procedures could be simplified if instead of the current method of diagnosis based on histopathological examination, requiring arduous sample preparation [2] [3], cancer tissue could instead be imaged and identified live and *in vivo* (using endoscopes or surgical microscopes). Therefore, improved patient outcomes could be facilitated through label-free diagnostic techniques e.g. novel nonlinear microscopy-based imaging methodologies.

Out of those, Coherent Raman Scattering (CRS) techniques have been attracting the most attention because of their chemical specificity and high sensitivity, enabling robust identification of cancer tissue and its video-rate imaging [4]. CARS and Stimulated Raman Loss / Stimulated Raman Gain (SRL/SRG) spectroscopy are the most common implementations of CRS. CARS is the most straightforward method to implement, but is plagued by the presence of an inherent Non-Resonant Background (NRB). SRS is free from this limitation, but the technical complexity of homodyne-based detection system required for SRS is an important obstacle for practical implementations.

Existing commercial lasers, which are needed for CARS/SRS, come with their associated optical tables, chillers and high maintenance requirements. They provide exquisite images in bio-science labs, but the cost and complexity limits their uptake and they are unsuitable for translation to, e.g., National Health Service (NHS) surgeries. Hence, there is an ever-growing interest in fibre laser systems and their application for biomedical imaging to overcome the limitations of solid-state picosecond (ps) and femtosecond (fs) lasers [5]. This project aimed to fulfil this need for new laser by using fs pump lasers to generate tailored bandwidth and hence high PSD supercontinuum in optimised, small-core microstructured optical fibres.

During the course of the project, three types of fibre have been investigated and, on basis of the findings a fibre-based SC source has been created, with optimum spectral and temporal output for bioimaging using nonlinear laser microscopy. Finally, that source has been successfully used for imaging of biological samples in CARS and supporting modalities, including SHG or TPEF. The main biological sample was a bioimaging golden-standard: adipose tissue, acquired from a dissected mouse.

TPEF and SHG signals increase strongly with peak power, and are thus optimised by pumping with transform-limited fs pulses, whereas SF-CARS require chirped, ps pulses. For enhancing the signal with the TPEF and SHG modalities prism-based compression was attempted and resulting signal strength was quantified using collagen rich mouse tail and the signal from SHG crystals.

The structure of the thesis is as follows. Chapter 2 provides the state of the art from the literature and the background theory for the non-linear optics, imaging techniques and fibre optics. Chapter 3 shows the results from the comparison between different fibres tested vs the set of source parameters needed for biomedical imaging applications. Chapter 4 shows the results of applying our customised fibre laser source for label-free bio-imaging. Chapter 5 shows the results of compression of SC generated through 1055 nm and 800 nm seeds. Chapter 6 sums up the work conducted, and chapter 7 provides future perspectives for development of the research completed here.

2. THEORY AND LITERATURE REVIEW

2.1 Limitations of current microscopy techniques

The ability to differentiate between healthy and diseased tissue is a powerful tool in medicine for diagnostics and in biology for fundamental research. A number of existing imaging techniques, both conventional and nonlinear, have been used for diagnoses and the structural investigation of changes in cells and tissue. Considering the nonlinear bio-imaging field as a whole, the majority of laser-based microscopy is based on Two Photon Excited Fluorescence (TPEF) [6] or Second Harmonic Generation (SHG) [1] to provide image contrast (signal). The former is often carried out with natural (e.g. green fluorescent protein - GFP) fluorophores in genetically modified cells or transgenic organisms, or with exogenous artificial stains applied to the samples. One can sometimes make use of natural fluorophores existing within cells and tissues. These often exhibit absorption in the UV-blue spectral region, which makes two-photon excited auto-fluorescence feasible while using NIR lasers. SHG, which is a special case of sum frequency generation (SFG), allows imaging of non-centrosymmetric structures such as collagen in tissues in a label-free manner along with TPEF. Both of these techniques have been in use from much earlier than other nonlinear techniques. They require high peak powers, which for bioimaging are obtained by short duration pulsed laser sources. That results in a large installed base of fs Ti:Sapphire lasers. The ability to extend the capability of such lasers to chemical specific label-free imaging techniques such as CARS without the purchase of expensive devices could offer significant benefits by providing the bio-imaging community the access to new, chemically selective contrast mechanisms where the use of GFP (or similar fluorescent proteins) or stains is not appropriate, and, ultimately – would enable medical diagnostics. However, while label-free imaging with non-linear techniques is steadily gaining ground, fluorescence microscopy (using fluorescent labels as tags/markers) remains the most common imaging technique in biology and medicine.

2.1.1 Fluorescence-based biomedical imaging

Fluorescence imaging most often utilizes emission from chromophoric labels to impart specificity [6], as many cellular components, such as lipids, are not fluorescent [7]. Therefore, different fluorophores are required to label each molecule or structure of interest [7]. The toxicity of these fluorophores, their potential disruptive influence on processes and functions of cells and tissue as well as the complicated labelling process [8] makes it practically impossible to apply this technique in living humans, so it is unsuitable for clinical in-vivo live imaging. Furthermore, in order to achieve z-resolved 3D imaging using conventional single-photon fluorescence, one needs an expensive confocal microscope [9].

2.1.2 Label-free techniques

Label-free techniques overcome the issues related to the requirement for external fluorophores but very few of them provide native structural or chemical contrast. An example of such a label-free imaging modality is Magnetic Resonance Imaging (MRI), widely applied in medical imaging. It involves changing gradient of Magnetic Field, which penetrates the tissue, making it possible to image different structural components.

While MRI in some conditions can image with μm [10], and even nm resolution [11] [12], and can achieve tissue penetration depths in range of mm or more it does not provide the required chemical or structural specificity that is needed for objective and early diagnosis of diseases such as cancer. Hence, interest in label-free techniques with high chemical specificity, like in vibrational techniques capable of identifying molecular bonds, has been growing. Out of these, InfraRed (IR) absorption spectroscopy identifies these bonds well, however it is not well suited for biological applications [13], mainly due to strong absorption by water [14]. This limitation however, is not present for Raman scattering which is an alternative vibrational spectroscopy technique.

2.2 Spontaneous Raman Spectroscopy

Raman spectroscopy is a promising label-free technique that has found increasing biomedical applications over the last few decades. One of the reasons for its suitability for bio-imaging is its lack of sensitivity to water. Raman spectra provide a vibrational fingerprint of a molecule or a substance. Hence, Raman spectroscopy has been extensively used in chemical and material sciences for characterisation. A wide range of molecules and materials have been studied, which makes this method a good choice for identification and fingerprinting of substances in a sample [15]. This has also been extended and applied to disease identification and to distinguish between different types of cancer [4].

The characterisation ability based on such Raman 'fingerprinting' can be linked to the way in which light interacts with the sample in the process of Raman scattering. An incoming electric field can lose (Stokes process) or gain (anti-Stokes process) energy to or from a vibrational level, respectively. This is caused by excitation to (or deexcitation from) higher vibrational levels of molecules (see Figure 1). An incident photon loses or gains energy corresponding to one of vibrational modes of molecule. This causes the energy shift in the emitted photon with respect to incident light - so-called Stokes and anti-Stokes shifts respectively [16].

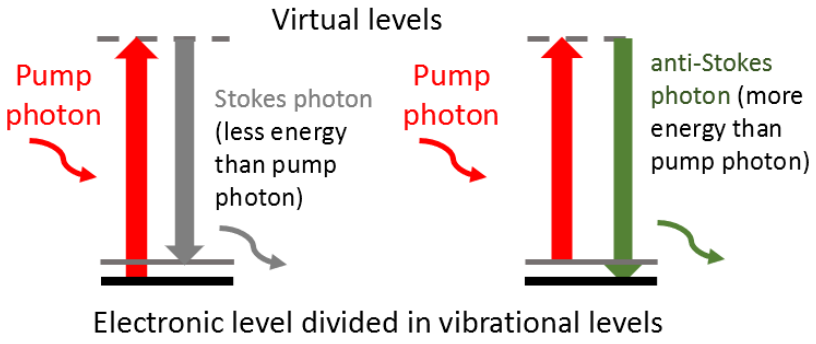

Figure 1 – Raman scattering energy level diagram. It shows the transitions involved in Stokes and anti-Stokes Raman scattering processes and the energy transfer in each of them.

The Raman effect can be understood in a simple way by assuming that a molecule causing the scattering can be presented as an electron-nucleus system. Firstly, one needs to consider the electric dipole moment created when the incident electric field interacts with the electron-nucleus system as presented in Eq. (1) . It shows the dependence of electric dipole (μ) on the polarizability of the electron cloud (α) and the externally applied electric field (E).

$$\mu(t) = \alpha(t)E(t) \tag{1}$$

One can expand the polarizability into a Taylor series where α_0 is the polarizability in absence of molecular vibrations and $\left(\frac{\partial\alpha}{\partial Q}\right)_0$ is the polarizability change along the nuclear coordinate Q(t) (Eq. (2)).

$$\alpha(t) = \alpha_0 + \left(\frac{\partial\alpha}{\partial Q}\right)_0 Q(t) + \ldots \tag{2}$$

One can use the approximation of a classical oscillator in order to describe the nuclear motion, *Q(t),* around the equilibrium in eq. (3), where ω_v is the nuclear resonance frequency. This harmonic potential approximation is valid only for electromagnetic fields that are small in comparison with the field binding the electron cloud to the molecule nuclei.

$$Q(t) = 2Q_0\, cos(\,\omega_v t + \varphi) = Q_0[e^{i\omega_v t + i\varphi} + e^{-i\omega_v t - i\varphi}] \tag{3}$$

For an incoming radiation field, $E(t) = Ae^{i\omega_1 t}$+c.c., where ω_1 is the angular frequency of light, and *A* is the amplitude of electric field, the dipole moment can be written as in eq. (4). In this expression $\alpha_0 Ae^{-i\omega_v t}$ describes Rayleigh scattering while $e^{-i(\omega_1-\omega_v)t}$ and $e^{-i(\omega_1+\omega_v)t}$ describe the Stokes-shifted and the anti-Stokes-shifted Raman scattering contributions, respectively.

$$\mu(t) = \alpha_0 Ae^{-i\omega_v t} + A\left(\frac{\partial\alpha}{\partial Q}\right)_0 Q_0([e^{-i(\omega_1-\omega_v)t+i\varphi} + e^{-i(\omega_1+\omega_v)t-i\varphi}] + c.c. \tag{4}$$

Considering the outgoing energy flux, caused by the oscillation of that dipole, one can calculate the total intensity of emission of Stokes-shifted light at frequency ω_s. It's described by eq. (5) [17].

$$I(\omega_s) = \frac{{\omega_s}^4}{12\pi\varepsilon_0 c^3} Q_0^2 |A|^2 \left|\frac{\partial\alpha}{\partial Q}\right|^2 \tag{5}$$

This relationship conveys both the dependence of Raman intensities on polarizability changes as well as the strong frequency (ω^4) dependence.

Although excellent at chemical fingerprinting, the efficiency of Raman scattering is very low (only 1 in 10^7 incident photons is Stokes scattered) [18]. That is insufficient for most biomedical applications especially those which require rapid imaging. There is therefore an increasing interest in coherent Raman imaging techniques like SRS and CARS. In these techniques the Raman radiation is no longer a sum of all incoherent scatterers – they instead cause the Raman scattering to be a coherent process throughout the excitation volume. Due

to constructive interference between the oscillators, Coherent Raman processes enhance the Raman signal from the sample by at least 2 [19] and up to 8 orders of magnitude [20], so that live label-free imaging of bio-molecules becomes possible.

2.3 CARS Theory

2.3.1 CRS overview

CRS encompasses all imaging and spectroscopy modalities that use signal enhancement due to vibrational resonance in Raman scattering. The first of the two main applications of this genre is Stimulated Raman Spectroscopy (SRS), also known as Stimulated Raman Loss/Gain (SRL/SRG). That is an imaging modality that overcomes some of the disadvantages of other implementations of CRS, such as the presence of a Non-Resonant Background (NRB) convoluted with the resonant signal in CARS. However, the necessity of using a homodyne detection system causes technical difficulties when extending the capabilities of currently used nonlinear imaging microscopy systems to include SRS.

Another version of CRS, called coherent anti-Stokes Raman scattering (CARS), is easier to implement since signals at new frequencies, well separated from the excitation, are detected. Spectroscopy and microscopy with CARS had been shown as early as 1965 [21] and 1982 [22], respectively. Due largely to the progress in laser technology over the last two decades CARS is emerging as a valuable imaging tool in biomedical research [23] as it provides label-free, non-destructive, non-invasive contrast and enables 3D imaging due to its inherent z-sectioning capability [24] [25]. CARS has provided important insights in neurology [26], cancer and tumour metastasis [27], embryonic and skeletal stem cells [28] [29], as well as in a range of in-vivo studies [30] [31] [20].

This thesis work is primarily focused worked on sources for CARS. Hence, in the following sections the fundamentals, background theory and applications of CARS are described.

2.3.2 CARS fundamentals

For the following derivation, one has to assume that the vibrational movement of two nuclei can be approximated as a damped harmonic oscillator along their internuclear axis.

In order to drive the vibration, the oscillator is subject to two incident electromagnetic plane waves of the form $E_j(t) = A_j e^{-i\omega_j t}$+*c.c.* (j=1,2). It is assumed that both of the incoming fields are characterized by frequencies higher than nuclear resonant frequency ω_v, so that the nuclear oscillator cannot be driven by those fundamental fields. According to the Born-Oppenheimer approximation only the electron cloud will follow the incident fields [32]. Moreover, if the intensity of the fields is sufficient, they can cause nonlinear electron motion at combination frequencies, including $\Omega = \omega_1 - \omega_2$. Under these conditions, one can describe the force exerted on the oscillator by the combined electrical fields (eq. (6)). This force is dependent on the frequency difference, and amplitudes of the incoming electromagnetic fields as well as the coupling of polarizability with the nuclear coordinates $\frac{\partial \alpha}{\partial Q}$ [17].

$$F(t) = \left(\frac{\partial \alpha}{\partial Q}\right)_0 [A_1 A_2^* e^{-i(\Omega)t} + c.c.] \tag{6}$$

The equation of motion of the nuclear oscillator under the influence of an external driving force can be written in the form of eq. (7). It contains the damping constant, δ that encapsulates the velocity-dependent damping of the oscillatory movement, and the reduced mass of the oscillator *m*.

$$\frac{d^2Q(t)}{dt^2} + 2\delta \frac{dQ(t)}{dt} + \omega_v^2 Q(t) = \frac{F(t)}{m} \tag{7}$$

The time-varying displacement can be found analytically using the following equation (8).

$$Q(t) = Q(\Omega)e^{-i(\Omega)t} + c.c. \tag{8}$$

wherein the amplitude of this nuclear motion is given by the following relationship (9)

$$Q(\Omega) = \frac{1}{m}\left(\frac{\partial\alpha}{\partial Q}\right)_0 \frac{A_1 A_2^*}{\omega_\nu^2 - \Omega^2 - 2i\Omega\delta} \tag{9}$$

The nuclear mode is driven by the interplay of incident fields. The amplitude of the vibrational motion depends on the amplitudes of the applied light fields and the coupling of nuclear coordinate to the electronic polarizability $\left(\frac{\partial\alpha}{\partial Q}\right)_0$. The magnitude of the vibration depends also on the difference between the effective driving frequency Ω and the inherent resonance frequency of the molecular oscillator ω_ν. The amplitude of this oscillatory motion is the largest, when the frequency Ω matches the oscillator's resonance frequency.

As seen through equation (1), that same electronic polarizability is influencing the response of the material to the incident electric field. That, in turn, can be demonstrated in large scales through macroscopic polarisation which can be regarded as the sum of N electric dipoles per unit volume as shown by equation (10)

$$P(t) = N\mu(t) \tag{10}$$

To consider large scale response of a material to the incoming radiation, we consider two different electric fields *E₁* and *E₂* incident onto a material. Then, based on eq. (1), (2) one can write the expression for polarisation as below in equation (11)

$$P(t) = N[\alpha_0 + \left(\frac{\partial\alpha}{\partial Q}\right)_0 Q(t)]\{E_1(t) + E_2(t)\} \tag{11}$$

This equation shows how the incident fields cause both linear polarisation $P_L(t) = N\alpha_0\{E_1(t) + E_2(t)\}$ and the nonlinear polarisation $P_{NL}(t) = N\left(\frac{\partial\alpha}{\partial Q}\right)_0 Q(t)\{E_1(t) + E_2(t)\}$.

The nonlinear polarisation can be further presented based on eq. (8) through equation (12).

$$P_{NL}(t) = P(\omega_{cs})e^{-i\omega_{cs}t} + P(\omega_1)e^{-i\omega_1 t} + P(\omega_2)e^{-i\omega_2 t} + P(\omega_{as})e^{-i\omega_{as}t} + c.c. \tag{12}$$

There, the incident fields are of ω_1 (also known henceforth as pump) and ω_2 (also known henceforth as Stokes) frequencies, and anti-Stokes and coherent Stokes scattered frequencies are ω_{as}= ω_1+$\omega_v$and ω_{cs}=ω_1-ω_v respectively. One should not confuse the coherent Stokes frequency ω_{cs}, that characterizes the scattering of excited dipole, with the Stokes excitation frequency ω_2.

All of these components oscillate with different amplitudes [33]. Thus, based on (9) amplitude of polarisation at the Anti-Stokes frequency is given by (13)

$$P(\omega_{as}) = \frac{N}{m}\left(\frac{\partial\alpha}{\partial Q}\right)_0^2 \frac{1}{\omega_v^2 - \Omega^2 - 2i\Omega\delta} A_1^2 A_2^* = 6\varepsilon_0\chi_{NL}(\Omega)A_1^2A_2^* \tag{13}$$

Because the oscillating polarisation is responsible for the emitted electric field oscillating at the same frequency, one can present the intensity of that electric field through equation (14).

$$I(\omega_{as}) = \frac{\epsilon_0 c}{2}|A_{as}|^2 \tag{14}$$

The magnitude of A_{as} is directly proportional to nonlinear polarizability $P(\omega_{as})$ and to the intensities of the incident fields I_1 and I_2 as per the following eq. (15).

$$I(\omega_{as}) \propto |\chi_{NL}|^2 I_1^2 I_2 \tag{15}$$

For most of the cases, the only significant component of nonlinear susceptibility χ_{NL} is the third order susceptibility, the lowest order nonlinear interaction in the structurally amorphous materials.

As one can see, the magnitudes of both spontaneous and coherent Raman effects depend on the movement of nucleus via coupling of electronic coordinates to the nuclear coordinates, which gives both of the effects their chemical specificity. However, amplitude is not the only aspect of these processes that needs to be considered for obtaining strong emission for nonlinear imaging, as explained below.

2.3.3 Phase-matching requirements for CARS imaging

In the previous section the amplitude of Anti-Stokes signals and their dependence on the incoming electric field was described. However, we next need to analyse the influence of phase on the process. In the formalism that follows, we consider a four wave mixing process. One has to take into account however, that for most of the applications two of the incoming waves are degenerate: pump and probe being often at the same frequency.

In order for a Four Wave Mixing process to create a strong output signal, both energy and momentum conservation principles must hold. The energy conservation principle is presented as in (16).

$$E_{as} = E_{pump} - E_{stokes} + E_{probe} \text{->} \omega_{as} = \omega_{pump} - \omega_{stokes} + \omega_{probe} \qquad (16)$$

On the other hand, the momentum conservation principle for colinear CARS is given by (17).

$$k_{as} = k_{pump} - k_{stokes} + k_{probe} \qquad (17)$$

As $|k| = \frac{2\pi n}{\lambda}$ in a dispersive medium the dependence of refractive index of material on frequency causes a mismatch in length of the wave vectors (18), Figure 2.

$$\Delta k = \frac{2\pi n(\lambda_{anti-Stokes})}{\lambda_{anti-Stokes}} - \frac{2\pi n(\lambda_{probe})}{\lambda_{probe}} + \frac{2\pi n(\lambda_{Stokes})}{\lambda_{Stokes}} - \frac{2\pi n(\lambda_{pump})}{\lambda_{pump}} \quad (18)$$

In order to increase signal, the phase mismatch needs to be reduced as much as possible.

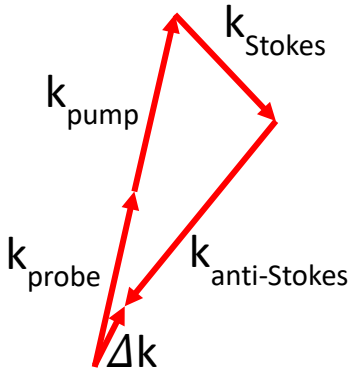

Figure 2 – Wavevector mismatch in CARS process [34]

However, in practical applications, this condition is relaxed in tight focusing conditions [35]. In the epi-direction, the condition for wave matching is fulfilled for small interaction lengths, comparable with CARS wavelength [36]. This is the case that applies to CARS microscopy in this thesis.

2.3.4 Nonresonant background

The previous sections outlined conditions for the generation of CARS signal. The CARS signal however, is inherently accompanied by a background due to electronic processes, that do not relate to the nuclear resonances (see Figure 3).

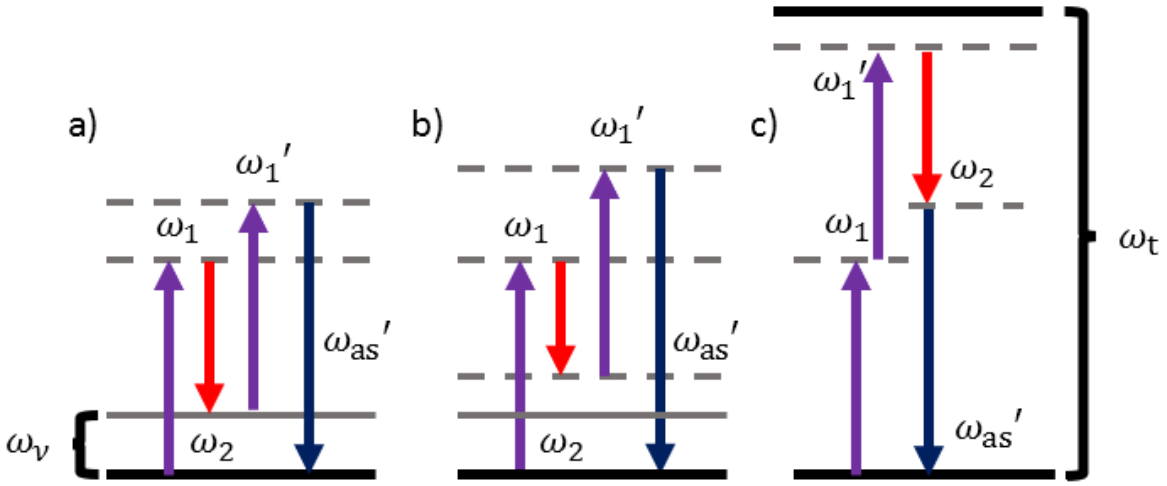

Figure 3 – Resonant (a), Non-Resonant (b) and Two Photon Excitation enhanced Non-Resonant (c) signal excitation

As stated at the end of chapter 2.3.2, in most of the applications the main part of the nonlinear susceptibility is the third order susceptibility. It's full form [37] [38] is presented in eq. (19), and to introduce additional quantities Γ_R and $\Gamma_t$connected to Raman and two-photon-absorption line-widths respectively, and A_R and $A_t$which are Raman and Two-Photon Absorption cross-sections respectively. The first term is responsible for emission of the coherent Raman signal. $\chi_{nr}^{(3)}$ is a contribution to non-resonant part of third-order susceptibility that relates to the non-resonant background, usually approximated as a frequency independent constant in the spectrally narrow measurement region [38]. The last term in eq. (19) is enhanced nonresonant contribution due to the two-photon electronic resonance.

$$\chi^{(3)} = \frac{A_R}{\omega_v - (\omega_1 - \omega_2) - i\Gamma_R} + \chi_{nr}^3 + \frac{A_t}{\omega_t - 2\omega_1 - i\Gamma_t} \qquad (19)$$

Here we see clearly that apart from the resonant, chemically characteristic component, polarisation dependent response of a material has also a nonresonant contribution. For diagram – see Figure 3 [37], where both excitation and emission of the signal is being presented.

Even though Non-Resonant Background is disadvantageous for spectral resolution and contrast, because of the convolution of NRB with resonant signal [39], it can provide the heterodyne amplification, often improving the strength of the signal over the detection threshold in all of the modalities described in section 2.4 below.

2.4 CARS imaging approaches

In this section the most common methods and the setups for CARS imaging are described.

2.4.1 Single-Frequency CARS

One of the simplest and earliest implementations of CARS for imaging was single-frequency CARS. It has certain advantages, like high resolution, good tunability in the given range and the existence of robust commercially developed system. However, the slow tuning speed of most current optical parametric oscillator (OPO) systems, not to mention capital and maintenance costs, or the low spectral power density in SC-based broadband CARS, means that while using these sources the acquisition of hyperspectral images can take hours [40].

All-fibre laser sources are being developed, that make it possible to generate synchronised ps output without the necessity of an OPO or a SC generating fibre, like the use of synchronized fibre-based oscillators [41]. However, tunability of these sources is still limited, and narrowband ps pulses do not make it possible to generate robust SHG or TPEF signals for multimodal imaging.

2.4.2 Broadband CARS approaches

Broadband CARS (BCARS) solutions use usually a broadband Stokes beam (as achieved e.g. through [42]), and a narrowband pump/probe beam providing high spectral resolution. However, as demonstrated e.g. in [43], doing that results in a suboptimal Power Spectral Density. That in turn makes the application difficult, because an SLM has to be used in order to optimally shape the pulse temporal profile at the focal point of the microscope. Also, the backward (epi-detected) CARS modality it gives inherently lower signal than forward

(transmission-detected) CARS. CARS requires coherent source (which precludes use of incoherent sources for multi-wavelength fluorescence like SuperK [44]), and one that provides spectrum with clearly defined polarisation (as pump and Stokes need to have polarisation aligned in respect to each other). These needs are addressed partially by the femtoWHITE CARS fibre: firstly, the output is highly coherent, as the generation occurs in the normal dispersion regime, and secondly, the depolarisation, although observable, is relatively low. However, the large broadening of output spectrum symmetrically around pump laser wavelength strongly decreases the overall power spectral density (PSD) within the required spectral range.

2.4.3 3-colour CARS

One of the ways in which BCARS has been implemented is the one adapted by the Cicerone group, where both a narrow and a broadband laser have been used for intra- and interpulse excitations [42] [45] [46] while using a photonic crystal fibre (PCF) as a source [47].

In conventional CARS, the nonlinear Raman response emission is at the anti-Stokes wavelength which is separated spectrally with a filter. Although technically a short wavelength pump and long wavelength Stokes are needed to excite the resonance from which a third short wavelength 'probe' pulse creates the output, the pump beam is typically also used as a probe to avoid unnecessary complication.

In 3-color CARS (used e.g. in [20] [46]), pump no longer is degenerate with the probe (see Figure 4). This complicates the setup, however it does also open the possibilities to remove NRB from the acquisitions [48], as per lower coherence time of NR-excited virtual states.

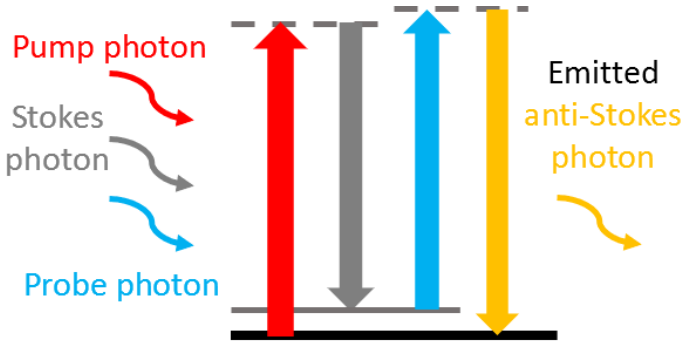

Figure 4 – Energy transfer between incoming photons and molecular energy levels in a 3-color CARS process with non-degenerate pump and probe

2.5 Advantages and disadvantages of CARS

CARS, most significantly, is a label-free technique, and does not require additional, (arduous) sample preparation. CARS enables the identification of compounds due to the extensive look-up library of Raman spectra of known molecules. The high signal to noise ratio allows for imaging of biological samples, and the ability to z-section a sample and isolate signals from different depths [23] enables the 3D resolved imaging of thick (clinically relevant) samples.

Another advantage of CARS imaging, due the use of pulsed lasers, it that it can be performed together with other modalities. This opens up the possibility of multimodal concurrent imaging capability and provides complementary information to CARS. The most prominent techniques which can be performed simultaneously with CARS are two-photon excited fluorescence (TPEF) and second harmonic generation (SHG). These techniques are described briefly in the next sections.

There are disadvantages and some of them are limited by the technological approaches [35]. These include the following:

1. Resonant signal emitted with nonresonant background

2. Amplitude of CARS measured only, without information about the phase (in most of the current modalities)

3. Signal is typically collected from just one anti-Stokes frequency, which is not sufficient for definitive fingerprinting

4 Complexity of setup and cost of two synchronized spectral sources

The physical limits, like the need for high peak power, became less limiting through introduction of turn-key sources of reliable, well-engineered ps pulsed laser. However the sophistication required, including large size of the currently used laser and OPO sources [33] prevents the technique being used widely.

2.6 Two Photon Excited Fluorescence

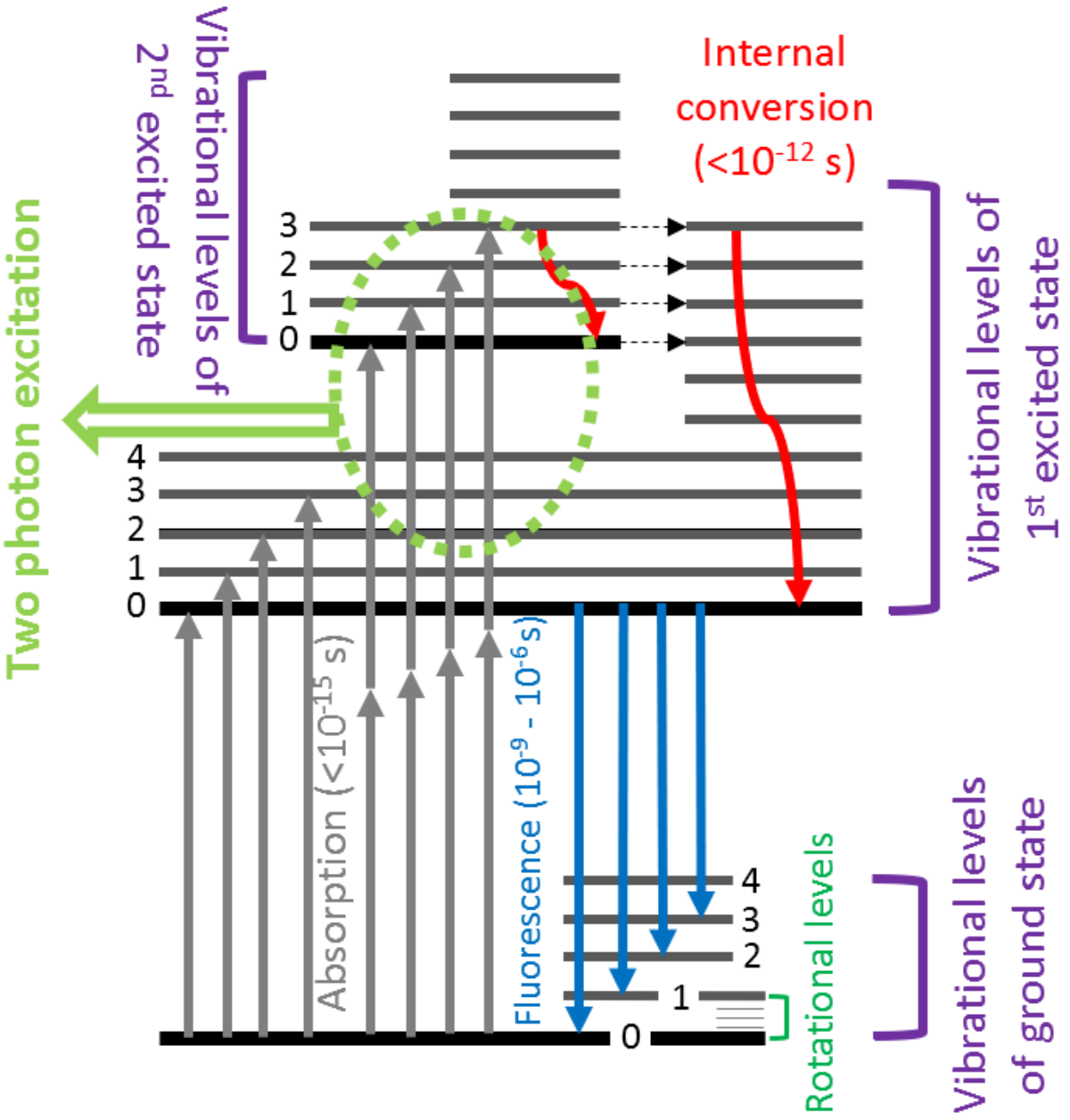

Figure 5 - Fluorescence excitation and emission process in the context of molecular energy levels – electronic (ground & 1st, 2nd excited), vibrational and rotational, showing the transitions of photons (red arrow) and the timescales of phenomena relevant to energy transfer across levels

Two photon fluorescence, occurs when two photons absorbed at the same time cause fluorescent (see Figure 5). The first photon absorbed raises the energy to a virtual state, which has a limited coherence time. In order for two photon absorption to occur, the second

absorption needs to take place within that coherence time. That limitation causes the process to be quadratically dependent on the intensity, such that the overwhelming majority of absorption (and associated emission) is contained to the focal point of a highly intense beam (typically from a pulsed laser source providing high peak power) [49]

The spatial resolution in dimensions parallel (R_{xy}) and orthogonal (R_z) is therefore limited by the numerical aperture of the objective [50]. λ_{em} is the emission wavelength, and NA is the Numerical Aperture of the objective used for detection.

$$R_{xy} = \frac{0.7 * \lambda_{em}}{NA} \quad (20)$$

$$R_z = \frac{2.3 * \lambda_{em}}{NA^2} \quad (21)$$

TPEF emission is typically implemented using 100 fs laser sources. If that is the case, then along with TPEF, sum frequency generation (SFG) can also be detected, provided that a multimodal detection setup is used.

2.7 Sum Frequency Generation

SFG is best known in its degenerate form, as Second Harmonic Generation (SHG), where both of the interacting incoming waves are of the same wavelength, which causes the frequency to double [51]. It is a second order nonlinear process, during which two photons, coincident at the sample, excite the molecule to higher energy level (see Figure 6). Because of that, the resultant signal is quadratically dependent on the incident power, which is similar to TPEF. Unlike TPEF however, SFG can be used as a structurally specific technique, because even-order nonlinear susceptibility tensors are zero in centrosymmetric or amorphous media, and the material needs to be anisotropic for it to be SHG- or SFG-active. The properties of second-order nonlinear susceptibility cause the material response to incident light to be dependent on its polarisation, so it is also possible to find out the properties of the tissue through a polarisation-sensitive measurement [52] [53].

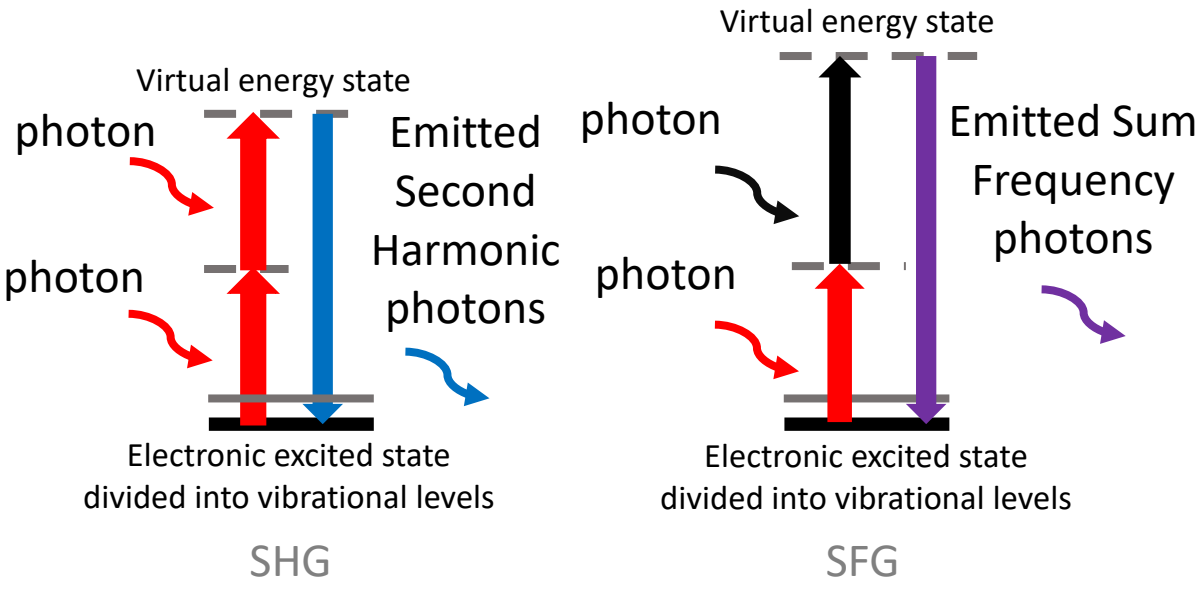

Figure 6 – Second Harmonic Generation (SHG) and Sum Frequency Generation (SFG) excitation, showing how in a multi-frequency setup either shorter or longer wavelength beam can excite Second Harmonic Generation, and how interaction within a multi-wavelength laser can excite Sum Frequency Generation. Both phenomena are due to the presence of virtual energy states, which require higher intensity pulses to provide signal levels generated from the real electronic transitions [54], used for fluorescence

2.8 Hyperspectral CARS & multimodal nonlinear imaging approaches

Even more robust characterization of the sample can be conducted when multiple vibrational levels are excited at the same time and this could be made feasible by applying a broadband pulse targeting multiple resonances, an approach called Multiplex CARS (M-CARS). The resulting signal would exhibit not one, but multiple Raman resonance peaks, as a range of vibrations would be excited. That means a Photomultiplier (often used in classical approach to CARS) would have to be exchanged for a spectrometer- or, alternatively, an array of Photomultipliers together with an appropriate filter setup would have to be used.

2.8.1 Spectrally Focused (SF) CARS

SF-CARS is one of the possible ways to achieve hyperspectral CARS. A route towards meeting the challenge of simultaneous application of hyperspectral CARS and multimodal imaging is

to use a broadband pulse which is then chirped and divided into long- and short-wavelength pulses which provide the pump and Stokes beams in so-called 'spectral-focusing CARS' (SF-CARS) [55]. However, short pulses are spectrally broad and hence can result in poor spectral resolution for CARS imaging.

Stretching the pulses linearly, such that different frequencies arrive sequentially in a controlled manner while ensuring that the instantaneous frequency difference (IFD or Ω) between the concurrent sections of the excitation pulses (pump and Stokes) is constant, means that a resolution similar to that for transform-limited ps pulses can be achieved [56] [55] [57] [58] [59]. In typical SF-CARS implementations, fs pulses have been stretched using dispersive glass elements [60] [57] and by equalizing the Group Delay Dispersion (GDD) between the pump and the Stokes by placing extra glass in the Stokes arm. The resolution of the system is dependent on the equalization of GDD which has been investigated analytically [56] [43]. The power requirements with SF-CARS are similar to single-frequency CARS, e.g. ~30 mW at the microscope focus is typically used with a high (>1) numerical aperture lens for bio-imaging due to photo-toxicity limitations.

Langbein et al. used the extreme bandwidth from a <10 fs Ti:Sa oscillator in a multimodal microscopy system targeting both the fingerprint region (1200-1800 cm^{-1}) and the high-wavenumber CH-stretch region (2800-3200cm^{-1}) [61] and later variations have used for example an offset probe to improve the signal to background ratio [58].

2.8.2 Broadband sources for CARS

One of the ways in which the need for two laser sources may be eliminated is the application of fibre-based SC [62].

As will be expanded upon later in section **2.9.10 Overview of currently used SC sources for spectroscopy and** imaging, there is a clear classification of possible sources for CARS. For single frequency applications, the narrowband lasers in connection with efficient OPA and OPO systems are very useful. More difficult is to generate broadband, coherent output, in

order to address many Raman resonances of the sample. One can get such characteristics only thorough transform-limited <10 fs laser oscillators or supercontinuum generating fibres.

To that end, methods using Stokes and pump carved from supercontinuum (SC) pulses generated in so-called microstructured fibres (MOFs) have been developed and are now widely used for SC pumped bioimaging [43] [63] [59] [64], and can avoid the need for a costly 10 fs oscillator.

SC generation was discovered in 1969, by R. Alfano and S. Shapiro. Since then, there has been a continuing interest in materials for SC generation and its applications [65].

2.9 Nonlinear fibre optics theory

In order to understand how SC is generated in fibres, and how fibre output parameters can be tailored for efficient bioimaging application we need to understand the way the high intensity light propagates within the fibre and interacts with the medium in a nonlinear way.

2.9.1 Introduction to pulse propagation

The propagation of light is described by Maxwell Equations [66]. In its simplest form, point source of radiation in a vacuum will generate a light wave that will propagate over a long distance, and the power per unit area will spread according to inverse of the square of the distance travelled. The speed of light in the vacuum is constant and equal to c. In any other medium, phase velocity of propagating light is reduced by factor 'n', known as the refractive index.

For any laser pulse, there is a fundamental limit between spectral width and the pulse width. For a flat phase (unchirped pulse) this limit is expressed through eq. (22)

$$\Delta v_p \tau_p \geq C_L \tag{22}$$

where v_p and τ_p are frequency and full-maximum half-width (FMHW) duration of the pulse, and C_L is the pulse shape-dependent constant (for Gaussian pulse = 0.441) [67].

2.9.2 Dispersion

One of the main effects influencing generation and propagation of SC pulses within a fibre is dispersion. In order to consider its effects in a medium in absence of nonlinear effects, one takes into account the input pulse of form [68] $e_{in} = E_{in}(\omega)e^{i\omega t}$. After propagation, the shape of output pulse in time domain is given by equation (23).

$$e_{out}(t) = \frac{1}{2\pi}\int d\omega\, E_{in}(\omega)e^{i\omega t}e^{i\beta(\omega)z} \tag{23}$$

The phase difference that arises because of pulse propagation in a medium over distance *z* is given by eq. (24).

$$-\beta(\omega)z = \varphi(\omega) \tag{24}$$

where $\beta(\omega)$ is a property of a given material typically described by a Taylor expansions as in eq. (25).

$$\begin{aligned}\beta(\omega) = \beta(\omega_0) + \left(\frac{\partial\beta}{\partial\omega}\right)_{\omega=\omega_0}(\omega-\omega_0) + \frac{1}{2}\left(\frac{\partial^2\beta}{\partial\omega^2}\right)_{\omega=\omega_0}(\omega-\omega_0)^2 \\ + \frac{1}{6}\left(\frac{\partial^3\beta}{\partial\omega^3}\right)_{\omega=\omega_0}(\omega-\omega_0)^3 + \cdots\end{aligned} \tag{25}$$

The dispersion D of fibre is given by eq. (26) where $\beta_2 = \left(\frac{\partial^2\beta}{\partial\omega^2}\right)_{\omega=\omega_0}$ is the Group Velocity Dispersion (GVD).

$$D = \frac{-2\pi c\beta_2}{\lambda^2} \tag{26}$$

The dispersion acting alone changes the temporal shape of the pulse.

2.9.3 GDD of chirped pulses

The dispersion causes phase distortion in the pulse. In the coordinate frame moving at the phase velocity of the pulse, the phase of the pulse (φ) is flat (described by a constant rather than function) if pulse is transform-limited- i.e. unchirped. The dispersion changes the relative

distance between different spectral components, as they propagate with different velocities. This can be quantified through Group Delay Dispersion (GDD), as described by eq. (27)

$$GDD(\omega) = \left(\frac{\partial^2 \varphi}{\partial \omega^2}\right)_{\omega=\omega_0} \tag{27}$$

As a convention, positive (negative) chirp means that frequency increases (decreases) with time. Positive chirp is caused by negative dispersion (D) of the material and vice versa. For most glasses the dispersion is negative in the visible region of the spectrum.

Using materials such as bulk glass one can achieve positive chirp (in the form of polynomial phase distortion), and through prisms and diffraction gratings one can achieve negative chirp (in a form of quadratic phase distortion with negative sign). Arbitrary chirp can be achieved using spatial light modulators.

2.9.4 Nonlinearity in fibres

The other important effect influencing pulse propagation is nonlinearity, already touched upon in chapter **2.3 CARS Theory**. For weak applied electric fields, which are small compared to atomic electric field strength 10^{11} V/m, the polarisation is directly proportional to applied electric field according to formula (28) taken from [17] where ε_0 is the electric permittivity in vacuum, χ is the susceptibility of the material and *E* is applied electric field.

$$P(t) = \varepsilon_0 \chi E(t) \tag{28}$$

For large electric fields, this relation stops being linear and higher-order corrections need to be introduced. This can be done by writing the polarisation in form of a power series as shown below [66]. $\chi^{(n)}$ is in this formalism a n+1 rank tensor, describing n-order correction to susceptibility (29).

$$P = \varepsilon_0[\chi^{(1)}E + \chi^{(2)}EE + \chi^{(3)}EEE + \ldots] \tag{29}$$

As described by Maxwell's equations, this induced polarisation is then treated as a source of a new, outgoing electric field radiated from the material [17].

Each of the terms in equation (29) is responsible for different range of nonlinear interactions.

- First-order susceptibility is responsible for the linear refractive index
- Second-order susceptibility is responsible for SHG, sum- and difference frequency generation as used in OPOs
- Third-order susceptibility is responsible for SPM, XPM Four-Wave Mixing phenomena and for CARS or SRL/SRG

The very low relative values of $\chi^{(2)}$ and $\chi^{(3)}$ limits the significance of higher-order susceptibilities to cases when high electric field intensities are present. Because of that, tight confinement of the electric field within a small volume has proved to be essential for SC generation. In a bulk material, the interaction length is limited by double the Rayleigh range-value known as ''confocal parameter''. However, in fibres SC generation is not subject to that limitation and nonlinear propagation is, in principle, limited mainly by absorption.

2.9.4a Autocorrelation

Second order nonlinearity may not contribute directly to SC generation, but it is invaluable for pulse characterisation through techniques such as SHG autocorrelation. It is the process of two pulses of the same frequency interacting in a SHG crystal. One of the pulses is continuously delayed in respect to the other with a pair of rotating mirrors, thereby sweeping the temporal delay of one pulse compared to the other. The output SHG emission intensity is therefore determined according to formula (30) [33]

$$I_{2\omega_0}(L) = \Gamma^2 I^2(\omega_0) L^2 sinc^2\left(\frac{\Delta kL}{2}\right) \tag{30}$$

where Γ is a material-dependent constant, *I* is the intensity of the incoming beam, ω_0 is the center frequency of the pulse, *L* is the length of interaction within the crystal, and the delta k is the phase mismatch between incident and generated beams.

2.9.4b Nonlinearity of amorphous materials

Third order susceptibility is not only relevant for CARS. For most of the amorphous materials, like the ones used for fibre manufacturing, the lowest order nonlinearity is governed by the third-order susceptibility $\chi^{(3)}$. This gives rise to an intensity dependent refractive index (IDRI) n_2, and hence the total refractive index $\tilde{n}$ is given by equation (31)

$$\tilde{n} = n_0 + n_2|E|^2 \tag{31}$$

where n_0 is a conventional refractive index described by equation (32)

$$n = \sqrt{\varepsilon_r \mu_r} \tag{32}$$

where ε_r and μ_r are the relative permittivity and permeability of the medium respectively [69].

and n_2 is given by eq. (33).

$$n_2 = \frac{3}{8n} Re(\chi^{(3)}_{xxxx}) \tag{33}$$

The most commonly applied material for fibre manufacturing is silica. In it, n_2 takes value approximately 2.5 x 10^{-16} cm^2/W [70].

The presence of a non-zero IDRI leads to the effects of Self-Phase Modulation (SPM) and Cross-Phase Modulation (XPM) that are fundamental for spectral broadening [71]. Self-Phase Modulation [72] occurs, when there is a large time derivative in phase change, caused by the nonlinear refractive index being intensity-dependent. This in turn causes the edges of the pulse to interact with the middle of the pulse, creating interference. SPM in the simplest form (solely considering the contribution of nonlinear refractive index to phase change) has been

described by [73] and [74]. SPM-facilitated spectral broadening for a Gaussian pulse is described by formula (34) [65]

$$\Delta\omega(z)_{max} = \frac{\omega_0}{2c} n_2 a_0^2 \left[\left. \frac{\partial F^2}{\partial \tau} \right|_{\tau_1} - \left. \frac{\partial F^2}{\partial \tau} \right|_{\tau_2} \right] z \tag{34}$$

where:

a_0 is the temporal amplitude of the pulse

n_2 is the nonlinear refractive index

ω_0 is the central frequency

z is the propagation distance

τ_1, τ_2 are the pulse envelope inflection points (points in which the second derivative of the pulse shape function is 0)

F is the time dependent pulse shape

For a Gaussian pulse shape that can be simplified as

$$\Delta\omega_{max} = \frac{\omega_0 n_2 a_0^2 z}{c\tau_0} \tag{35}$$

where the τ_0 is pulse FMHW duration.

2.9.5 Nonlinearity in the optical fibres

In order to excite nonlinear effects, which will finally result in our SC generation, the intensity has be or order of magnitude of the field binding electron to atom $E_a \approx 5 \times 10^{11}$ V/m [17] [75]. This can be achieved through enclosing light in the limited space with non-zero nonlinearity. The structure of an optical fibre creates a set of boundary conditions, the

solution to which causes the pulse launched into the fundamental mode not to spread laterally and thus spreading only in one direction- length of the fibre.

Whereas solid core fibres can be the source of high nonlinearity [76], the hollow core fibres can be efficiently used for guiding the generated light without considerable distortion to its spectral composition (low nonlinearity) and its temporal shape (low dispersion), as the pulse propagates mainly through the air (see [77] for investigation of confinement of the laser within the core surrounded by air) [78].

The guidance properties of the fibre can be modified by changing either its physical structure, as done in MOF, or by the choice of core/cladding material, which for all solid fibres is glass. In the step index fibre, light is limited to propagate along its axis by the difference of refractive indices between the core and the cladding. For microstructured fibre [79], the difference of refractive indices is bigger, as *n* of the cladding is decreased by the air holes. For Anti-Resonant (AR) fibre, the light propagates throughout the hollow core on the principle of resonance [80].

There are multiple possible pulse temporal profiles possible within the fibre. The easiest to analyse, and therefore most popular, is a Gaussian pulse shape described by relation [67]:

$$\varepsilon(t) \propto e^{\left[-1.4\left(\frac{t}{\tau_p}\right)^2\right]} \tag{36}$$

where $\varepsilon(t)$ is the intensity of the pulse, t is the time, and τ_p is the pulse FMHW duration.

SC generation in fibre has been first described by [81], but for couple of decades the development of fibre-generated SC did not progress much. The explosion of the publication connected to it after year 2000 (see Figure **7**) can be connected to two factors: availability of high power laser sources, and development of small core microstructured fibres, which can be tailored to purpose for a lot of applications (e.g. dispersion engineering, core size) [65] [82].

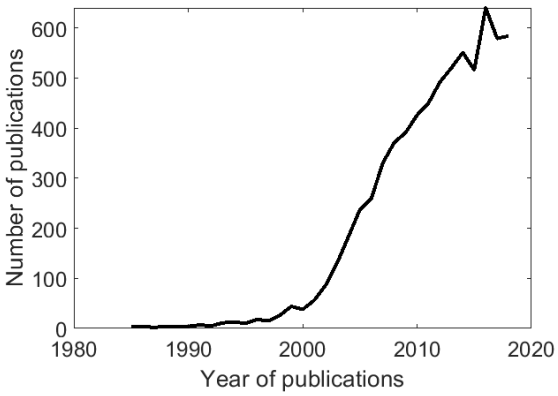

Figure 7 – Number of publications involving 'supercontinuum' across the last 30 years

Typical structure of PCF is presented in Figure 8 [83]. Parameter *D* is the core size, parameter *d* is the diameter of capillaries from which cladding consists, and Λ is the separation of capillaries in the cladding.

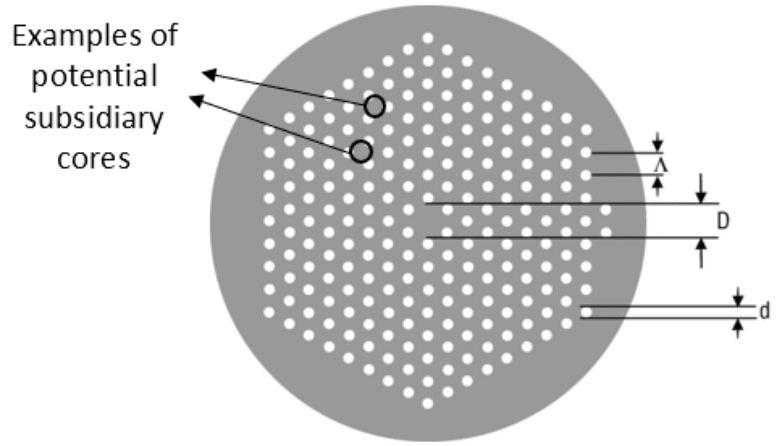

Figure 8- Photonic Crystal Fibre cross-section

These parameters are significant for SC generation – it had been found, that small Λ and large d/Λ cause the Minimum Dispersion Wavelength (MDW) to be in the visible regime, and if Λ is large and d/Λ is small, it shifts it into infrared [84]. One has to also consider, that only for d/Λ ratio smaller than 0.4 the fibre will be single-mode [85], which is the most

efficient way of SC excitation because of tight confinement. Moreover, the dispersion curve also can be significantly modified by changing D, as pictured on Figure 9.

It has to be noted, that thanks to these tailoring properties PCF fibres have significant advantage over step index fibres manufactured out of silica or other materials- one can achieve zero dispersion at lower wavelength than the material the fibre is made of (e.g. in case of silica, even <500 nm ZDW have been demonstrated, and the bulk silica ZDW is ca. 1300 nm) [86].

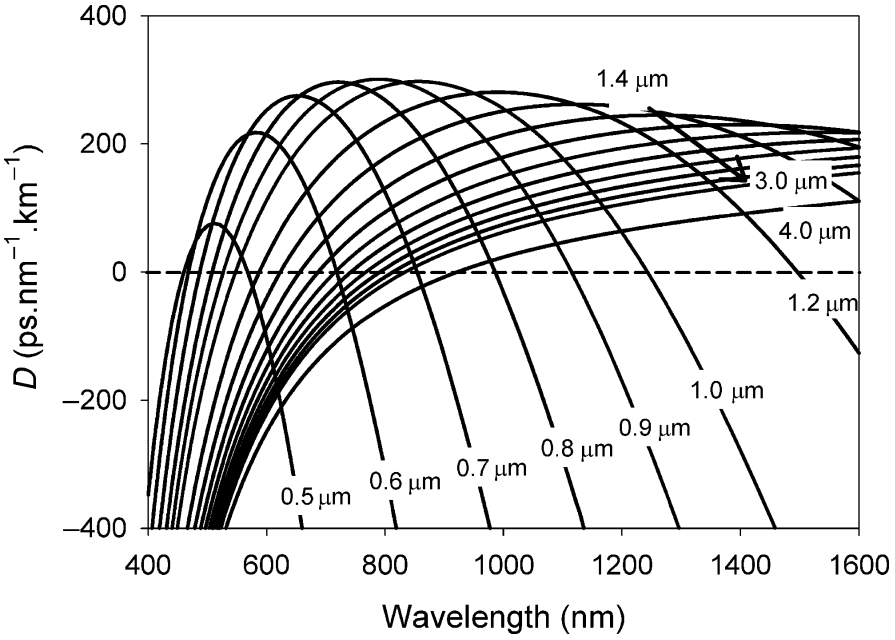

Figure 9 - Dispersion curves for different core sizes for otherwise same parameters of PCF [87]

This has found confirmation in the investigation of spectral broadening in the subsidiary cores (see also Figure 8) – i.e. coupling of the light in the silica strands [88]. It has been also confirmed by the investigation of output spectra out of CGCRI fibres in this thesis, as shown on Figure 10. Visible components of the spectrum pumped with 800 nm can be seen on Figure 11.

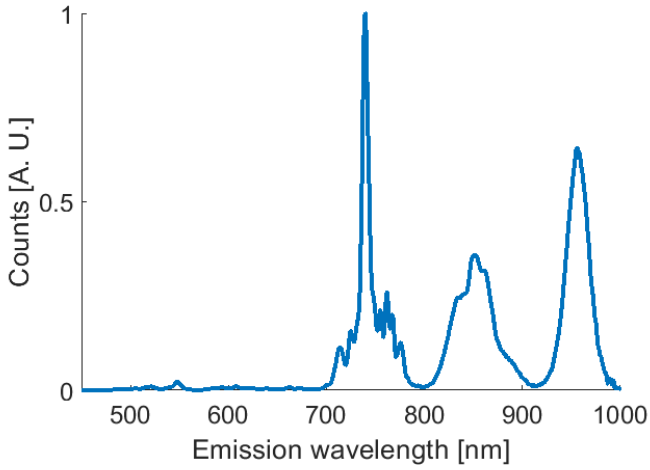

Figure 10 – Spectrum registered after pump laser coupled into subsidiary cores

Figure 11 - Extensive spectral broadening in the subsidiary cores

One of the properties of the fibres is the numerical aperture (NA), which in silica step index fibres is given by equation:

$$NA = \sqrt{n_{core}^2 - n_{clad}^2} \tag{37}$$

The NA determines acceptance angle of the fibre, and therefore puts constraint on the free space optics used to couple the light into fibre. For PCF fibres calculation needs to be

conducted to determine the NA, which is outside the scope of this work, but can be found e.g. in [89].

2.9.6 Influence on the spectral output of fibre parameters

As already introduced above, both nonlinearity and dispersion [90] can be modified in a PCF via its structure. Nonlinearity can be modified by engineering appropriate Mode Field Diameter by core size, and the dispersion can be modified by designing optimal microstructure exhibiting appropriate effective refractive index. The tight mode confinement in the PCFs used in this research increases γ and hence increases rate of spectral broadening, so that the benefit of the chosen structures is not confined solely to their dispersion properties.

Four-Wave Mixing mechanism is enhanced in proximity of Zero/Minimum Dispersion Wavelength, which is the principle which is used to tailor the output spectral shape through fibre parameters in some commercial products (e.g. femtoWHITE) .

In order to produce coherent SC one needs to either use a ZDW fibre in the anomalous regime, that is shorter than the soliton fission length [91] or to use an ANDi fibre, which is also limited-by a wavebreaking length- although this constraint is not as serious as the former.

The principle of wavebreaking is as follows- the peak of the pulse experiences higher nonlinear refractive index, so it slows down, and the edges of the pulse start to overlap in time with the center of the pulse- and different frequencies arriving at the same time at the given z of the fibre start to interact with each other, creating new wavelengths and causing rise to sidebands in the SPM-broadened spectrum [92], showing that the process is a degenerate four-wave mixing [93].

Formula (38) describes the distance, after which the wavebreaking occurs.

$$z_{OWB} = T_0 \sqrt{\frac{\gamma P_0}{|\beta_2|}} \tag{38}$$

And the associated bandwidth, to which the pulse grows at this point is shown in eq. (39)

$$|\omega_{SPM}(z_{OWB})-\omega_0|_{max} \propto \sqrt{\frac{\gamma P_0}{|\beta_2|}} \tag{39}$$

An example of pure Four Wave Mixing within the optical fibre is given in [94], where a ps pump and Stokes pulses recombine for an anti-Stokes emission.

2.9.7 Pulse propagation theory

The propagation of the pulse in a passive optical fibre is usually described using an simplification of Maxwell Equations, namely the Nonlinear Schrödinger Equation (NLSE), shown in one of the forms as eq. (40), where α describes the losses, and A is the amplitude of the electric field.

$$i\frac{\partial A}{\partial z}+\frac{i\alpha}{2}A-\frac{\beta_2}{2}\frac{\partial^2 A}{\partial T^2}+\gamma|A|^2A=0 \tag{40}$$

It describes the evolution of pulse in time vs. propagation distance.

The NLSE does not, except in special cases, have analytic solutions and hence in this work it has been solved numerically to optimize the parameters of SC spectra. The pulse in the numerical form computed through MatLab simulation from [95] has been applied. The Runge Kutta method has been applied, in which the fibre along which the pulse propagates has been divided into finite elements. Then the propagation of the pulse described by the GNLSE is conducted from one element to the other.

2.9.8 Characteristics of the broadband laser source.

For the optimum fibre SC source for CARS, which requires a high coherence input, the following dispersion characteristics have been determined [65]:

1. The fibre should demonstrate all-normal dispersion profile, that is flat and convex, in order to achieve robust SC generation in the normal dispersion regime
2. The Wavelength of Minimum Dispersion value should be close to 0 (preferably between -30 and -10 ps/nm*km), and the dispersion profile should be as flat as possible around that value.
3. Output bandwidth depends on the pulse duration and peak power, but the fibre length should be chosen according to the wavebreaking length

The determination as where to separate the output SC in order to target the intended range of wavenumbers for CARS needs to be supported by simulation, determining range of accessible wavenumbers for different divisions. This will be different for each fibre and pump laser considered. A broad spectrum is necessary to target 3000 cm^{-1}, but spreads the energy more, especially considering the almost flat-top character of spectra produced by the wavebreaking, the PSD decreases unless significant power increases for the seed pulse can be used (and additionally there are polarisation concerns).

2.9.10 Overview of currently used SC sources for spectroscopy and imaging

For optimal image quality, spectral power should not be extensively spectrally spread. The most biologically relevant range is 500-3000 cm^{-1} [46]. Therefore, SC making it possible to image in full range has been of particular interest [43] [96]. Currently used systems achieve down to 100 ms CARS acquisition rates per pixel with recognizable CARS signal, providing 10 cm^{-1} spectral resolution [97].

The issue with widely available SC sources of high power ('White Laser Light') is firstly, the distribution across the bandwidth of 800 nm or more [98], and secondly, the shape of the pulse in time domain becomes disturbed very often by soliton fission [91] causing the output to be of low coherence and hard to compress.

First issue causes inefficient excitation- only fraction of generated power overlaps with region of interest for excitation of Raman resonances. This causes the majority of power to be

wasted. Second issue limits the flexibility in compressing the pulse to desired temporal width this seems to be confirmed by the results of research detailed in [99].

Some researchers have shown that the SC generation through short fibre pieces could be used for a possible source of smooth SC [100] [101]. Analysis of SC tailoring in respect to its application in time-resolved CARS investigation has been conducted [102], but it is only a theoretical consideration on tailoring the SC through changing the structure of the fibre.

For CARS, the pump source has to produce ps or chirped to ps to provide optimum resolution in bio-samples. It has to be coherent throughout the spectrum, so that the frequencies can generate Four Wave Mixing within the investigated sample. The spectral shape needs to provide the necessary wavelengths concentrated in the range of interest, so that the Power Spectral Density will be as high as it can for a given average power. Pump wavelength should be chosen, so that the generated spectrum will be in the range transmitted by commonly applied microscope optics within the transparency window of the sample, at the same time being close enough to Minimum / Zero Dispersion Wavelength so that enough broadening occurs. These parameters were used as a guide for the study presented in the first results chapter.

Different materials can be considered for fibre core. One of the novel designs gaining interests is Hollow Core fibre, but instead of air (providing limited nonlinearity) one uses highly nonlinear gas [103]. The other example of material which is considered for the fibres is chalcogenide glass, which exhibits much higher nonlinearity than silica. However, due to technological constraints of preform productions and fibre drawing silica-based fibres seem to be still the dominating SC-producing fibre. The current status of the options possible is summarised in Figure 12.

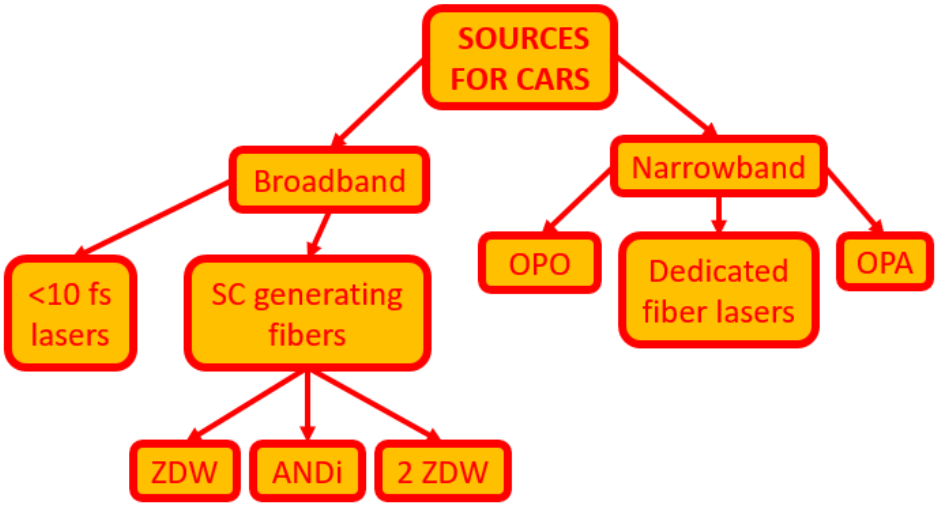

Figure 12 - Current general division between different fibre sources used for CARS purposes

The SC in fibres such as the femtoWHITE 800 fibre from NKT is ordinarily generated in the anomalous dispersion regime, where the soliton fission threshold, above which the SC pulse breaks into multiple pulses, limits the coherence and reduces the effectiveness for exciting CARS signals [104]. To address this, the NL-1.4.775-945 NKT fibre was introduced commercially as an NKT femtoWHITE CARS module [105]. It has two closely spaced Zero Dispersion Wavelengths (ZDW) to avoid extended propagation in the anomalous dispersion regime thereby increasing the coherence. Such modules have been used for tissue imaging, spectroscopy [43] and CARS for resonances both in the fingerprint region and the CH-stretch region [59]. However, the excessive broadening due to the dispersive and nonlinear properties of the fibre limits the useful power available for CARS signal generation, so it has been applied only for CARS detected in the forward (transmission) direction, rather than in the weaker epi-direction (with one notable exception [106]), as would be needed for thick and hence easily prepared clinical samples [107] [55] [37].

In ANDi fibre, the input short laser pulse undergoes broadening caused mainly by SPM, which results in broadened pulses with a high degree of coherence [108]. In a fibre with a ZDW such as CGCRI manufactured fibre tested in this research, the SC generation is product of both SPM

and FWM, soliton dynamics and dispersive effects [87], which enables broader spectra to be achieved for a given input pulse energy. However, the drawback when using seed pulse FMHW durations above ca. 10 fs is that soliton fission occurs [91] which is so sensitive to the seed pulse parameters that the output pulses are highly variable and possess a complex modulated phase profile. Therefore, in this research the CGCRI fibre length was matched to the soliton fission length to enable both rapid broadening and a highly coherent output pulse train. The use of a fibre with two closely spaced ZDWs (femtoWHITE CARS) leads to a coherent continuum by directly creating significant broadening to shorter and larger wavelength by coupling the soliton and dispersive wave across both ZDWs. It is, in some sense, a hybrid of ANDi and single ZDW approaches [109].

Another important parameter of a fibre-based source for imaging, is its pulse-to-pulse stability. As explained above, soliton fission, being a stochastic process, prevents the repeatability between pulses, therefore it would not provide signal for a consistent excitation across the whole grid through which the signal is being acquired (throughout all of the pixels of assembled image). The fact, that ANDi provides a low noise SC has been already confirmed [110]. Moreover, the requirement for coherence of the source is not key in TPF, but is of great importance for CARS generation, which precludes the use of incoherent laser sources like SuperK [44].

ANDi fibre has multiple advantages - pulses preserve a well defined phase shape, in contrast with conventional sources, which have one ZDW [111]. That leads to good compressibility of the pulses, as demonstrated by [112]. Uniform spectrum – unlike fibres with the Zero Dispersion Wavelength, where the solitons can interfere with each other, which results in fringes visible on spectral output [113], ANDi output is without any significant fine structure

2.9.11 Pulse measurements

During the optimisation of the source reported in this thesis, spectral and temporal characteristics of the pulse had to be controlled. For spectral measurements, both an Optical Spectrum Analyser (ANDOR) and Red Tide 650 spectrometers have been used. There is a

considerable difference in a way the spectrum is acquired- OSA scans across the dispersed spectrum with point intensity detector, whereas spectroscope acquires the data via the CCD matrix, which the spectrum is incident on. OSA gives absolute power within each of the parts of the spectrum, but the spectroscope has a responsivity curve, determined by the quantum efficiency of CCD for each of the colors. The spectroscope used an inverted Czerny-Turner design [114].

Autocorrelation measurement for narrowband pulse can be conducted as described in **2.9.4a Autocorrelation**, during which the SHG signal generated by the crystal is detected by a PMT, and the intensity autocorrelation trace is recorded by an oscilloscope.

For measuring the temporal profiles of broadband pulses, the same principles apply, however autocorrelation is more complicated to implement technically, because the spectral bandwidth is larger than the phase matching bandwidth of SHG crystals thick enough to generate SHG autocorrelation. More thorough techniques like FROG [115] need to be used, so that the pulse will be characterised temporally across its whole spectrum. The crystal dithering angle technique [115] can be used as a simplified method, however it may be challenging to use it in order to characterise pulse width at the focal point of a microscope, due to small working distances (<250 μm) of objectives involved as well as small focal volumes (sub-μm^3).

Another possible way of characterising of the temporal duration of the pulse is the recently considered interferometric autocorrelation of laser pulses based on two photon absorption [116], but application of it in experimental conditions proved too challenging within the limitations of the project.

2.9.12 Pulse duration in SF-CARS and SHG/SFG and chirp equalisation of pump vs Stokes

As described above, SF-CARS heavily depends on the properties of the chirped pulses, especially as in SF-CARS the hyperspectral capability is achieved by changing the temporal overlap (practically achieved by changing the delay) between the pump and the Stokes

pulses). The chirped pulse FMHW duration can be determined analytically for a Gaussian pulse, e.g. by formula (41) [117]

$$\tau = \sqrt{\tau_0^2 + \left(\frac{4\log(2)\,GDD}{\tau_0}\right)^2} \tag{41}$$

where τ_0 is transform limited pulse width, τ is chirped pulse FMHW duration and GDD is Group Delay Dispersion. That chirp is necessary for achieving good resolution, determined by eq. (42) [56] where τ_p is the FMHW duration of the pump pulse, and τ_s is the FMHW duration of the Stokes pulse.

$$\Delta\tilde{\nu} = \frac{2ln2}{\pi c}\sqrt{2\left(\tau_p^{-2} + \tau_s^{-2}\right)} \tag{42}$$

Using a spectrally broader pulse, and dividing it in the middle, would provide us with the highest effective power targeting vibrational levels- but only in a narrow range. Pump of small spectral breadth in comparison with Stokes provides us with scanning capabilities across a wider range of wavenumbers. One can see here an inherent conflict- the fs pulse provides high peak power, but low resolution. The ps pulse provides high resolution, but less contrast (even if it is a chirped fs pulse), on account of being order of magnitude lower intensity than fs pulse- and that means the signal is 3 orders of magnitude lower. This case has been discussed e.g. in [118].

For the figure below, an analysis of the targeted wavenumber range has been conducted. It has been assumed a Gaussian pulse shape and chirped pump and Stokes FMHW duration according to eq. (41). The resulting range of targeted wavenumbers across the pulse is presented in Figure **13**. Top Row: Broadband stretched pulses separated into Pump and Stokes segments with dichroic filter and shown with various relative delays applied. Bottom row: Frequency difference between Pump and Stokes shown vs. arrival time. (a-i) vs. (a-ii). Broad range of excited frequencies, i.e. poor CARS resolution, shown for unequally chirped Pump vs. Stokes when using part of spectrum far from the dichroic cut-frequency. (b) Narrow excitation band using same spectral regions as (a-i) but after GDD equalization.

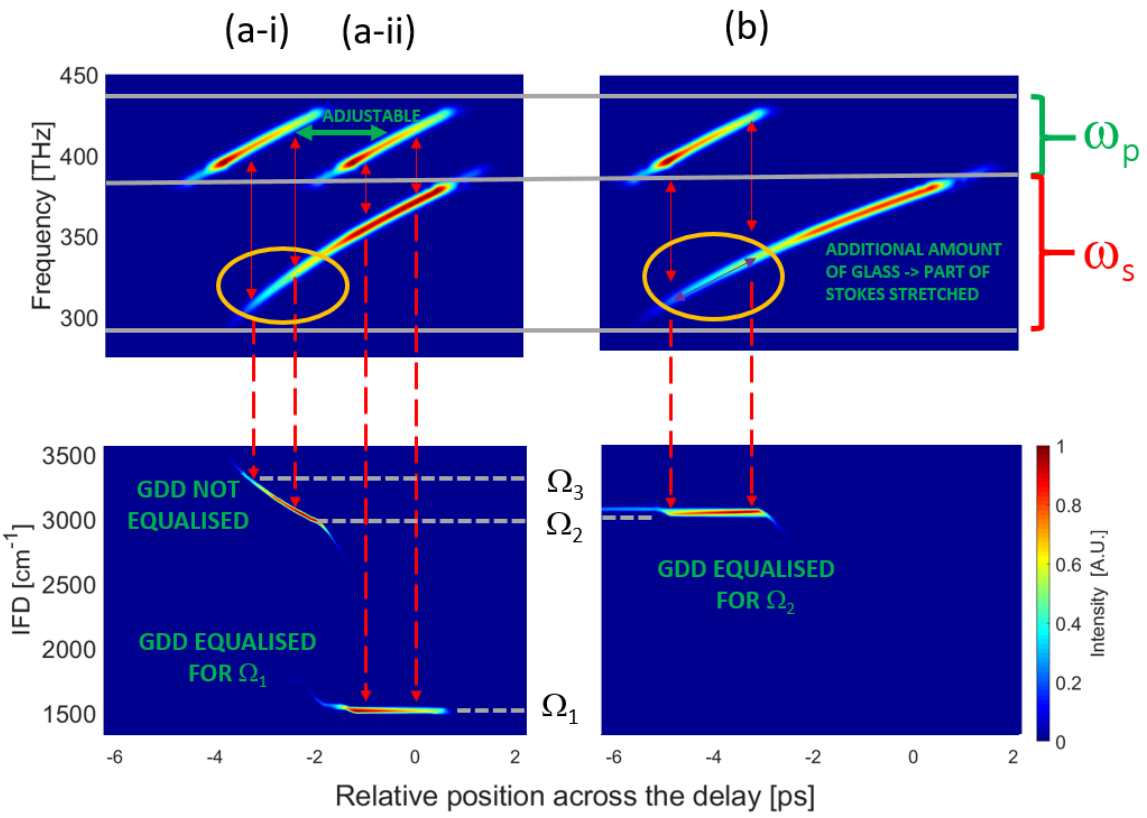

Figure 13- Principle of SF-CARS- Interaction between pump and Stokes showed for different time delays (upper left) and for different chirping conditions (upper right), and resulting range of excited vibrational levels (bottom)

Moreover, chirp inequality caused by dispersion necessitates the use of glass blocks to equalize the chirp of Stokes and pump. This is because unwanted but physically unavoidable, higher order dispersion influences the spectral resolution at different target instantaneous frequency differences (IFDs) (shown for IFDs: Ω_1, Ω_2 and Ω_3 in Figure **13** a-b). This means that the GDD needs to be equalized for each target resonance in turn for each image. The simulation data from our modelling shows what occurs when we create a relatively narrow-band pump (ω_P) and a broadband Stokes (ω_S), the Instantaneous Frequency Differences (IFDs, Ω) are narrow or broad depending on the GDD equalization. For different target vibrational frequencies or IFDs different amounts of GDD compensation is required for optimal spectral resolution across all parts of the Stokes spectrum. The spectral width of the excitation is shown in the lower row. As illustrated in (a-i), with insufficient GDD equalization

Raman peaks across the entire frequency range between Ω_2 and Ω_3 are being targeted; whereas in (a-ii) where GDD is more equal, a single resonance, Ω_1 is targeted. Similarly, in (b) if additional GDD equalization is applied to the low frequency part of the Stokes beam, then it is possible to achieve similar, good resolution for a vibrational frequency of Ω_2.

Therefore, continuous chirp regulation has been suggested e.g. using set of two prisms, with a regulated degree of insertion for at least one of them. However, to reduce the complication of such a setup, in the work presented in this thesis commercially available glass blocks were introduced to provide quasi-continuous chirp adjustment, which resulted in chirp equalising capabilities for CARS from fingerprint region and throughout the CH-stretching range.

2.10 Pulse compression approaches

On the other hand, for SHG and TPEF imaging, one needs a pulse that is characterised by narrow temporal shape and, therefore, high peak power. To that end, different pulse shaping approaches have been taken for imaging [119].

2.10.1 Prism compressor

The simplest of this setups is a prism compressor. It can compensate for the second-order phase distortion caused by a dispersive material [120] (Figure 14 [121]).

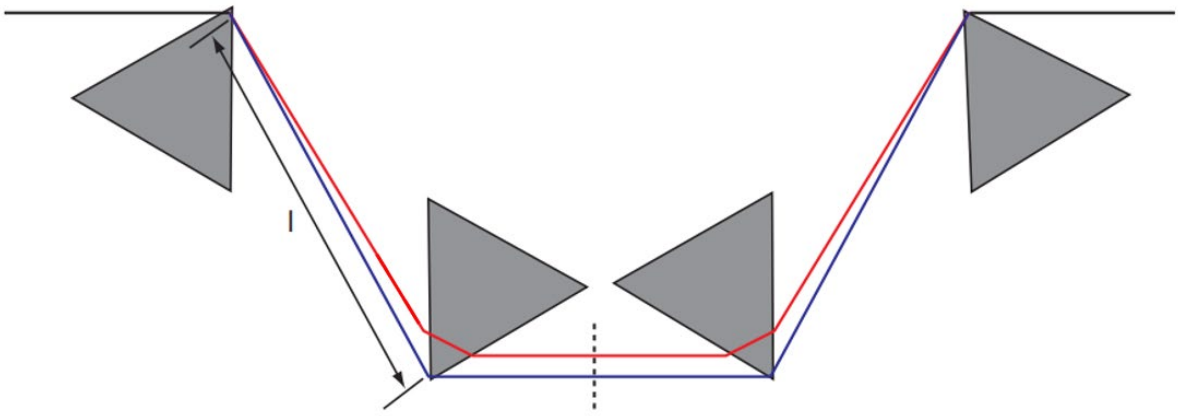

Figure 14 - Path difference between red and blue colors while propagating throughout 4 prism compression setup.

The disadvantage in using the prism compressor is that the third and higher order phase distortion may not be compensated as precisely as required.

2.10.2 Combined grating-prism compressor

Fork& Shank [120] suggested that further progress could be achieved by combining two compressive elements to create one grating-prism compressor. The third-order chirp was compensated because third order phase distortion caused by the grating based compressor is opposite in sign to the phase distortion caused by the prism compressor. The main disadvantage of this solution would be the transmission losses and costs of prisms and gratings would add up.

2.10.3 Chirped mirrors

Another solution in the form of chirped mirrors has been used in connection with SC compression [108]. They are limited however in amount of chirp they compensate (multiple reflections needed). Hence, for the one-off prototype development reported in this thesis chirped mirrors were too costly, but for a high volume end-product they may find applications.

2.11 Nonlinear imaging technology

2.11.1 Scanning techniques and focusing

After choosing the source and optimising the output, the next challenge lays in applying the source in the microscopy setup. Such a setup needs to have the ability to scan not only in spatial dimensions (x-y-z movements of either beam or the sample), but also in time (live cell acquisition) or throughout the molecular fingerprint (e. g. Raman vibrational spectrum). For these time-sensitive approaches, multiple optimisation mechanisms have been developed [122].

2.11.2 Detection techniques

For the efficient intensity-based detection of excited signal one can apply a range of detectors. For image detection most often used is a CCD detector. However, for purpose of detection in a scanning-based system, Electron Multiplying CCD (EMCCD) is often used. However, two types of detectors are being used in almost all of the systems- diode (often in the form of Avalanche PhotoDiode) or a Photomultiplier. PMT has narrower range, but higher sensitivity than APD.

2.11.3 Volume of interaction in nonlinear imaging

In order to achieve excitation of nonlinear effects significant enough for detection using above techniques, the power has to be concentrated within the small focal volume. That requires high-NA imaging objectives, which are often designed to work in either oil or water immersion.

However, focusing of a broadband spectrum creates problems. For every lens that is not achromatic, there is a certain chromatic dispersion. As one can prove e.g. through ABCD matrix method [123], there is a slight difference between how good is the beam collimated for different wavelengths. That doesn't cause considerable divergence for short distances, but for 4m length of our optical path it is already long enough to cause significant impact. The problem in nonlinear imaging is also the focusing properties of the objective itself. Most of the objectives used (including the ones used in our experiment) are achromatic- the set of the lenses within the objective corrects for chromatic aberration, therefore focusing all the wavelengths at the same point in the sample. That is a key requirement for spatial overlap of pump and Stokes- they will cause four wave mixing only if they are overlapped in the volume of a material with non-zero third-order susceptibility. It is also worth noting, that the volume from which the emission will occur, will be smaller for CARS than two-photon fluorescence because the of difference with the signal dependence on power (cubic for CARS, squared for Two Photon Fluorescence).

2.12 Summary

The presented review clearly points out, that in spite of the multiple available fibre sources in the market, there is still a potential for improvement in the field. The need for synchronized multi-frequency output can and is addressed by SC application, but a specifically tailored for purpose laser source would potentially address a lot of problems with current devices, including low power spectral density, making the imaging of thick, biologically relevant samples [55] [107] [124] [37] difficult.

3. CHARACTERISATION OF CONTINUUM-GENERATING FIBRES

Some of the plots presented here have been shown as part of the poster presented at the European CLEO 2019 [125].

3.1 Introduction

The construction of an optimal multimodal nonlinear imaging system needs to start with a choice of a suitable laser source. Optimisation of source output parameters is especially important for non-linear imaging techniques such as SF-CARS which ideally require high power spectral density combined with broadband pulses.

One of the options fulfilling this application is <10 fs laser oscillator. However, it would be quite cost-demanding to equip the current bioimaging laboratories with such a device. In order to avoid that budget requirement, one can use supercontinuum pulses generated in microstructured fibres (MOFs) at significantly lower cost and currently widely used for supercontinuum pumped bioimaging [43] [63] [59] [64]. Such modules have been used for tissue imaging, spectroscopy [43] and CARS for resonances both in the fingerprint region and the CH-stretch region [59]. However, the excessive broadening due to the dispersive and nonlinear properties of the fibre limits the useful power available for CARS signal generation (as shown on Figure 15 [126]). Therefore, the fibre has been applied predominantly for CARS that is detected in the forward (transmission) direction rather than in the backward (epi-) direction, in which signals are orders of magnitude weaker [107]. Epi-detection is needed for thick samples which are more clinically-relevant.

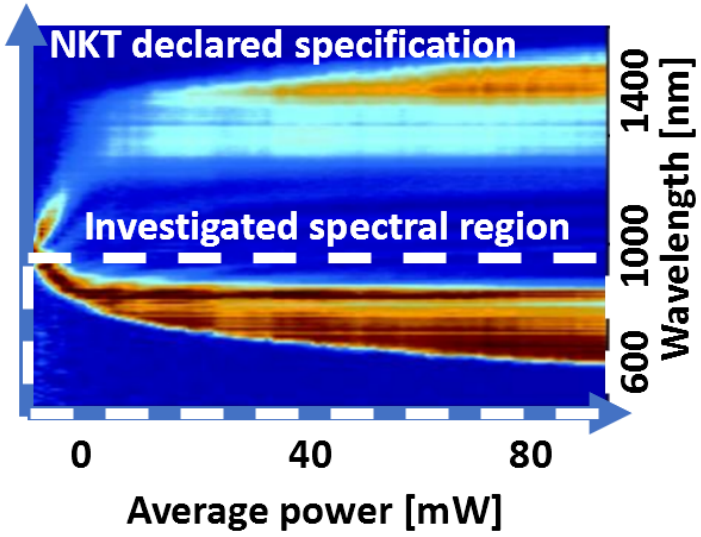

Figure 15 - femtoWHITE CARS emission spectrum (description of axes and marked region of interests from author). Emission for 40 fs pulses of 790 nm pump laser, colours marking PSD : orange – high, blue - low

The aim of the work in this chapter is to study and characterise different fibres and assess their suitability for non-linear imaging with SF-CARS. Computational studies analysing the influence of fibre source parameters on system capabilities have been explored e.g. by [102], but no experimental results of such review has been presented until now. Thus in this chapter, three fibres with different dispersion properties were studied through both simulations and experimental characterisation. A fibre with one ZDW, manufactured by CGCRI, another fibre without a ZDW (NKT-NEG-1) were compared with a fibre with two ZDWs (femtoWHITE CARS). The dispersion curves of the fibres are presented on Figure 16 (on basis of [126], [127], [128]). The fibres were investigated for influence of length, pump wavelength and pump power on the spectral and temporal characteristics of the output, in order to choose the optimal fibre source for SF-CARS imaging.

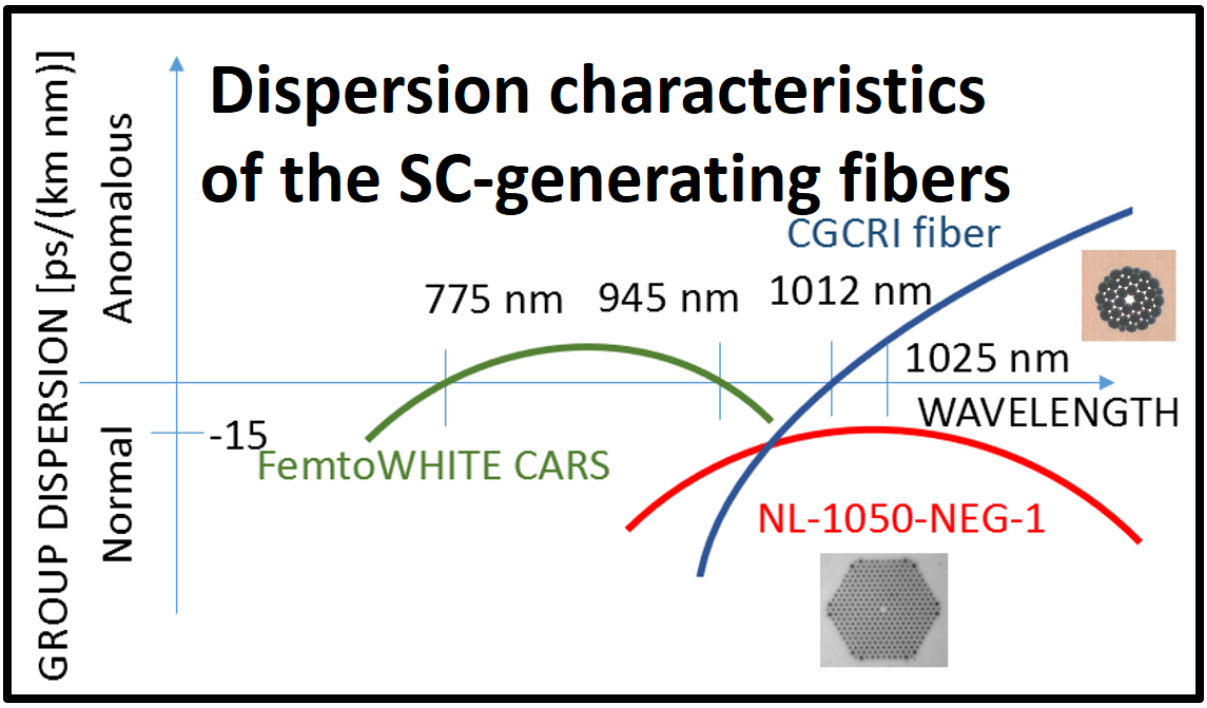

Figure 16 - Dispersion curves and cross section photographs of fibres used in the experiment (core size of CGCRI fibre 5.1 µm, NEG-1 2.3 µm)

3.2 Experimental details

Two separate fs laser sources were used for characterisation of fibre parameters- an Yb-based fibre laser source emitting 1055 nm and 90 fs Gaussian pulses [129], and a Mai Tai Coherent Inc. 130 fs laser tuned to 800 nm.

Preparation of pieces of fibre shorter than 10 cm can be difficult, as per minimum dimensions of fibres accepted in mechanical cleavers (>4 cm). Splicing of such a short piece can also require careful planning. However, when spliced to any longer, solid core fibre, the dispersion changes the temporal duration of broadband pulse considerably. This makes the free space setup preferable, until more advanced Hollow Core Fibres with transmission band across the range of interest will start to be commercially viable [80].

3.2.1 Methods of fibre characterisation

The spectra and temporal shape of pulses out of the fibres pumped with 1055 nm source has been analysed using the free space set-up shown in Figure **17**.

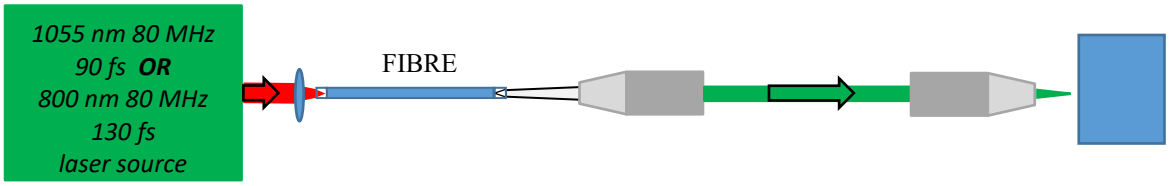

Figure 17- **Schematic of the Laboratory set-up for fibre characterisation for two different laser sources. The laser is focused with an 18 mm AR coated lens into the PCF fibre with protective end-caps, generating SC. The output is then collimated with an objective or lens (depending on the NA of the fibre in question) and focused with a second lens/objective into a detection setup (either spectroscope or autocorrelator – not shown). The fibre is positioned on a stage with 3 axes of movement.**

The fibre ends are protected by a flat endcap layer of glass to avoid degradation of the microstructure and to increase the damage threshold. The light from the fibre is collimated by an objective, and launched into another focusing objective, which in turn focuses the compressed SC into the detection setup.

3.2.2 Coupling power into the PCF

Spectral and temporal characteristics of the output are dependent on the power coupled into the fibre. However, due to the high peak powers used damage to the fibre core was observed. This was due to the low damage threshold of small core as observed in PCFs [130]. To remedy this, a glass end-cap was fused into the fibre tip was placed, which protected the entry facet of the fibre from ablation. The output facet needs to undergo the described end-capping procedure as well, in order to prevent water ingress into the microstructure.

As a result of the above measures the coupling efficiency was largely constant and degradation has not been observed over the course of our work. The coupling efficiency was consistent between 55% (2016) and 50% (2020). The short term coupling stability can be seen on Figure **18**, as compared with the power stability of MaiTai pump laser.

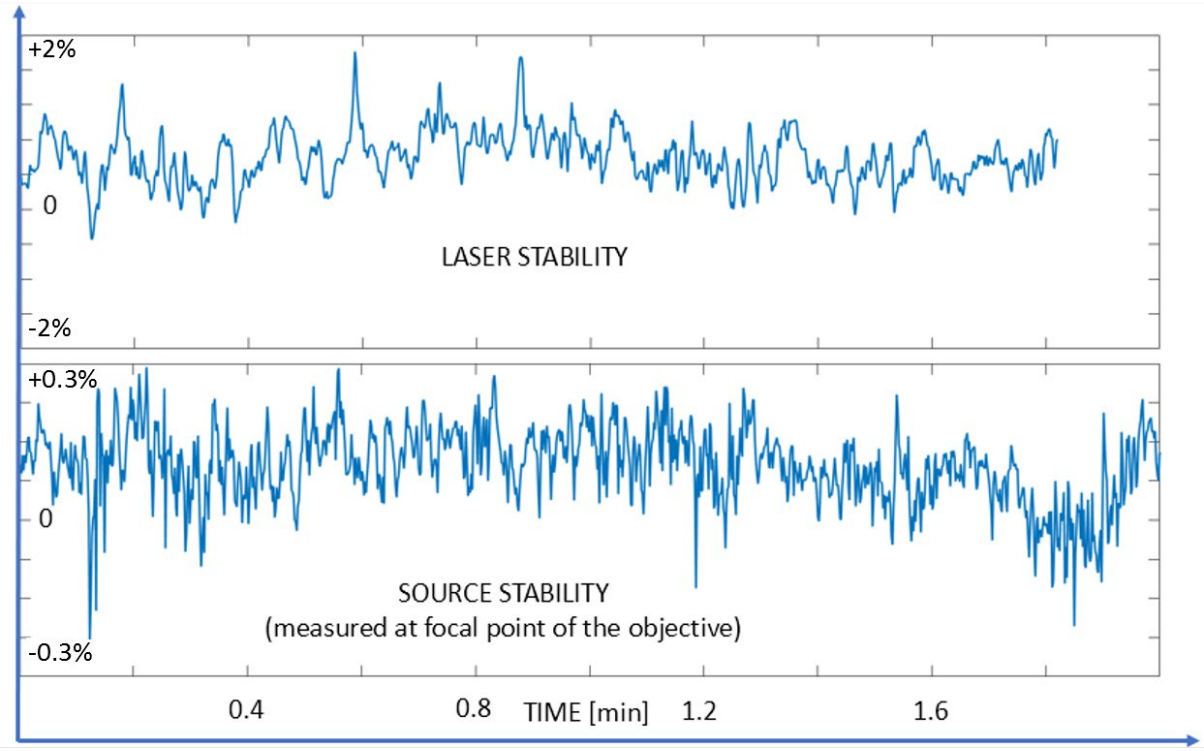

Figure 18- **Stability comparison between MaiTai (upper, 42 mW average power) and SC source (lower, 280 mW average power) over the course of 2 minutes- duration of time necessary in order to acquire an image**

One of another issues in coupling light, especially into short fibres, is the cladding – coupled light. Usually, it is removed quickly, as it propagates as an evanescent wave- the cladding – coating interface cannot support guidance over long distances. Moreover, bending of the fibre can further facilitate stripping away any light in the cladding. However, with short stripped fibre pieces the situation is different. Especially for these, the cladding modes can still be enclosed within the fibre through the index difference between the air and the cladding. As mentioned in 2.9.5 , that results into high numerical aperture, which makes the optimisation of coupling efficiency very hard- it is hard to tell apart the core guided light and the light in the cladding.

However, if one uses a high numerical aperture objective for collimation of the fibre output, it is possible to isolate the core guided light with an iris, and then coupling optimisation can finally be conducted, reaching coupling efficiencies similar to long lengths of fibre (50-60%).

3.2.3 Laser source characterisation

The seed used was the 1055 nm fibre laser described in detail in [129]. The spectrum and measurements of the pulse width of pulses emitted by this device are presented on Figure 19 and on Figure 20.

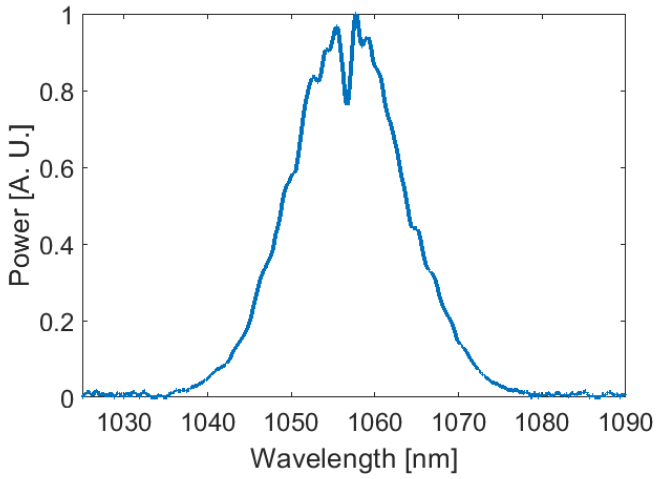

Figure 19 – Spectrum of 1055 nm pump laser as registered before the fibre

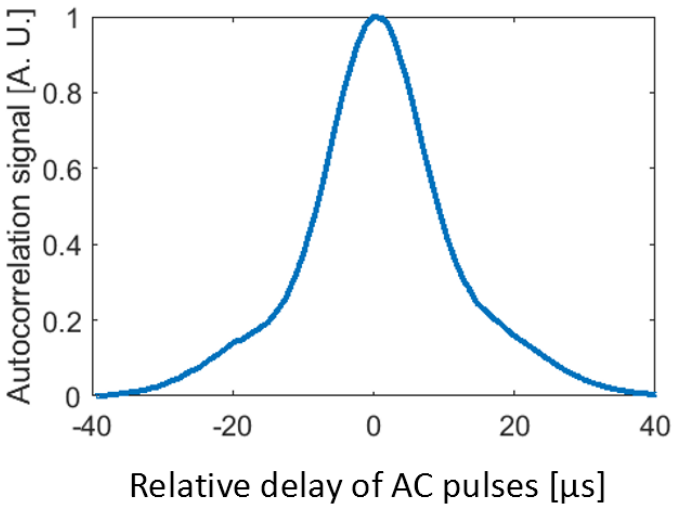

Figure 20 - Autocorrelation measurement of pulse width of 1055 nm laser, consistent with pulse width of 91 fs

The 800 nm source was a standard MaiTai Ti:Sa device, with 800 nm output and 130 fs pulse width at the output (as confirmed through spectroscopic and AC measurements).

3.3 Experimental and computational results

3.3.1 Simulation of fibre output

Before experiments have been conducted, simulations have been conducted using software based on [95], coded by the authors of mentioned publication to solve the Nonlinear Schrödinger Equation. It has been shown that the 300 nm broadening required to target both fingerprint region and lipid Raman resonances could be generated using short fibre piece and either of abovementioned sources. The simulations have been presented next to the experimental results for comparison.

3.3.2 ZDW (CGCRI) fibre with input at 1055 nm

The length of this fibre has to be adjusted taking into account the soliton fission length. Before the pulse propagates across this distance, the spectrum is internally coherent, but after the soliton splits, the coherence is lost, as discussed in **2.9.6 Influence on the spectral output.**

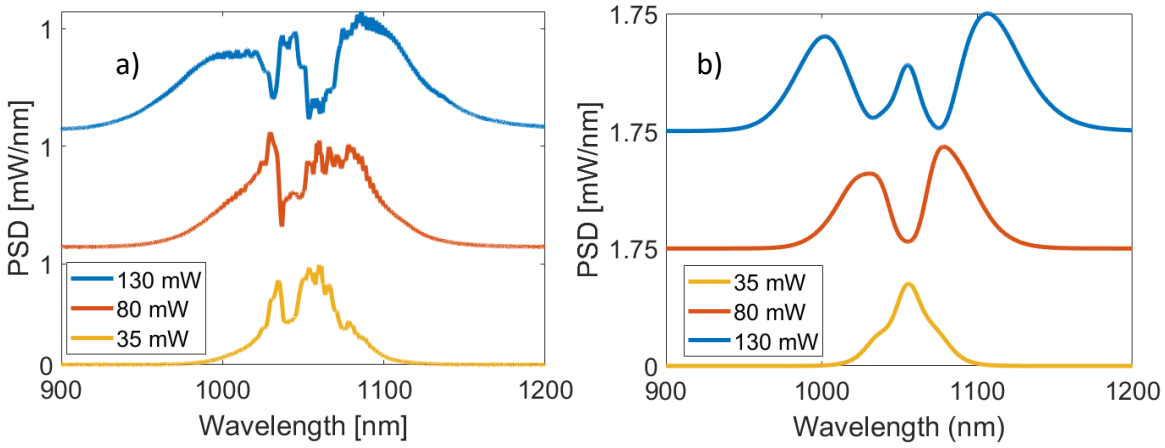

Figure 21 – Spectra of generated supercontinuum vs. simulations

Spectral intensity of generated SC (a) vs. simulated broadening for varied powers (b) in the fibre vs. of CGCRI fibre of 17 mm (Figure 21). The spectral width has been measured as 225 nm for the 130 mW input, and has been found within both the simulated result and the experiments.

The pulse out of the fibre is temporally narrow thanks to Soliton Compression phenomenon [131]. The optics placed on a path of the beam however introduce additional 800 fs^2 of quadratic phase distortion, causing the pulse to be broadened (see 2.9.3 GDD of chirped pulse), as seen on the result of simulation on Figure 22. Spectrum shown on Figure 23. That pulse duration and shape causes it to be difficult to autocorrelate, which can partly account for failed attempts for pulse duration measurements.

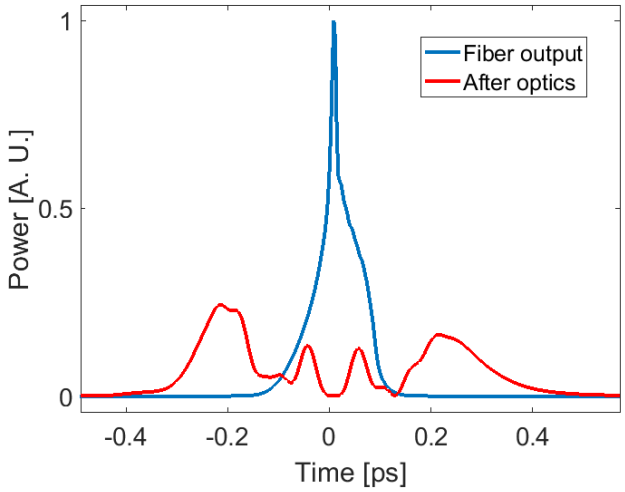

Figure 22 –Predicted temporal shape of the pulse with chirping material equivalent of 35 mm of BK7 placed on path of the pulse and at the fibre output. SC generated at the average power of 200 mW out of 17 mm fibre.

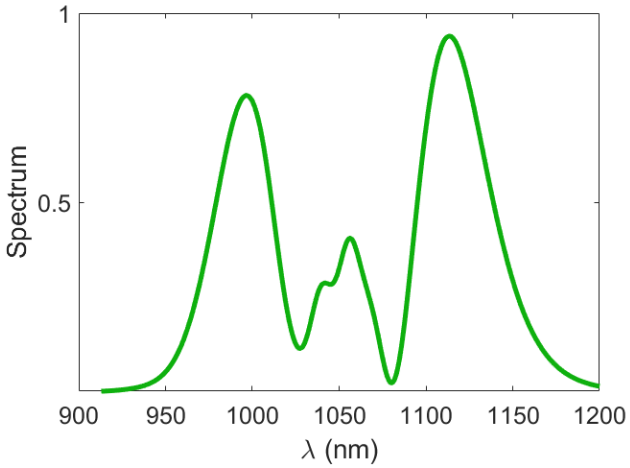

Figure 23 - Predicted spectrum out of 17 mm CGCRI fibre at 200 mW launched power

3.3.3 ZDW (CGCRI) fibre with input at 800 nm

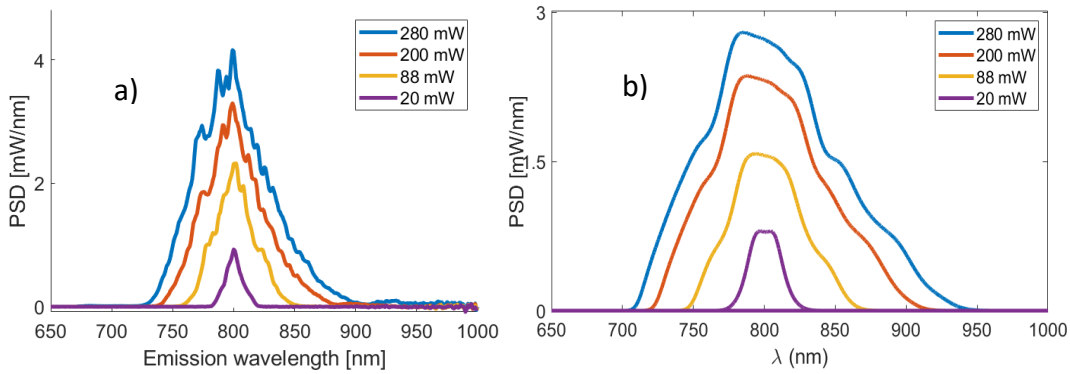

Figure 24 - measured (a) and simulated (b) output of 340 mm CGCRI fibre at 800 nm

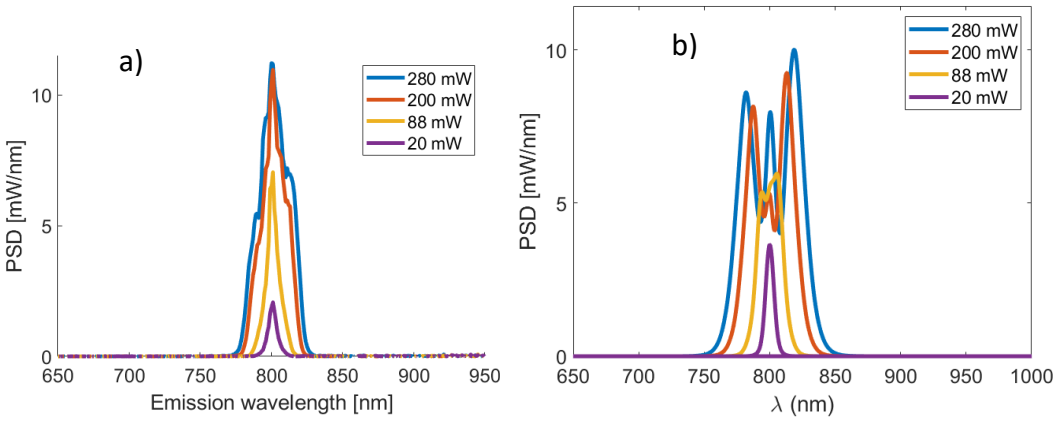

Figure 25 - measured (a) and simulated (b) output of 13 mm CGCRI fibre at 800 nm

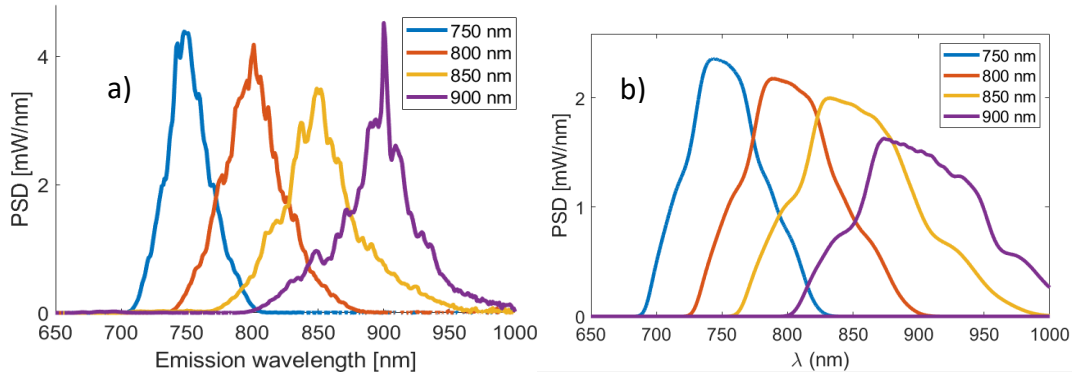

Figure 26 - measured (a) and simulated (b) output of CGCRI 340 mm fibre for 170 mW power for different wavelengths

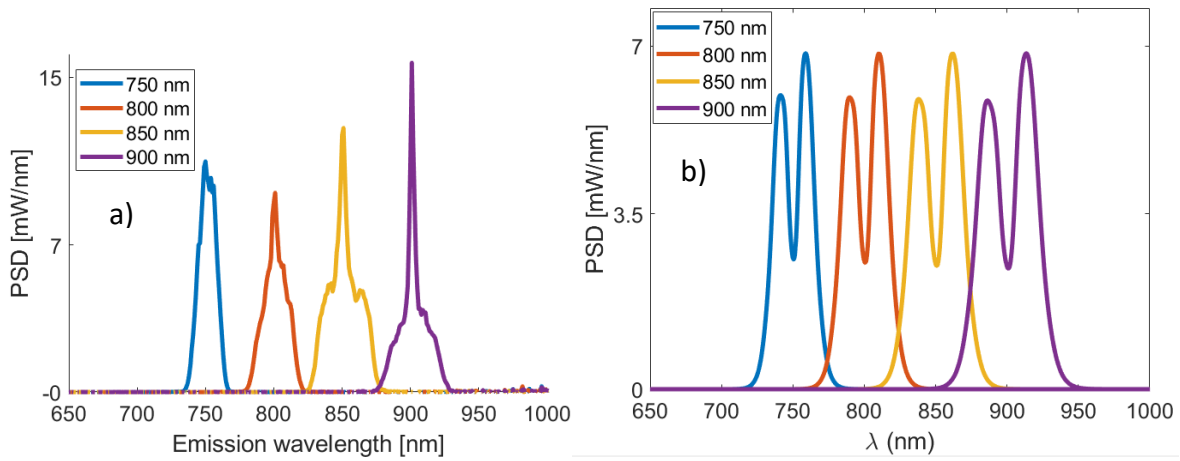

Figure 27 - measured (a) and simulated (b) output of CGCRI 13 mm fibre for 170 mW power for different wavelengths

Because the dispersion is significantly lower for CGCRI fibre for 800 nm than for the later described NEG-1 fibre, the broadening is significantly reduced in comparison to the ANDi fibre, either for 340 (Figure 24 and Figure 26) or for 17 mm lengths (Figure 25 and Figure 27).

The clearly seen fraction of light registered at 650-700 nm and 900-1000 nm can be most probably explained by the not fully eliminated guidance of the fraction of the total coupled power within the cladding. This fraction of power, however insignificant, can produce extensive broadening (as explained in 2.9.5).

The fibre output spectrum is more sensitive to changes of power than the ANDi fibre.

Because of the larger core size in this fibre, any kind of asymmetry in the core is not as influential on the birefringence, and, by extension – on the depolarisation of the output spectrum. Because of that, the fibre exhibits lower depolarisation than its All Normal Dispersion counterpart, which makes it a perfect candidate for imaging in the fingerprint region. Depolarisation stays low independently on the fibre length – see Figure 28. The depolarisation measurement has been conducted through registering of the spectra after the fibre, with a polariser added to separate the components.

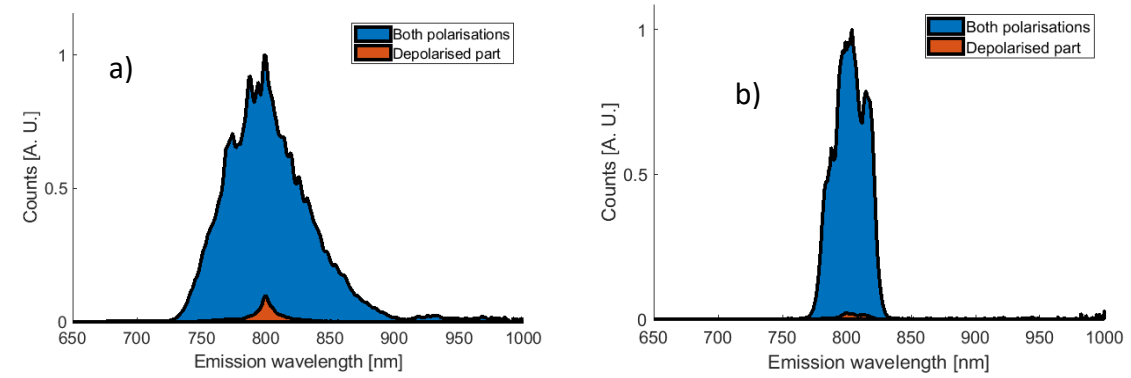

Figure 28 - depolarisation for two pieces of CGCRI fibre - 340 mm (a) and 17 mm (b) pumped at 800 nm with 280 mW

3.3.4 FemtoWHITE CARS fibre with input at 800 nm

FemtoWHITE CARS as a commercially available product has been considered the best available tool for long time, and because of that it has been used in many projects [132]. It is therefore a natural move to characterise it in the same way as was done with the two investigated fibres, in order to provide necessary context to the research.

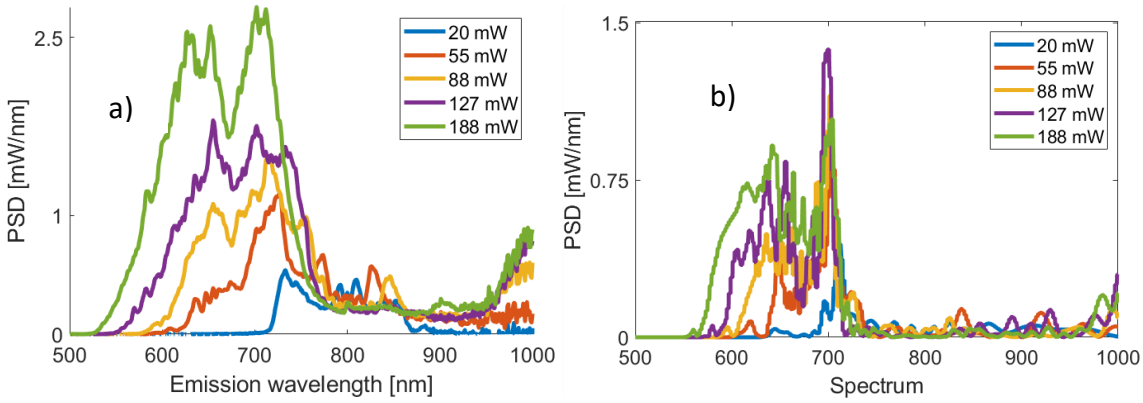

Figure 29 - femtoWHITE CARS characterization - experimental (a) and through simulation (b)

Through processing of the specifications provided by the fibre manufacturer, we have achieved capability of simulating the output of this fibre as well. As the simulation has been conducted using approximate fibre parameters retrieved from the specification sheet, minor differences in the specific shape of the output spectrum in comparison to measurements can

be seen in Figure 29. Also, the inherent low stability of the spectral output in response to minor fluctuations of input power exacerbates these differences.

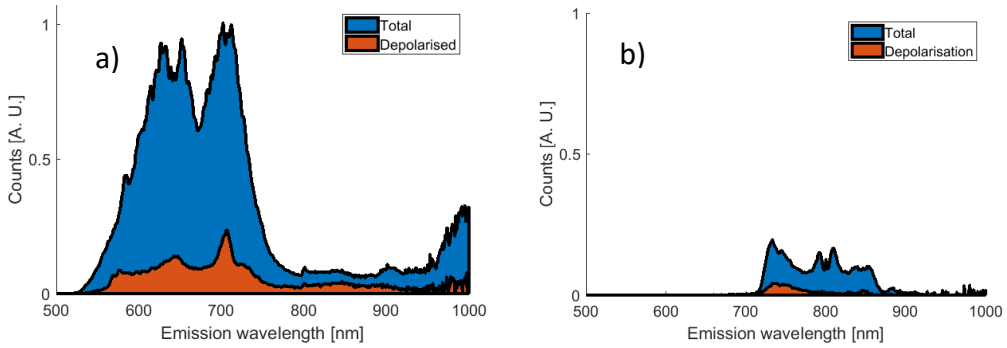

Figure 30 - Depolarisation in femtoWHITE CARS for outputs of 188 mW (a) and 20 mW (b)

As one can see from Figure 30 the depolarisation at the fibre output is power-dependent – the higher the power, the more prominent the cross-polarised component is.

3.3.5 NKT ANDi fibre pumped at 1055 nm

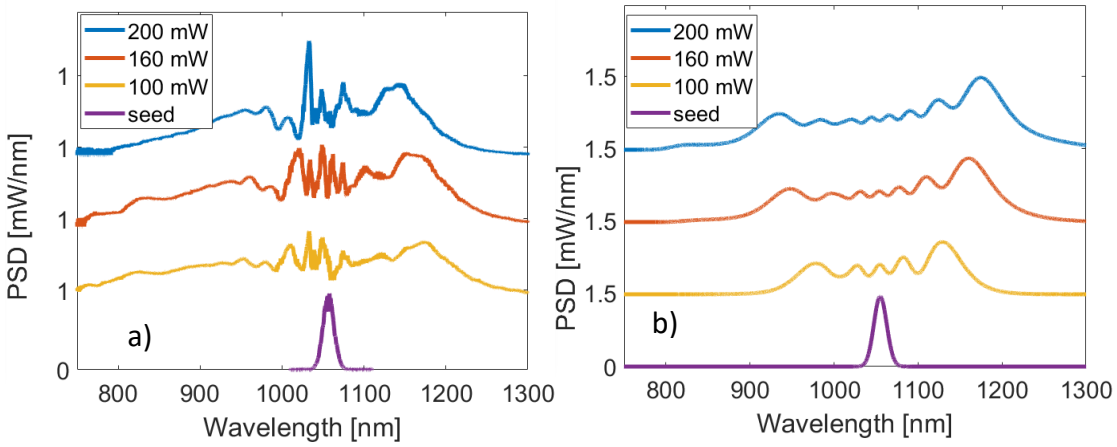

Figure 31 - Spectral intensity of generated SC (a) vs. simulated broadening for varied powers (b) in the NKT ANDI NEG-1 fibre of 37 mm. Powers in legend are given in mW.

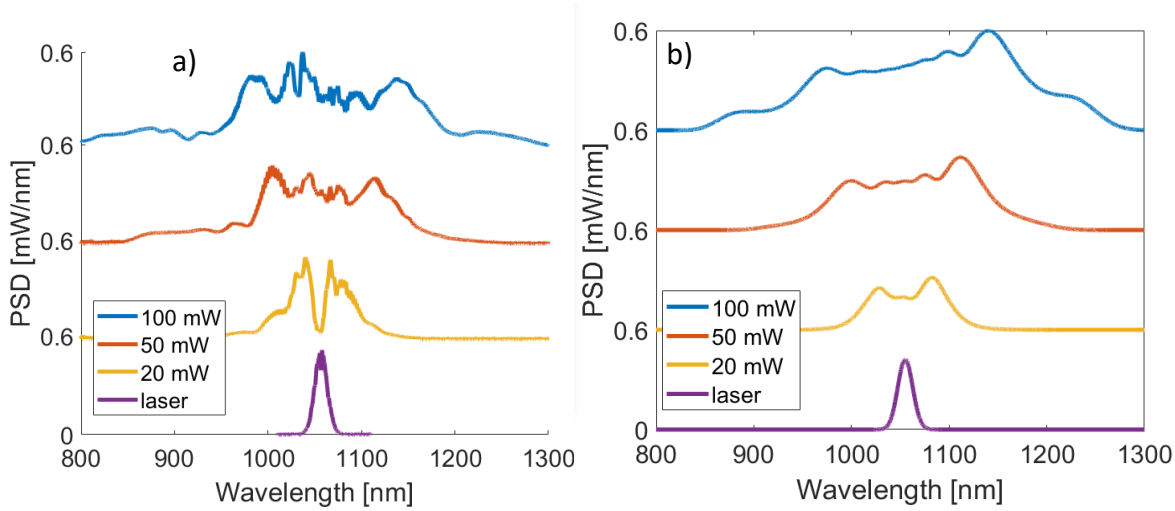

Figure 32 - Spectral intensity of generated SC (a) vs. simulated broadening for varied powers (b) in the NKT ANDI NEG-1 fibre of 85 mm. Powers are given in mW.

For similarily formatted figures later in the text this convention holds – a) experiment and b) simulation

Spectral characterisation of the fibre has been done for lengths of 127, 85 and 37 mm. The spectral characterisation of 37 mm fibre was promising, delivering power concentrated in 200 nm range, at the same time being consistent with the simulations (see Figure 31 and Figure 32). Spectra for 127 mm of fibre were too broad and are not shown.

3.3.6 NKT ANDi fibre pumped at 800 nm laser

As described in **2.9.6 Influence on the spectral output**, for ANDi fibres the spectral output broadens until wavebreaking occurs. After the wavebreaking occurs, the spectrum is not significantly dependent on power or length, even if it is still subjected to some spectral instability as it is dependent on the variations caused by changes in coupled power, caused by inherent noise of a fibre-based system. The closer one comes with the pump wavelength to Minimum Dispersion Wavelength, the more prominent the broadening is, as already discussed.

3.3.6a Power dependence of the output for each fibre length

The power dependence of the output spectrum can be seen on Figure 33. The divergence between the simulation and the experimental results (like the lobe arising on a)

can be possibly explained by the depolarisation of the spectrum through the birefringence of the fibre (**see** Figure 38**).**

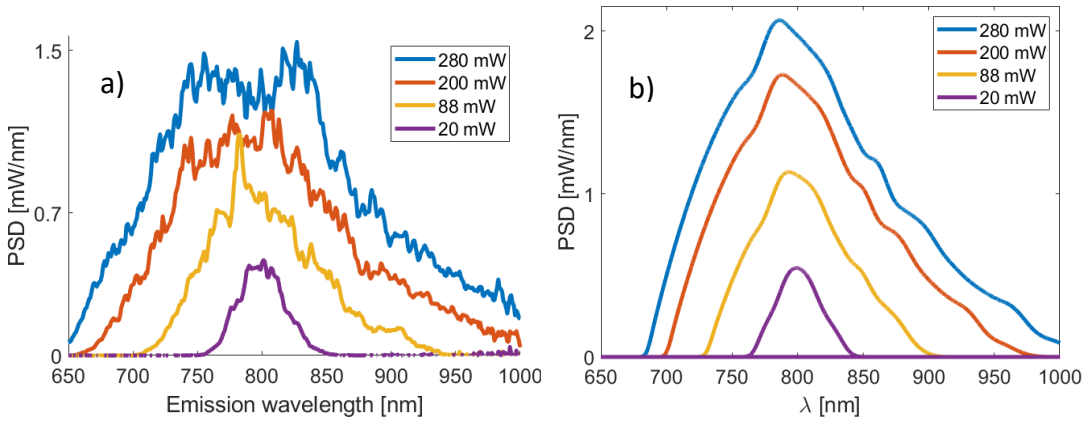

Figure 33 - 430 mm NEG-1 fibre at 800 nm pump

The most extensive broadening for NEG-1 fibre occurs for long propagation lengths. However, that is limited through the wavebreaking length, after which the spectral broadening slows down, and temporal broadening starts to be dominant. Taking into account also the detrimental effect of long propagation length on the depolarisation, it does seem that the wavebreaking length is the optimal fibre size for the purpose of that project.

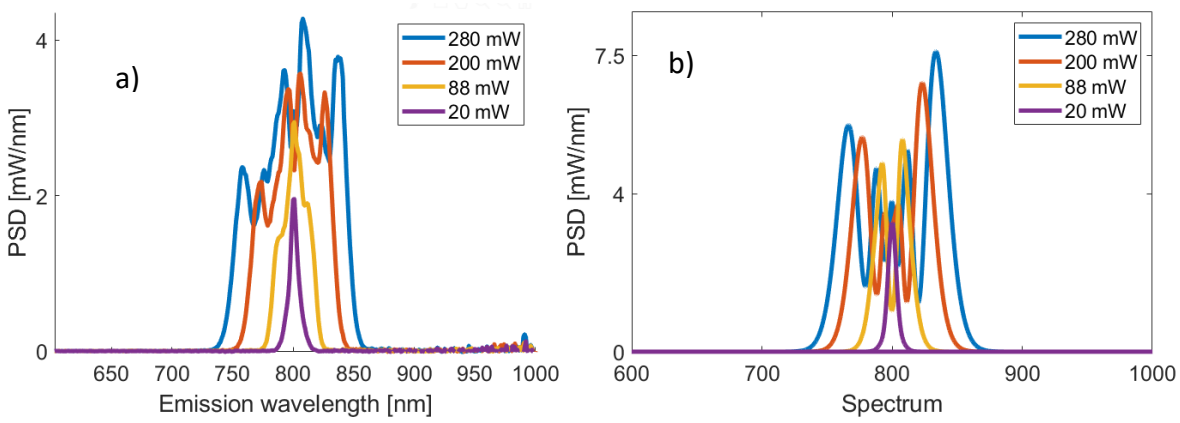

Figure 34- 13 mm NEG-1 fibre at 800 nm pump

The divergence between results and simulations on Figure 34, exceptionally visible around the pump wavelength of 800 nm, can possibly ascribed to either depolarisation, or unstripped power coupled into the cladding.

3.3.6b Pump wavelength variation at constant power of 170 mW

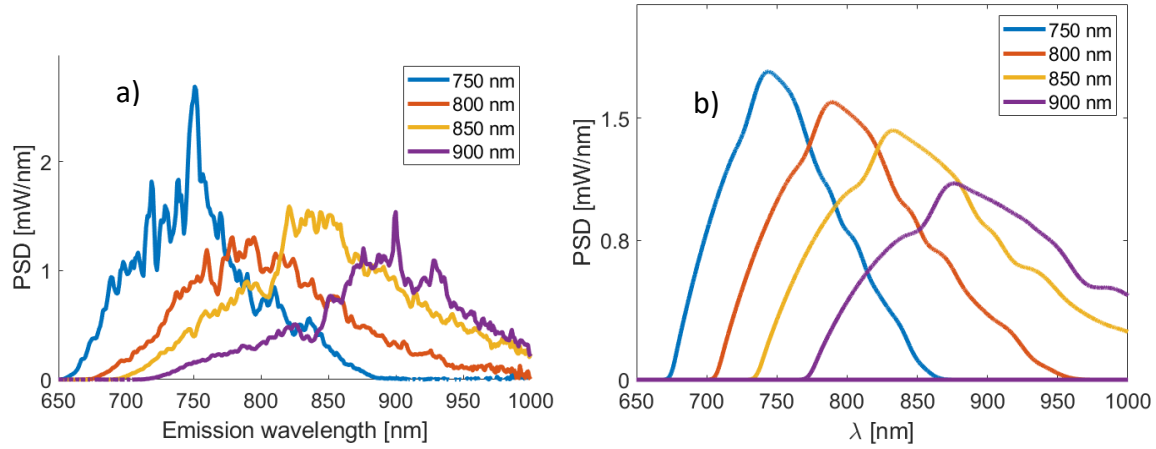

Figure 35 - output spectra out of 430 mm ANDi fibre for different pump wavelengths at constant power of 170 mW a) experimental and b) simulated

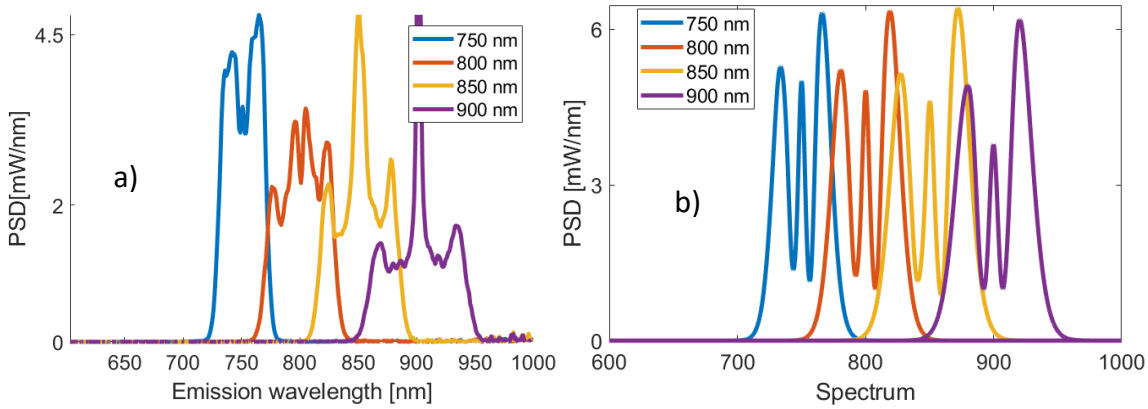

Figure 36 - output spectra out of 13 mm ANDi fibre for different pump wavelengths at constant power of 170 mW a) experimental and b) simulated

The fibre output has also been registered and simulated for different wavelengths for constant power (Figure 35, Figure 36). What is evident, is that the closer we get to the Minimum Dispersion Wavelength, the greater the broadening, what is consistent with conditions set in **2.8 Hyperspectral CARS & multimodal nonlinear imaging approaches**.

3.3.6c Depolarisation dependence on fibre length

The spectral shape acquired is diverging from the simulations. That is most probably caused by the processes of interaction between two polarisation modes, caused by the birefringence of the fibre. It has been previously reported, that there can arise spectral bands attributable to Modulation Instability in weakly birefringent microstructured fibres [133], which can contribute to the differences between spectra for two orthogonal polarisation directions.

As seen on the Figure 38, for longer fibre the depolarisation is higher than for the shorter pieces for the same power. Moreover, the attempt has been made to reduce the polarisation by placing it between two squeeze plates, as previously attempted by [134]. This gave limited success, and further attempts have been made with a chopper, attenuating the average power without the reduction of peak powers of pulses. This also gave limited success as visible on Figure 37. The chopper did not reduce the depolarisation considerably, suggesting the depolarisation at the output of the fibre is more related to the peak power than to average power and associated thermal effects. An alternative would be to procure the polarization maintaining version of this fibre, but that was not available to us here- NKT stopped selling that version of this fibre. Deeper insight into the challenge of designing such fibres was presented in [135].

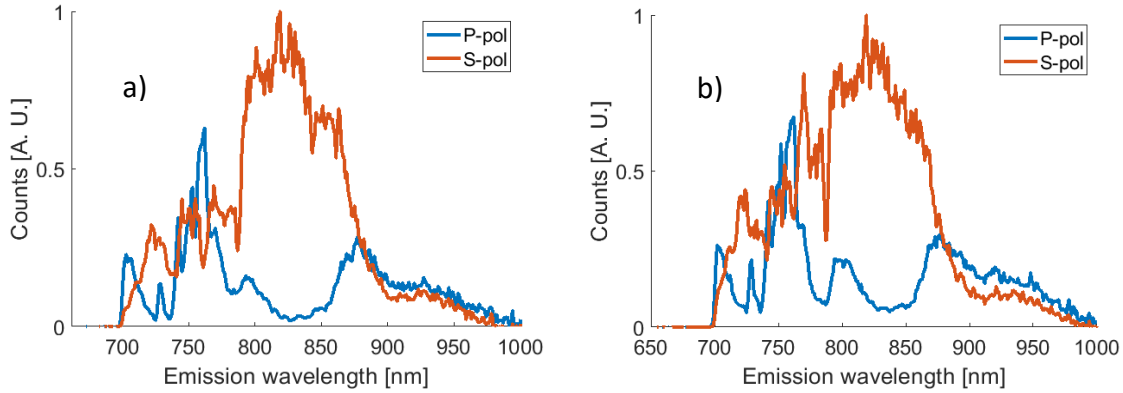

Figure 37 - Depolarisation for recombined beam (237 mW at the fibre output) without any attenuation (a) and with chopper attenuating the power to 50 mW (b)

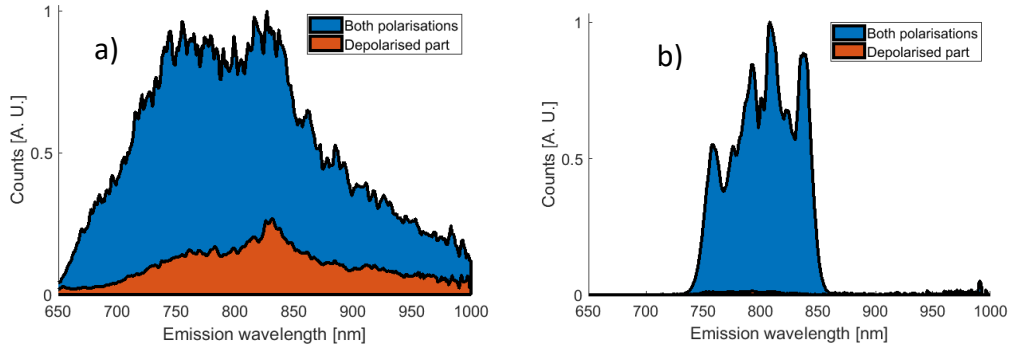

Figure 38 - Depolarisation for two different fibre lengths of NEG-1 for power 280 mW power coupled for 430 mm (a) and 15 mm (b) long fibres

3.4 Application of NKT ANDi fibre source pumped at 800 nm for bioimaging

One of the fibres- the ANDi NEG-1 fibre – has been selected for further examination directly in context of the intended application – SF- CARS. Once the spectral shape was known, it was natural to follow with attempt to predict, what would be the potential range of Raman vibrations that this spectrum would excite.

To estimate our SF-CARS excitation efficiency over the targeted wavenumber range, the power-spectral-density directly from the fibre output (P(λ)) (see Figure 39(a)) was spectrally

filtered within the simulation to account for the transmittance (T_D) and the reflectance (R_D) of the dichroic beam splitters used in the delay line in our setup. This way it was possible to predict expected experimental pump and Stokes powers after division and recombination. The anti-Stokes signal obtained upon targeting each of the instantaneous frequency difference was then integrated across the whole duration of pump-Stokes overlap (not unlike the Figure **13**). This last step required consideration of the temporal overlap of the pulses, so we used the output of the simulation and calculated the predicted GDD added by the glass blocks and other optical elements in the beam. We used Eq. (43, 44, 45) below, in which λ_1 and λ_2 are the wavelengths of the pump and Stokes beams needed for targeting a Raman resonance at frequency offset of Ω_1, B_A is the beam area of the focused laser at the sample, I_p and I_s are the intensities of the pump and Stokes beams respectively. The non-resonant CARS signal is calculated for each of the components of the overlapped parts according to (45) taking into account the intensities only, and assuming a proportionality constant R=1, as no resonances are present in this simulation.

$$I_S(\lambda) = \frac{P(\lambda_1)T_D^2}{B_A} \quad (43) \qquad I_p(\lambda) = \frac{P(\lambda_2)R_D^2}{B_A} \quad (44) \qquad I_{CARS}(\Omega_1) \sim R I_p^2(\lambda_1) I_S(\lambda_2) \quad (45)$$

The anti-Stokes output power was then filtered to account for the effects of the dichroic beam-splitters separating the output to provide the estimated detected four wave mixing signal for each Raman resonance targeted. The results vs fibre length are shown in Figure 39(b). The power targeting CH-region wavenumbers is lower for a 4 cm compared to a 9 cm length of fibre. However, increasing to 12 cm causes only minor additional power, so a length of 9 cm was selected for further study. We next considered the linearity of the slope of the frequency vs. time mapping at the fibre output as any distortion makes it more difficult to match pump and Stokes beams. The key factor is the so-called 'wave-breaking length', which determines the end of the first (and most rapid) stage of the spectral broadening, beyond which dispersion becomes dominant, leading to a subsequent predominance of temporal broadening [45]. Linearly chirped pulses are produced with 1x to 2x the wave-breaking length and as at the 280 mW power level, the wave-breaking length was ~5 cm, the 9 cm length is

appropriate. (From a purely technical perspective, we found this length was convenient with standard fibre holders e.g. HFV002 from Thorlabs)

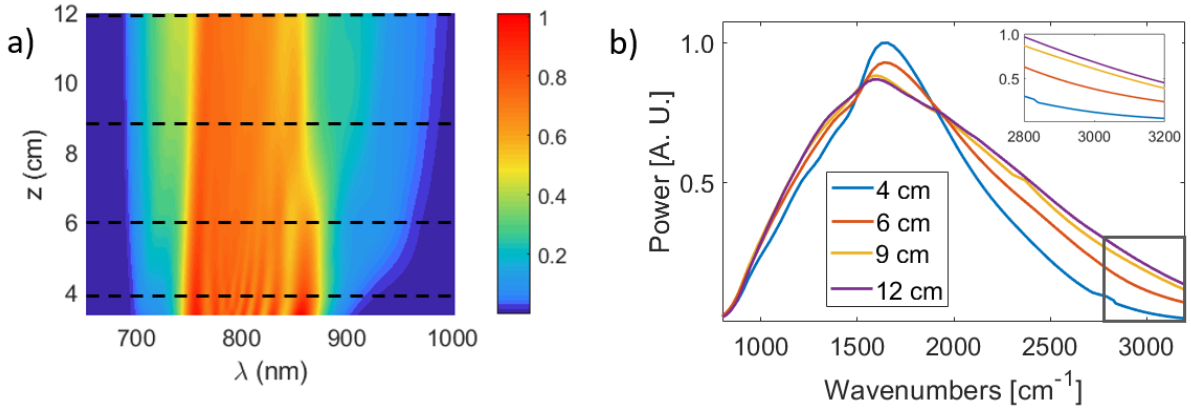

Figure 39 - Simulation results: (a) Spectrum from ANDi fibre vs. length; (b) CARS excitation power at microscope focus for various fibre lengths. All data is for 280 mW of power at the fibre output. (Total pulse energy 3.5 nJ.)

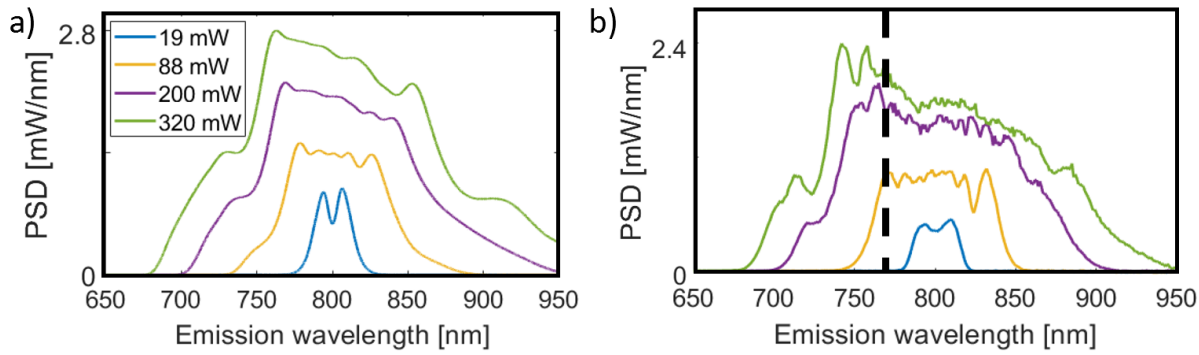

Figure 40 - Output spectra from 9 cm ANDi fibre vs. output power. a) Simulation results; and b) Experimental data. The dashed line in b) indicates the separation between pump and Stokes for SF-CARS.

We next plotted the predicted power dependence of both the simulated spectra and experimental spectra (Figure 40). The spectra steadily broaden with power and there is good agreement between the simulations and measurements. The slight differences we observe may be attributed to the use of a scalar GNLSE rather than a vector-coupled model.

3.5 Summary

The CGCRI fibre has proved to be very efficient source while pumped at 1055 nm, however the proximity to the zero dispersion wavelength causes the spectrum to be coherent only for fibre lengths lower than the soliton fission threshold. Once soliton fission has occurred, the spectrum starts to broaden across both sides of the Zero Dispersion Wavelength. This substantiates additional concerns, that even if that spectrum has been coherent throughout, parts of it would significantly overlap with the excited signal from the sample, making filter-based detection impossible. That proves to be challenging. The ANDi fibre broadening is lower at any input power level, but by increasing the fibre length we can increase that. Because of the dispersion curve fully in the normal dispersion regime, the soliton fission effects do not influence the output spectrum.

The CGCRI fibre has proved to be efficient source while pumped at 800 nm as well, however the broadening was not enough to target CH region- only fingerprint. Because the whole broadening occurs in the Normal Dispersion region, one avoids unwanted soliton fission effects. The ANDi fibre on the other hand, because of lower core diameter and higher dispersion, gives bigger spectral broadening, which enables the imaging of both CH region and fingerprint region. Therefore, in spite of exhibiting higher degree of de-polarisation than any of the other investigated fibres, it still is advantageous to apply it for imaging, and we consider it is better than both commercial femtoWHITE CARS source and the CGCRI fibre.

Next, a systematic comparison sweeping (i) input pump power, (ii) pump wavelength and (iii) fibre length comparing the coherent SC from a femtoWHITE-CARS (2 ZDWs) fibre, a fibre with one ZDW offset above the seed wavelength, and an all-normal dispersion (ANDi) fibre was performed. Starting with the seed laser polarisation aligned to a principal fibre axis, the total experimentally measured spectral output and importantly the polarisation resolved spectral component on the orthogonal axis were shown, which is a measure of the power-dependent depolarisation [134]. That depolarisation can be decreased, to a degree, through squeezing the fibre with metal plates, which induces the stress-related birefringence, decreasing presence of orthogonal modes in output spectrum of previously non-PM fibres, such as ANDi

fibres, previously demonstrated by [134]. This orthogonal component will degrade the efficiency of the CARS signal but still contributes to the bio-toxicity that limits the maximum power for imaging.

The results show that the CGCRI fibre has the lowest level of depolarisation, probably because of the large core and relatively low nonlinearity. The ANDi fibre produced a spectrum that is ideal for CARS in the Raman fingerprint region as it has high PSD in both the pump and Stokes branches enabling the full spectrum to be used. While the rather severe depolarisation (30% measured worst case) somewhat reduces this attraction, a polarisation maintaining version of such a fibre would represent an excellent choice for fingerprint imaging. The femtoWHITE-CARS fibre has lower depolarisation than the ANDi fibre in the region near the pump where the other fibres show the most severe depolarisation. (Results are not available in the long wavelength band due to unexpected fibre damage.) Its performance in the lipid-region is as good as, or even slightly improved compared to the ANDi fibre. However, this fibre is widely known to produce >1000 nm spectra, and the depleted region between the ZDWs limits the PSD available in the fingerprint region compared to the ANDi fibre, which again points out the tailored NEG-1 as an optimum source for imaging in that region

4 APPLICATION OF TAILORED-CONTINUUM FROM ANDI-FIBRE FOR LABEL-FREE BIOIMAGING WITH SF-CARS

4.1 Introduction

This chapter presents the results from application of the source in the labelled and label-free imaging modalities- labelled TPEF, auto-TP-fluorescence, SHG and finally, and most importantly, SF-CARS. The significance of the results is discussed and compared with currently available sources.

Disclaimer: part of the content of this chapter has been published in Applied Physics B (''Multimodal spectral focusing CARS and SFG microscopy with a tailored coherent continuum from a microstructured fibre'' [136]*)*

Users of femtoWHITE CARS modules have, to-date, used a pick-off of the fs seed laser as the pump and combined that with just the long wavelength part of the supercontinuum as the Stokes, thus losing the energy in the short-wavelength part of the supercontinuum and reducing signal power [63] [137] [138]. We wanted to use that short-wavelength power so, motivated partly by the recently reported technique using intra-pulse frequency combinations for broadband-spectrum-based 'hyperspectral' 3-color CARS [46], we have used the full spectrum from the NL-1050-NEG-1 from NKT Photonics, to produce a coherent continuum [139] and demonstrated its use for SF-CARS and SHG/SFG imaging. We have avoided what some people see as a drawback of 3-color CARS, which is that it requires a synchronous narrowband (few ps equivalent bandwidth) probe, which generally necessitates a complex laser system.

4.2 Technical application issues

4.2.1 Spectral spread and its influence on the range of targeted wavenumbers

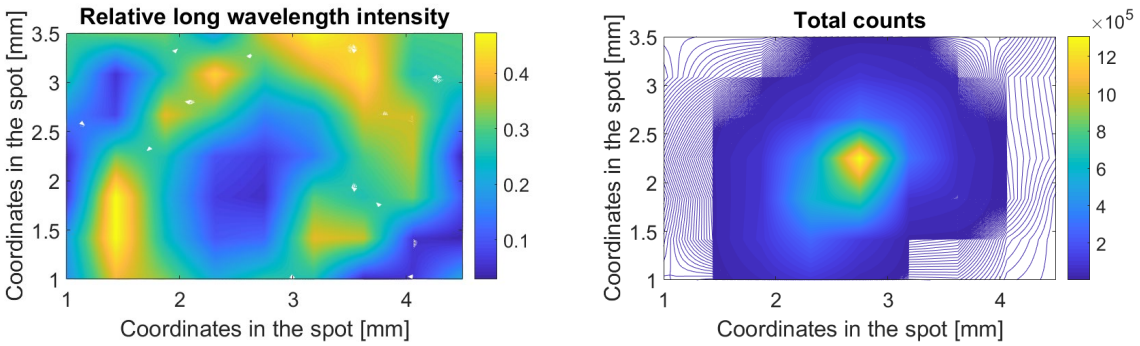

Figure 41 - Spectral chirp 338 cm after collimation of SC beam – relative intensity of long (831-922 nm) wavelengths range (left) as compared to total intensity of the signal (right)

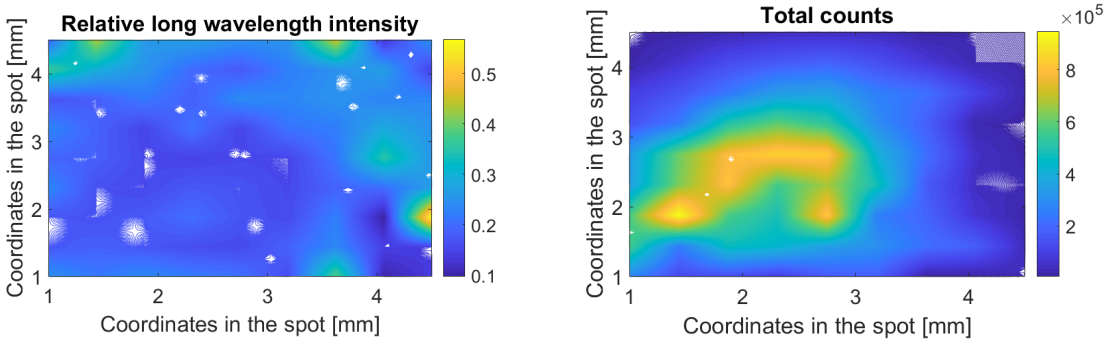

Figure 42 **- Spectral chirp 35 cm after collimation – relative intensity of long (831-922 nm) wavelength range (left) as compared to total intensity of the signal (right)**

The different focusing properties of a plano-convex singlet cause different refraction for different wavelengths. That difference becomes prominent at the large distances, and can cause problems with appropriate coupling the broadband spectrum into the microscope (see Figure 41 and Figure **42**). The maximum of power of Stokes is concentrated in the short wavelengths 770-850 nm, but components between 850 and 1000 nm are responsible for targeting the 3000 cm^{-1} range. Therefore, if they are being clipped, the accessible wavenumber range is becoming narrower. The use of achromatic doublet caused the reduction of the problem and improved the range of transmission throughout the

microscope. After that was implemented, beam was no longer clipped on the back aperture of the objective, which has been the case previously, as seen on Figure **43**.

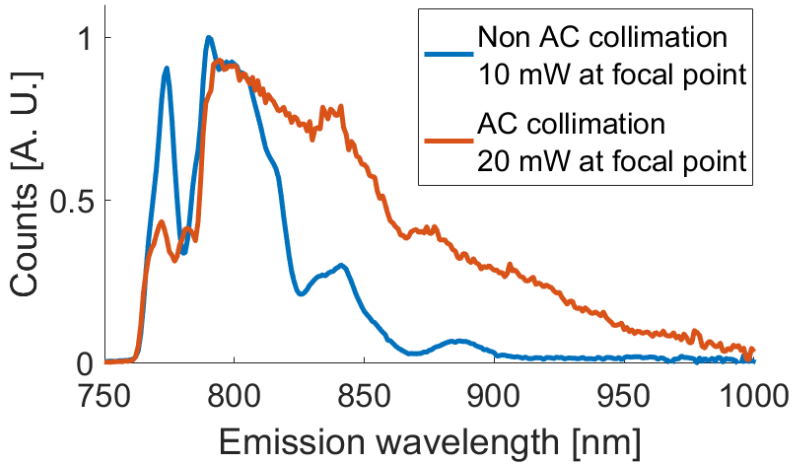

Figure 43 **– Comparison of the spectrum registered at the focal point of the microscope before applying achromatic (AC) lens for collimation of the fibre output, and after, for the same power at the fibre output. Significant improvement in transmission of longer wavelengths has been registered, as seen through spectral and power comparison.**

4.2.2 M^2 measurements

M^2 has been measured for both pump and Stokes, and it was found to be between 1 and 1.1 for both of them, not deviating significantly from the MaiTai laser M^2, which was measured to be 1.

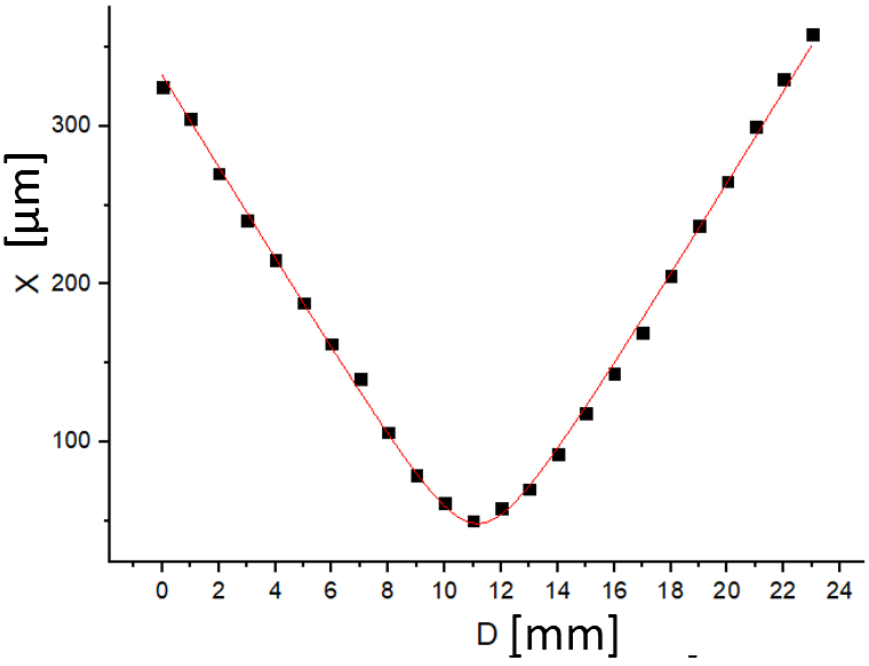

Figure 44 - **M2 investigation of Stokes beam in one of the axis, representative for all 4 measurements**

4.3 Experimental setup for SF-CARS

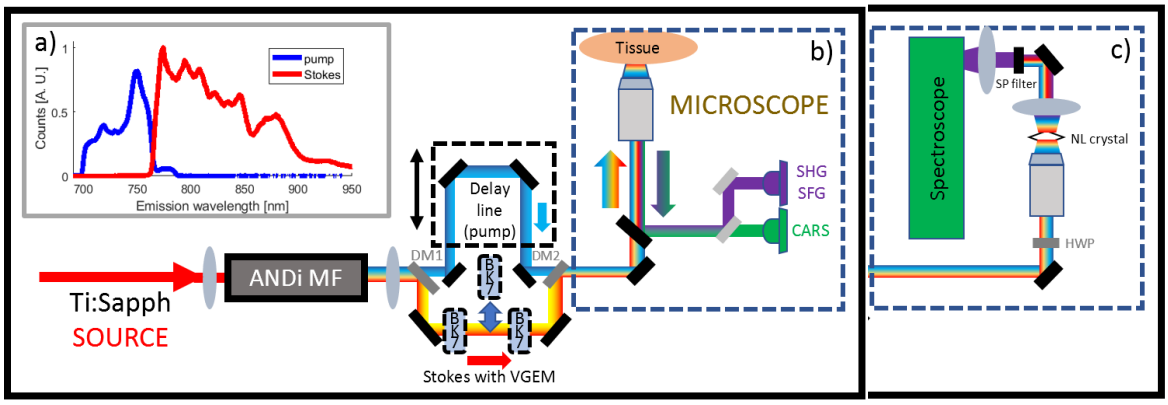

Figure 45 - Schematic of the spectral focusing CARS imaging setup. Inset a) showing the spectrum incident on the sample, subfigure b) showing the detection setup for imaging and spectroscopy, subfigure c) showing the detection setup for SHG/SFG characterisation.

Schematic of the setup used is shown on Figure 45. The ANDi-microstructured fibre (ANDi MF) is used for the generation of a broadband spectrum. A dichroic mirror, DM1, separates the supercontinuum into pump and Stokes beams (spectra shown inset). The delay line ensures temporal overlap at the sample. The modular Variable GDD Equalizing Module (VGEM) balances the GDD of the Stokes relative to the pump. Then, the collinear beams are coupled into the microscope for imaging.

One of the important issues in the design of the setup, is the reflectivity of the silver-coated mirrors. With over 20 mirrors in the setup one has to consider the lossy reflections. Even with reflectivity in the range of 94-96 % per mirror, the lossess accumulate, resulting in low (58-65%) transmission through the optical path. Alternatives have been considered- e.g. gold mirrors and dichroic mirrors. However, gold mirrors did not provide better reflectivity throughout region of interest (95% per mirror, 48% of initial power at the end of the path), and the the ultrafast dichroic mirrors did not present a broad spectral reflectivity. Broadband dichroic mirrors, on the other hand, did not conserve temporal characteristics of the pulse correctly, making them largely unsuitable for broadband applications- see e.g. measurements (courtesy of Thorlabs) of dispersion characteristics of BB1-EO3 product (Figure 46). It is clear, that after multiple reflection from this mirror the phase profile would be heavily distorted.

That could be solved through either custom fabrication of these devices or and SLM compensation, both costly and deemed not within the scope of the project, which led to use of the silver-coated mirrors, in spite of their unfavourable loss characteristics.

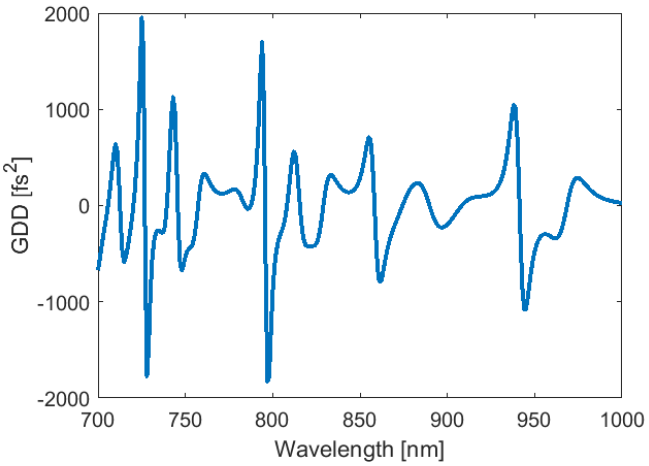

Figure 46 - Dispersion characteristics of BB1-EO3

The output beam was collimated using an achromatic lens (Thorlabs AC064-013-B-ML f=13 mm) and then divided into pump and Stokes components using a dichroic filter with a cut-off at 775 nm (Semrock FF775-DI01-25X36). The pump pulse was directed into a delay line (STANDA 8MT175-200), which provides displacement with a resolution of up to 310 nm which corresponds to a temporal displacement of 2 fs in the retro-reflection setup used here. The stage is equipped with an encoder providing feedback on its position and ensuring reproducibility of the temporal offset. The VGEM device was constructed simply by assembling anti-reflection coated polished glass blocks in a line. Up to 5 x 12 mm thick glass blocks (Thorlabs WG12012-B) blocks and 1 block of 5 mm thick glass (Thorlabs WG11050) were used in either a single- or double-pass arrangement to provide a total insertion length of up to 130 mm. Flip-mounts ensured that the path length through the VGEM was easy to adjust. The pump and Stokes beams were recombined using an identical Semrock FF775-DI01-25X36 dichroic and were aligned collinearly and coupled into an upright microscope (Leica DM305) through a pair of scanning galvanometric mirrors (Cambridge Technology 6220H). All

optical components had an appropriate AR coating to reduce losses for the near infrared beams.

A 63x water immersion objective with NA=1.2 from Leica was used for the imaging and spectroscopy experiments. The objective lens is corrected for aberration in the visible and NIR (up to 1100 nm) which is important for multimodal imaging with different excitation wavelengths. The average power at the focal point was measured to be 16 mW for the pump (spectral width 70 nm), and 23 mW for the Stokes (spectral width 130 nm), which in total corresponds to an average PSD of >180 µW/nm. Images were acquired in the back-scattered geometry using non-descanned detection, since for multiphoton techniques there is no requirement to use a confocal pin-hole to reduce out-of-focus signal. Hamamatsu PMT detectors (H10722-01, H10722-20) were used for the simultaneous detection of CARS/TPEF and SHG/SFG signals respectively.

There was an inherent conflict while choosing the correct filter sets- because, the narrower the excitation spectrum, the better the extinction of that spectrum is at the detection- i.e. the signal, orders of magnitude weaker than the excitation SC, needs not to be overshadowed by the latter. However, the broader the spectrum, the bigger wavenumber range it covers. Therefore, there is a difficult balance needed here- and the choice of filters heavily depends on the application of the spectrum. If wavenumbers lower than 1000 cm^{-1} are of the interest to investigator, instead of filtering short wavelength part of the spectrum at 700 nm, one can filter e.g. at 750 nm. That removes the part of SC that would overlap with the anti-Stokes emission associated with wavenumbers <1000 cm^{-1}, at the cost of losing the capability of targeting CH region. Additionally, extremely sharp filter is needed at the detection, so as to remove the leftover excitation SC, at the same time letting through maximum of the emitted anti-Stokes emission.

For the purpose of >1000 cm^{-1} imaging, the signals were separated from the supercontinuum using a 694 nm short pass dichroic (Semrock FF02-694/SP-25) and further a 550 nm long pass filter (Thorlabs 550LP) and 400 nm bandpass filter (FB400-40) for the CARS and SHG/SFG imaging channels, respectively. ScanImage software (Vidrio Technologies) was used to

acquire the images pixel-by-pixel [140]. All bio-images were acquired in a 1024 pixel x 1024 pixel format, with a dwell time of 32 µs per pixel and averaging over 6 consecutively acquired frames. The pure fluorescent background has been subtracted from pictures acquired in CARS modality.

4.4 Imaging experiments

Firstly, GDD equalization over the vibrational frequency range of 1000-3050 cm^{-1} is experimentally demonstrated with the opto-mechanical, modular, Variable GDD Equalizing Module (VGEM) which enabled the amount of glass in the path of the Stokes beam to be changed in a quasi-continuous, modular way. Images of mouse adipose tissue were recorded, in a dual-channel setup, where the signal is separated into SHG/SFG and CARS/TPEF detectors, enabling concurrent multimodal imaging. Note that SFG did not require pulse compression, so no post-processing of the SFG and CARS images was needed with respect to image registration: This is a clear advantage compared to systems that record the images from various modalities only after a delay while changing the pulse parameters of the laser and which thus require algorithms to post-process the data.

4.4.1 SF-CARS calibration and chirp equalisation

For preliminary spectroscopy, solid dry samples of thymine (T0376, Sigma), deuterated palmitic acid (366897, Sigma) and 40 µm polystyrene (PS) beads (Fisher) were used for calibration. Each of these samples were prepared separately by placing a tiny amount (~0.1 mg) of each on a standard glass microscope slide under a coverslip (#1.5; 0.17 mm thick), the edges of which were sealed with a nitrocellulose-based varnish in order to allow imaging with a water immersion objective, as otherwise the water would leak inside and wash away the sample. Additionally, a sample containing a mixture of 40 µm polystyrene (PS) and polymethylmethacrylate (PMMA) beads was prepared in the same manner as above for the three single component samples.

The spontaneous Raman spectra for thymine and deuterated palmitic acid, necessary for creating a calibrated reference to be subsequently compared with the CARS spectra, were

acquired using a 633 nm laser, a 20x (0.8 NA) objective using a Renishaw 2000 micro-spectroscopy system set for 20 s acquisition times and averaged over 3 spectra. The spectrum for polystyrene was taken with a home-built Raman micro-spectrometer system utilizing a Shamrock303 spectrograph with an Andor iDus420 camera as the detector and equipped with a 785 nm laser. The spectrum was acquired with a single 20 second exposure with 0.6 mW laser power using a 40x (0.9 NA) objective.

The temporal delay (IFD) vs. Raman frequency shift was then calibrated to allow spectroscopic Raman characterization of samples by measuring just the position of the delay stage from its encoder at which the hyper-spectral SF-CARS peaks align with the independently measured spontaneous Raman peaks. Spontaneous Raman spectra and the registered (i.e. calibrated) SF-CARS spectra for thymine and polystyrene are shown below in Figure 47 a), b). Small differences in actual CARS peak positions are to be expected due to the dispersive line-shapes and mixing with the non-resonant background in CARS. While further data processing, e.g. using a Kramers-Kronig transform [141] could separate those effects, here we use the best fit to the two main peak positions from the raw data as an approximation to demonstrate hyperspectral SF-CARS imaging.

For these non-biological samples, SF-CARS spectra were recorded by acquiring images of the sample slides of each material separately using different relative delays between the pump and the Stokes beams and then plotting the image intensity for the specific region of interest with respect to the delay. These spectra were used only for calibration. Next, we used the sample which had the admixture of the different polymer beads to demonstrate chemically-selective contrast via hyper-spectral SF-CARS. Images (in sections 3.4 and 4 below) were acquired with 128 pixel x 128 pixel resolution with 60 µs pixel dwell time following averaging over 3 recorded frames.

The SF-CARS resolution was well matched to the widths of the peaks in the spontaneous data and we achieved 30 cm^{-1} (full-width half maximum) and 37 cm^{-1} for the 1372 cm^{-1} and 1678 cm^{-1} thymine peaks and 40 cm^{-1} for the 3054 cm^{-1} polystyrene peak. The resolutions achieved here agree well with the 36 cm^{-1} resolution predicted using the approximate analytic equation

Ref. [56] calculated from the width of our measured pump/Stokes spectra and our calculated pulse durations. Hence the VGEM operated successfully across the entire Raman frequency range needed for bio-imaging. However, we note that the width of 1374 cm^{-1} peak is narrower than the 1678 cm^{-1} peak. The apparent improvement in resolution at lower wavenumbers is probably due to filtering-out of a part of the emitted anti-Stokes wavelengths by our detection setup.

Spectra of Thymine, Deuterated Palmitic Acid, Polystyrene and PMMA before and after chirp equalisation are presented, which illustrates how the latter influences the former. The shapes of the spectra can be roughly correlated to Raman spectral shapes. The resolution of the system is 30-40 cm^{-1}, which is comparable to the shift of Raman peaks caused by the convolution of resonant emission with the Non-Resonant Background. Therefore a liberty has been taken to compare the wavenumber values associated with the peaks visible on spontaneous Raman spectra of investigated substances with the positions of the intensity peaks on the registered spectra. Therefore, the correlation between the relative pump-Stokes delay and the targeted resonance can be established and used during bioimaging.

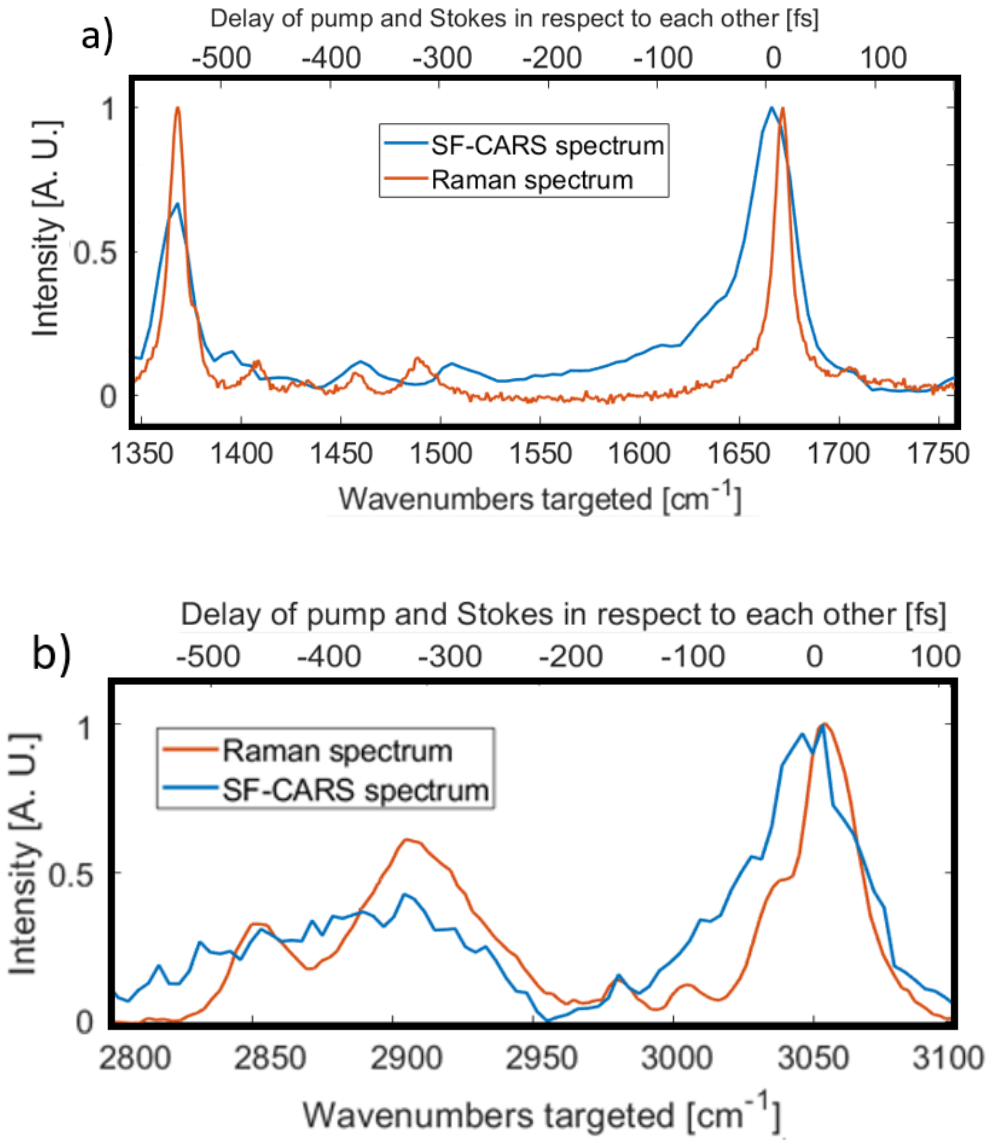

Figure 47 - Resolution and calibration in the fingerprint region (a, thymine crystals) and in the CH region (b, polystyrene beads)

Experimental data showing achievable resolution and the calibration of the relative pump vs. Stokes temporal delay (in fs) vs Raman resonance offset (in cm^{-1}) is shown on the Figure 47. Spontaneous Raman spectra (red) and SF-CARS spectra with optimised GDD equalization (blue). a) Thymine (finger-print region: VGEM pathlength 36 mm); and b) polystyrene (CH stretch region: VGEM pathlength 125 mm).

The maximum tuning speed with our delay stage was 32 cm^{-1}/ms, which enables switching between the extremes of the 900-3200 cm^{-1} range within 72 ms. Depending on pixel count,

this is likely to be much faster than the image acquisition time at any single frequency (up to 20 s), so is not normally a limitation. Even higher speeds are possible, e.g. more-complex, tailored, SF-CARS systems have achieved microsecond scanning, so the scan speed can be made comparable with the single-pixel dwell-time [142]

Calculations indicated that the FMHW durations of the chirped pump and Stokes before GDD equalization should be ~600 fs and 1.7 ps, respectively. The GDD in both the pump and Stokes beam path needs to be equalized after transmission through all of the microscope optics [57]. We first used simulations to estimate the GDD equalization required between the pump and Stokes for each targeted Raman resonance, and then refined these estimates experimentally using our VGEM. For the simulations, we estimated the total thickness of the lenses and transmission filters after the fibre to be equivalent to 14 cm of BK7. For glasses most often used in microscopy optics, the GDD decreases at longer wavelengths (e.g. the dispersion zero for fused silica is close to ~1300 nm). Therefore the additional glass blocks were placed in the longer-wavelength Stokes beam. GDD equalization for each Raman resonance, that is the target instantaneous frequency difference (IFD), was calculated based on dispersion, as per data for N-BK7 glass [143]. Thus for targeting an IFD of 2800-3050 cm^{-1} the amount of additional GDD equalization was 72-125 mm, reducing to 60 mm for 2100 cm^{-1} IFD and 36 mm for 1678 cm^{-1} IFD. The 6 blocks of glass in the VGEM could be used in single or double pass, giving 12 - 130 mm of additional BK7.

The dependence of the achievable spectral resolution on the VGEM glass path is plotted in Figure 49 a)-b) by integrating over the entire temporal overlap between pump and Stokes. Figure 49 a) shows that with a fixed length of BK7 in the Stokes path, the highest Raman resolutions are only achievable for a limited range of targeted IFDs. It is noted though that even when optimized, the spectral resolution is not uniform across the whole spectral range, predominantly due to residual higher order dispersion but also to a lesser extent due to the discrete increments in glass path (VGEM, in our case). Figure 49 b)(i-iii) show the profiles for the three cases: the fingerprint (900-1800 cm^{-1}), the so-called ‘silent’ (1800-2800 cm^{-1}) and the CH-stretching (2800-3200 cm^{-1}) regions confirming that the GDD compensation also maximises the anti-Stokes signal.

The same three chemicals as used for calibrating the delay stage position vs. CARS wavenumbers were used to check the predictions. As shown in Figure **49** c), the measured peaks become higher and narrower with the addition of the appropriate amount of glass, whereas both under- and over-compensation result in lower resolution, confirming the trends in the simulations.

Then, the theory can be used to calculate predicted correlation between peak height and width, on the basis of having a known amount of glass present on the path of the beam, and knowing the chirp of the pulse out of the fibre. The temporal duration of pump and Stokes can be therefore quantified through the chirp, and applied to the numerical simulation for predicting the interaction between the two. The algorithm is presented on Figure 48, where this loop has been conducted for the whole range of BK7 material put on the path of the beam.

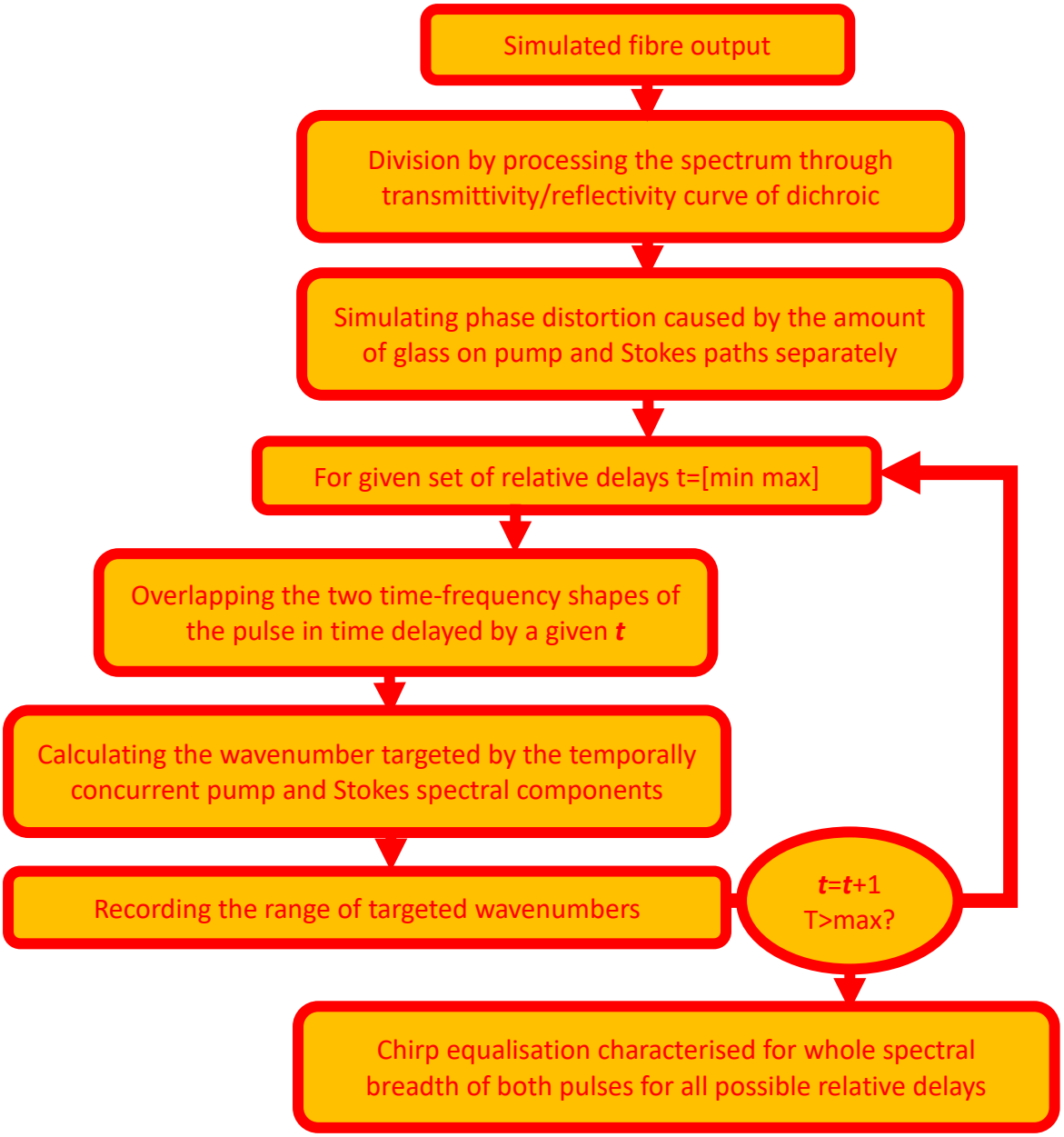

Figure 48 - Algorithm used to quantify chirp equalisation

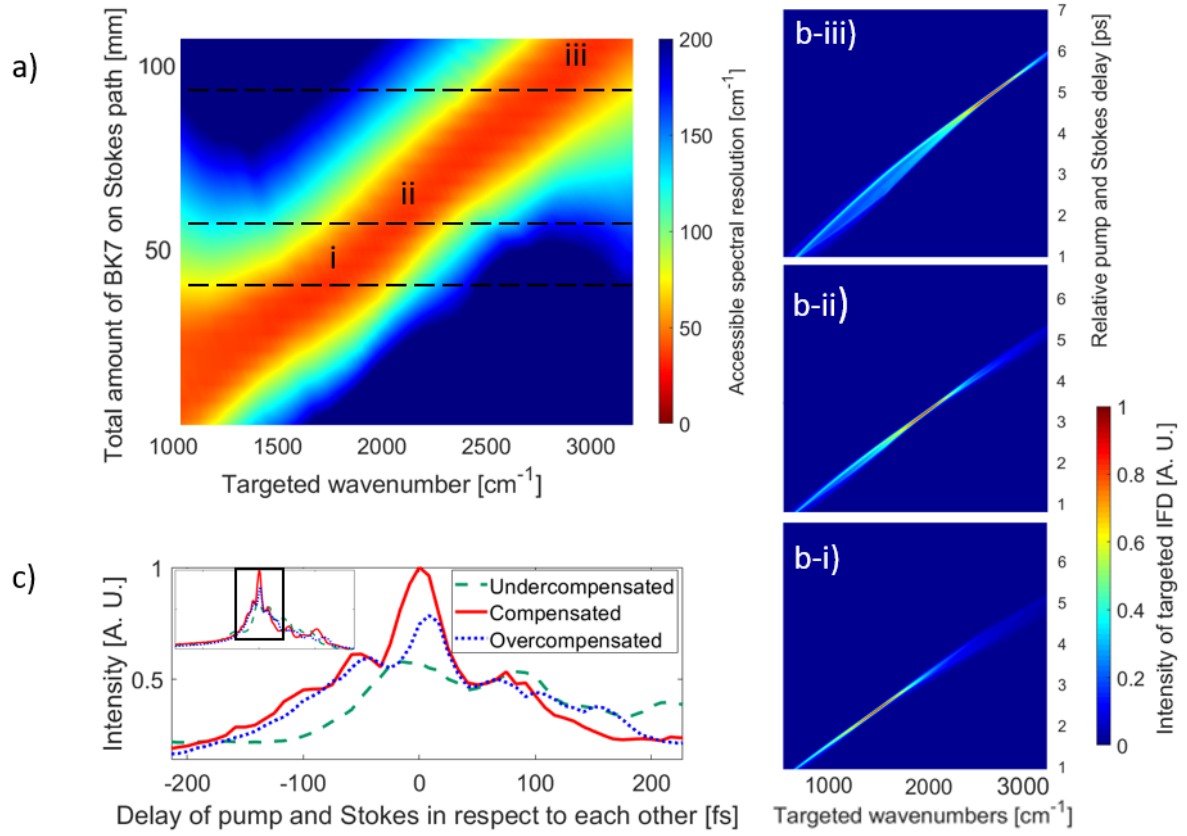

Figure 49 **- SF-CARS resolution vs. chirp equalisation (a), SF-CARS resolution across different wavenumbers for different chirp equalisations (b), SF-CARS resolution as changing for different chirp equalisations on example of targeted Deuterated Palmitic Acid 2100 cm^{-1} vibrational level**

The simulation results of the SF-CARS resolution as dependent on the BK7 glass quantity are given on Figure **49**: a) Calculated SF-CARS resolution (FWHM) as a function of Raman frequency and on BK7 added (from 0 to 120 mm). Dashed lines: i) 36 mm, ii) 60 mm and iii) 100 mm correspond to the BK7 insertion lengths used for the simulations shown in b) i-iii). b) Simulated anti-Stokes signal power vs. wavenumber for fixed amounts of BK7 in the VGEM. The BK7 lengths used were optimized for targeting the principal regions of interest: i) fingerprint region, ii) deuterated region and iii) CH region. c) Experimentally measured SF-CARS spectrum of deuterated palmitic acid with partial, full and excess GDD compensation. (Delay between pump and Stokes shown with respect to the position of the 2100 cm^{-1} peak. Better resolution and signal intensity are achieved with 60 mm of BK7 GDD compensation

than with either 24 mm (under-), or 84 mm (over-compensation). The inset shows the anti-Stokes spectrum measured across a broader range.)

Given that SF-CARS allows access to finger-print and the high-frequency CH stretching region a 30 cm^{-1} spectral resolution is acceptable wherein imaging of the main biomolecule classes such as lipids, proteins and DNA is required. However, for differentiating sub-classes of biomolecules such as saturated and unsaturated lipids or secondary structure of proteins, a resolution of better than 10 cm^{-1} is desirable. Clearly, there is a trade-off between resolution and signal strength. The complexity of the setup and the application are obvious considerations as well. For example in order to achieve a resolution of 10 cm^{-1} in our setup would have required further stretching of pulses by 3 times. This would entail having an additional 28 cm of dispersive BK7 path length in the system (common beam path; in pump and Stokes) with a further 24 cm in the Stokes beam to image the range (1000 to 3200 cm^{-1}) of IFDs targeted above. This would further require a longer delay line to be able to target the full range of IFDs (finger-print through to the CH-stretch region). More notably this would decrease the peak power that would decrease CARS (and SHG/TPEF) signal strength and hence limit the type of sample that can be imaged by SF-CARS.

4.4.2 Application of the Non-Resonant Background as characterisation of power targeting the wavenumbers of interest

Before the resonant peaks of biologically relevant samples could be targeted, setup needed to be optimised for the simpler FWM process- NRB signal generation.

The Non-Resonant Background emission has been predicted through the simulated pump-Stokes interaction using numerical model. The Non-Resonant Third Order Susceptibility has been approximated as 1. The calibration has been applied, predicting the shape of NRB in respect of the relative pump-Stokes delay. Then, the silicon sample has been introduced. Silicon does not exhibit prominent Raman peaks anywhere in the targeted 1000-3200 cm-1 region, therefore it has been safe to assume that the emission from the sample will be entirely non-resonant. The intensity of the consecutively acquired images as dependent on the pump-

Stokes relative delay can then be compared to the predicted emission. Agreement was found (see Figure 50).

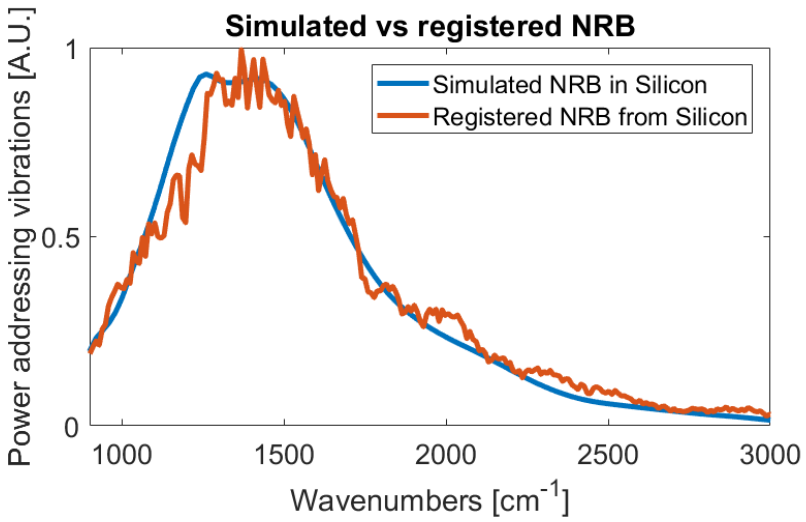

Figure 50 - Silicone sample registered NRB vs simulated NRB for 400 mW emission

Definitive proof that the signal is the anti-Stokes emission spectrum were the spectral measurements. We have approximated the shape of anti-Stokes emission for each of the relative pump and Stokes delays, and we have compared it with the registered spectra. Agreement was found (Figure 51).

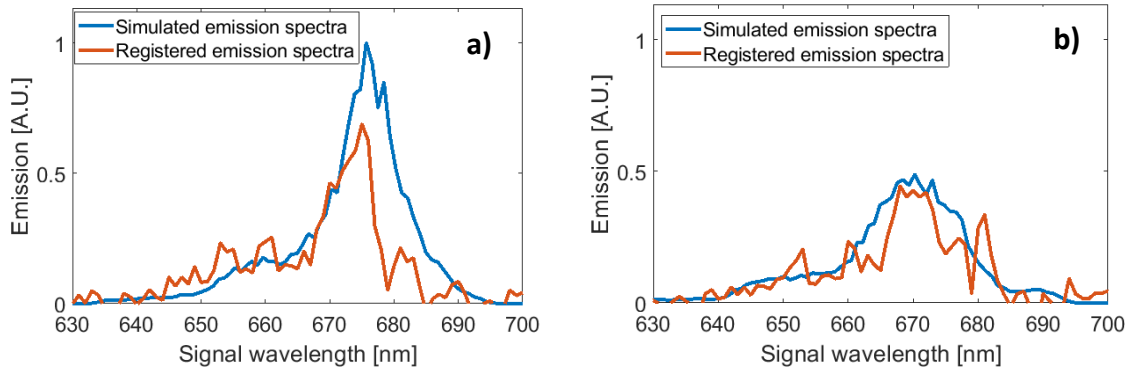

Figure 51 - Anti-Stokes NRB emission spectra measured and simulated results for relative pump-Stokes delay, that would target resonances at a) 1540 cm^{-1} b) 1660 cm^{-1}

4.4.3 SHG/SFG modality imaging

At one instant in time, due to the presence of the wavelength-offset pump and Stokes, multiple combinations of wavelengths can mix at the sample. The interaction of pump and Stokes can target resonances within the structure with the difference frequency, but it can also cause sum frequency emission.

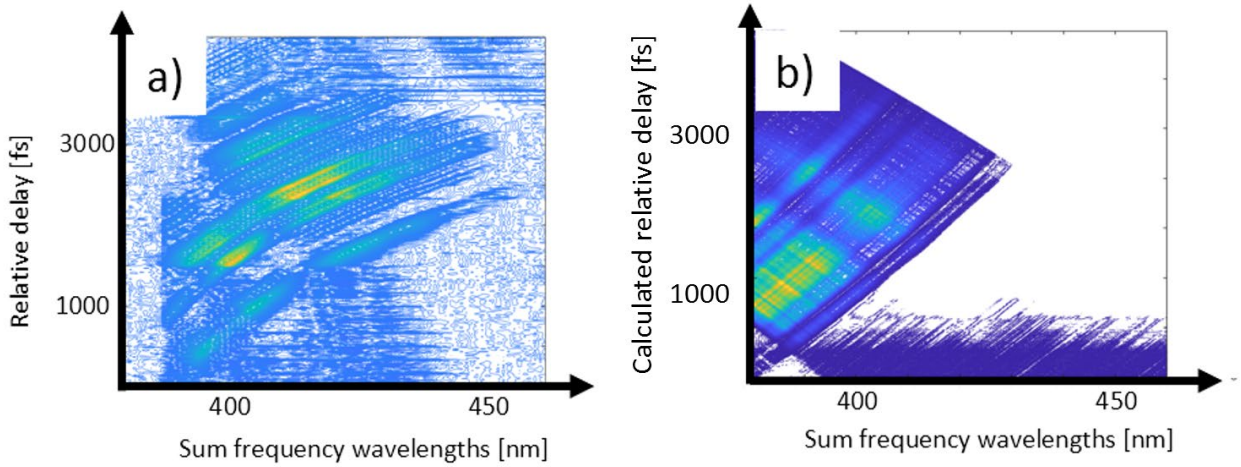

Figure 52 **– SFG for divided SC generated with 235 mW fibre output: measured (a) and simulated (b).**

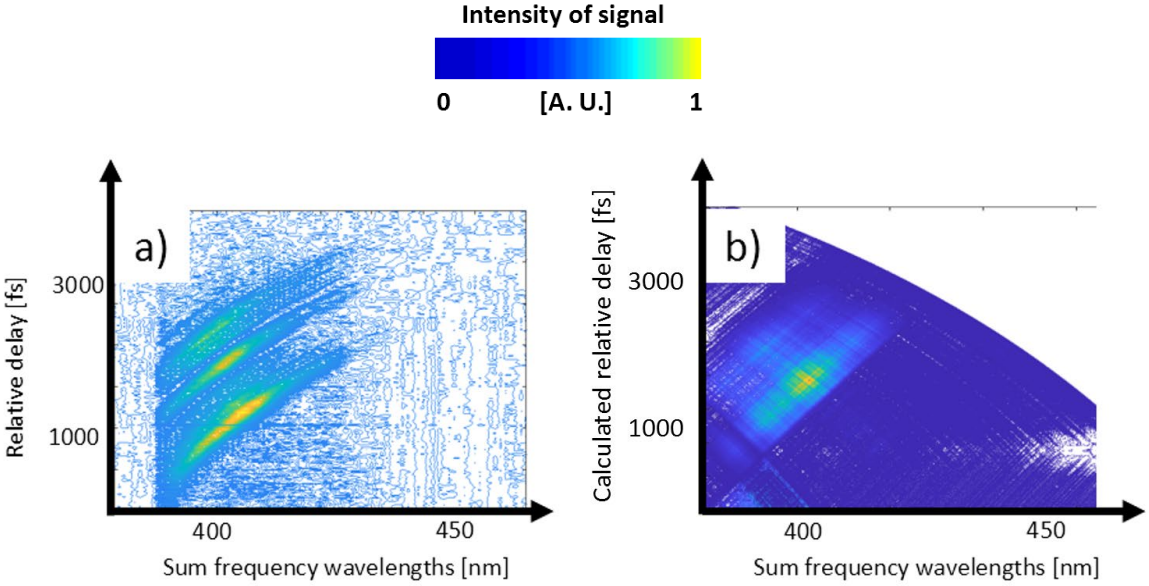

Figure 53 **- SFG for divided SC generated with 64 mW fibre output: measured (a) and simulated (b).**

Using assembled setup the pulses have been overlapped on the nonlinear BBO crystal. The result is that sum frequency spectra have been acquired for different relative delays between the pump and Stokes pulses- see Figure 52 and Figure 53. The acquisitions have been done for two different powers, 230 mW and 64 mW. The simulations were also conducted, in order to assess what wavelengths are generated. SHG/SFG modalities are different in the aspect of wavelength dependent parameters (like resolution, depth penetration). The predicted SFG spectrum has been generated using the simulated interaction between the pump and Stokes beam, but considering interaction with one Stokes and pump photons each, instead of with one Stokes and two photons from pump as in FWM.

Y-axes of the simulation plots have been calculated to present the approximate temporal overlap between the pulses, calculated from the chirp predicted for each of the pulses on the crystal (assuming Stokes pulses stretched by a factor 12 fs/nm, caused by 4000 fs^2, equivalent for 9 cm of BK7).

4.4.4 Bioimaging experiments

Biological samples were prepared by excising tissues from culled mice. All procedures were carried out in accordance with the Animals (Scientific Procedures) Act 1986 set out by the UK Home Office. Female C57BL/6 mice aged between 4-6 months were culled via CO_2 and cervical dislocation. The adipose tissue was removed using scissors and a pair of forceps. The sample was finally washed in Phosphate Buffered Saline (PBS) immediately before being mounted on a microscope slide and sealed under a coverslip (#1.5; 0.17 mm thick) before imaging. All subsequent imaging was done without the addition of any stains/dyes and can be therefore qualified as label-free.

Investigation of fatty tissue has been already proven to be key to early cancer detection [27] and to more fundamental investigation of biochemistry of lipid components [144].

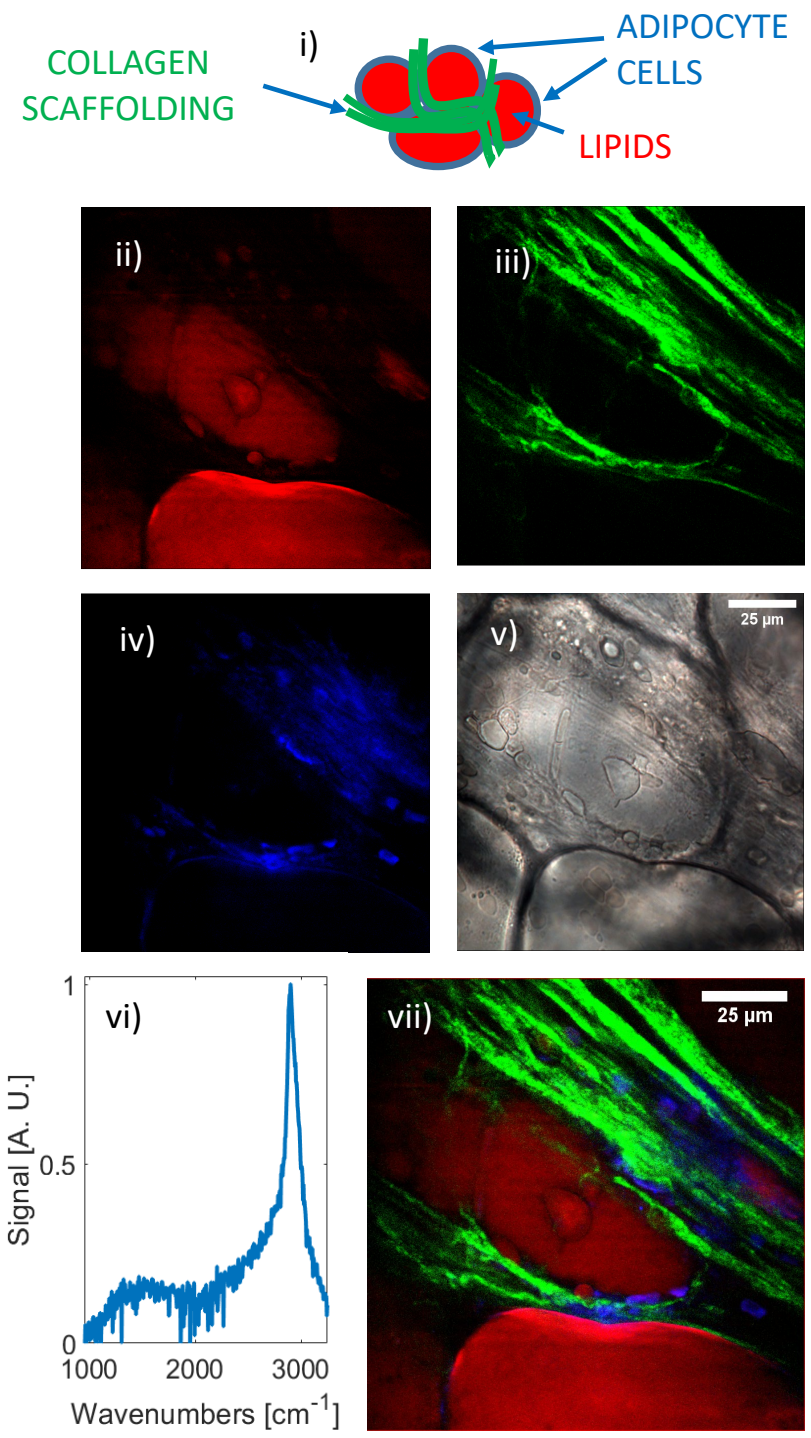

Figure 54 - Multimodal image of adipose tissue from mouse i) Schematic showing main components of adipose tissue; ii) CARS image at 2865 cm-1 inside of the cell; iii) SHG/SFG; iv) Two Photon Excited Autofluorescence; v) Bright field transmission image of the tissue; vi) Spectrum corresponding to the picture ii) in adipose tissue; vii) Composite image with CARS, SHG and TPEF overlaid.

The imaging experiments have been conducted on the biological sample of adipose tissue. The image parameters have been optimised for the best image quality, sacrificing speed for clear structural differentiation in the images presented. The resultant are multimodal: The two channels have concurrently acquired emissions from in two distinct spectral windows (380-420 and 550-683 nm). That permitted separation of SHG/SFG emitting structures of the sample and the fluorescence active elements. For spectral scans, the resolution has been sacrificed for speed, after relevant tissue fragment has been initially isolated in the field of view. The spectral scan data proves the hyperspectral capability of the setup: Changing the delay of the stage changes targeted wavenumber (see-Thymine, Deuterated Palmitic Acid and Polystyrene data, theory of SF-CARS), and that can be used to differentiate the resonant Four Wave Mixing signal (see the adipose tissue data) clearly from Non-Resonant Background.

Image acquisition was carried out in an epi-detection configuration, such that CARS and SHG/SFG images were simultaneously acquired first and then TPEF simultaneously with SHG/SFG, on our two-channel detection setup. The SHG/SFG images, since they were common to the two successive acquisitions, allowed co-registration of the images from all 3 modalities. The pixel dwell times were the same for each of the modalities indicating similarity in signal levels. Each modality provides a different chemical or structural readout. We show representative images for adipose tissue from mice in Figure 54. A schematic of the expected arrangement of different components in adipose tissue is shown in **(i).** It can be seen that the signal from the CH_2 stretching peak at 2845 cm^{-1} [39] is diffuse and not structurally dependent, as it is from uniform lipid distribution within the adipocyte (fat cell) (ii). **(iii)** shows the corresponding SHG/SFG image. Due to the broadband nature of our pump and Stokes beams we can get both SHG from pump and Stokes as well as SFG due to intra-pulse and inter-pulse combinations. We verified through spectral measurements that indeed we observed both SHG and SFG at the same time. Since SHG is a special case of SFG both interactions are via the $\chi^{(2)}$ related part of the hyperpolarizability and so are generated only in non-centrosymmetric molecules, or in structures with order so that the boundaries lead to symmetry breaking. Here, SHG/SFG have been used to selectively image collagen fibres, which are a dominant component of adipose tissue scaffolding [145], highlighting the fibrillary

nature and periodicity of collagen fibres in the sample. On the other hand, we used TPEF to image autofluorophores in the tissue that had an emission in the range of 520+/-20 nm which has been attributed mainly to Flavin Adenine Dinucleotide (FAD) and Flavin Mononucleotide (FMN) [146]. These molecules indicate metabolic activity in cells. Thus the two-photon autofluorescence (TPaF) images (iv), Adipose Tissue Macrophages (ATMs), that are metabolically active and localize in between adipocyte cells in such tissue. We verified that the TPaF signal was not delay dependent, and as such is not a four-wave mixing signal. Shape and distribution of the macrophages is similar to that observed by others [146], and our detection window covers the expected emission spectral range [147]. (v) and (vii) compare an optical (brightfield) image and the composite multimodal image of the same area of the tissue. While the brightfield image (acquired in transmission) gives only bulk morphological features the multimodal image gives the underlying chemical and structural distribution and the local adipose tissue architecture [146] through combined CARS, SHG and TPEF modalities. An SF-CARS spectrum is shown in (vi) corresponding to the lipid area shown in (ii) which shows the characteristic CH_2 peak at 2845 cm^{-1}. This confirms the selectivity of the CARS signals and the ability to acquire spectroscopic information confers a unique advantage to SF-CARS for imaging samples of unknown compositions.

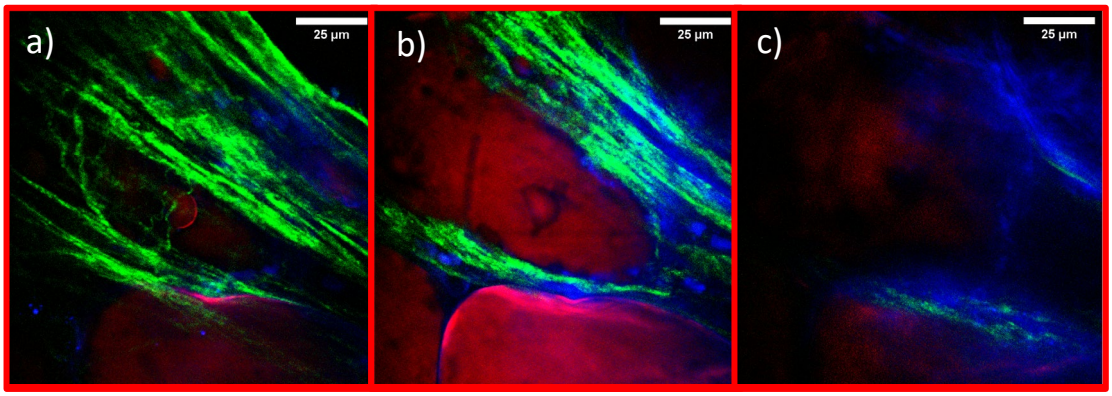

Figure 55 **- Z-Stack slices of area shown in Figure 54 vii).**

Currently tissue diagnostics makes use of coloured stains on thin tissue slices (typically 5-7 µm in thickness) imaged in a transmission configuration, and hence samples require careful preparation and sectioning. Hence, for such diagnostic applications using label-free imaging on clinically relevant thick tissue samples (fresh from surgery, for example), epi-detection would be preferable and the compatibility of the ANDi SC source with that modality presents a significant advantage.

Here we are able to show that with our fibre-enabled multimodal CARS imaging setup we can image at different depths in a thick (>25 µm) tissue sample. Z-Stack slices parallel to the composite image in Figure 54 vii) are shown in Figure **55** at depths with reference to the top of the sample of a) 0 µm , b) 10 µm and c) 18 µm. The ability to image in 3D is preferable since tissue is intrinsically three-dimensional and sectioning can miss crucial information. However, as expected the signals are weaker at depth compared to that on the surface. The depth of focus is expected to be different for CARS (3-photon process) and SHG/TPEF (2-photon processes); however, with the 1 µm z-resolution of our microscope stage we did not observe any significant effect. Overall, the simultaneous acquisition of the signals with the ANDi-fibre based SF-CARS setup shows CARS as well as multimodal imaging capability on thick tissue samples. The epi-detection capability with a fibre-based setup demonstrates the relevance to biological and clinical samples without the need for extensive sample preparation.

The structure of lipid droplets acquired is of comparable features as the ones previously described in literature [148] [149]. Furthermore, there is also a quite broad interest in adipose

tissue characterization, which opens door to wider uptake by users of the source. Currently available data in this field is as follows: Quantitative imaging of chemistry within lipid droplets has been used in [144] and [150]. The impact of collagen type and distribution on the function of the tissue has also been discussed in [151] and [145], with [146] clearly demonstrating, that some of the characteristics, such as interaction between different structures within the tissue, can be clearly resolved only with a multimodal setup.

4.4.5 Removal of artefacts caused by intensity instability

The fidelity of the acquisition is inhibited by the plethora of factors, such as: bleaching of the sample and mechanical dropping of the microscope stage. Partly that loss of intensity can be quantified using e.g. a silicon sample which undergoes the same mechanical movement as a biological sample during image acquisition. The bleaching of fluorescence from the sample, however, is not possible to standardise, as it is very sample dependent. All of these factors have to be taken into account during the subtraction stage of the image processing, as some of the fluorescence components may be erroneously left over and assigned to CARS emission. The only way to avoid that is when the CARS emission is clearly structurally different from the fluorescence emission.

4.4.6 Image processing method

There is a need for post-processing of the raw data acquired from microscopy images, for which different methods are used throughout the bio-imaging community to extract as much information as possible [132]. The broadband nature of the supercontinuum pulse causes many fluorophores within the tissue to fluoresce, as plenty of fluorophore absorption spectra overlap with the spectral components of the supercontinuum. Therefore, fluorescence caused by pump and Stokes has to be separately registered, and subtracted from the image when targeting appropriate CARS vibrational level.

There have been successful demonstrations of hyperspectral computational imaging in the past, some of them successfully, which shows how to maximize the impact of hyperspectral

CARS work [122]. They have not been explored within the scope of this project, but can be a potential extension of the work in the future.

As noted above, because the hyperspectral imaging is not done in a concurrent way, there is a possibility of sample moving slightly in between the repeated images. In order to process pictures after that happens, ImageJ software was used to align them in respect to each other using common structural characteristics (Align Objects tool).

4.4.7 Other applications of the source

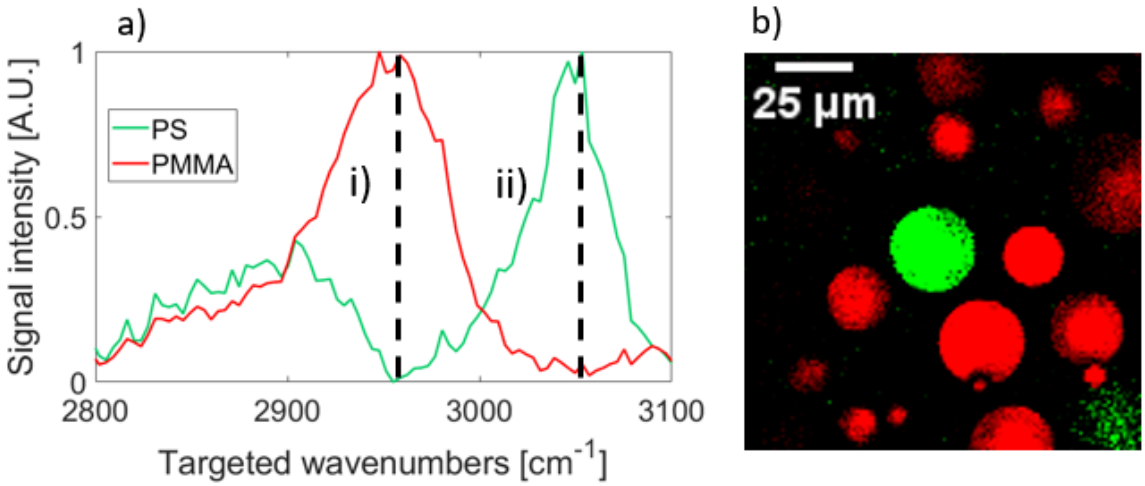

Figure 56 - Hyperspectral imaging capabilities- showing chemical specificity in CH region sufficient to distinguish between Polystyrene and Polymethymethacrylate (a) during hyperspectral image acquisition (b).

Tuning to different vibrational peaks is performed by controlling the temporal delay between pump and Stokes with the motorized linear stage (delay line). To demonstrate the changes in resulting image contrast optimization and chemically specific imaging that this enabled via a sample containing an admixture of visually identical beads made of different chemicals with closely spaced resonances (both in the CH_2 stretching region) was created with both polystyrene (PS) and poly-methyl methacrylate (PMMA) beads. These materials are indistinguishable using white-light imaging but are clearly segregated with SF-CARS as seen from the recorded SF-CARS signal vs. wavenumber in Figure 56. a) Shows SF-CARS spectra after background subtraction corresponding to two different beads from the same sample.

The dashed lines correspond to the peak positions of i) 2957 cm^{-1} and ii) 3054 cm^{-1} associated with the two materials. b) shows the corresponding image with SF-CARS intensities at IFDs of 2957 cm^{-1} (red) and 3054 cm^{-1} (green) respectively that allows differentiation between the two types of beads. This demonstration is similar to the broadband CARS data in Ref. [152], and shows that the ANDi SC herein in capable of matching the state of the art in the field. The images clearly show the benefit of spectrally selective 'fingerprint' imaging modalities such as CARS as well as showcasing the way the ANDi fibre extends the capabilities of standard Ti:Sapphire lasers.

The challenge currently facing the environmental sciences concentrated on the oceans clean-up from microplastics is an identifying and imaging the contamination in a chemically specific way would enable both research and sorting for recycling purposes. The detection of microplastics in flow can be crucial for a more robust analytical support of ocean clean-up, which would be made possible by far better mobility of the laser source used in this work in comparison to most of its predecessors. It has been done using Raman [153], but not yet any coherent Raman techniques. CARS signal strength would provide sufficient characterisation speed, so as to conduct the sorting while the water flows through the focal volume of the relevant objective. This development would be key to sorting of plastic waste filtered out from the water into appropriate recycling pathways.

To enable an automated system to distinguish between different kinds of plastics Principal Component Analysis (PCA) can be used, results of which are presented on Figure **57**. There is a clear difference between the components, and this opens possibility to distinguish between different plastics not only on dried samples, but also in the flow.

PC4 is clearly Polystyrene, as it is the only one with two distinguishable peaks in C-H region (3050 cm^{-1} and 2890 cm^{-1} respectively). PC2 is PMMA, as it is broader than any of PS peaks and centred between them (which is consistent for a 2960 cm^{-1} maximum signal position). Finally, PC3 is Low Density Poliamide (LDPA), which has a double peak structure at 2875 cm^{-1} and 2850 cm^{-1}, which is not resolved here. X scale is calibrated using previously established

method. This continues that indeed PCA stack analysis can be successfully used for calibration, without manual input by an end-user.

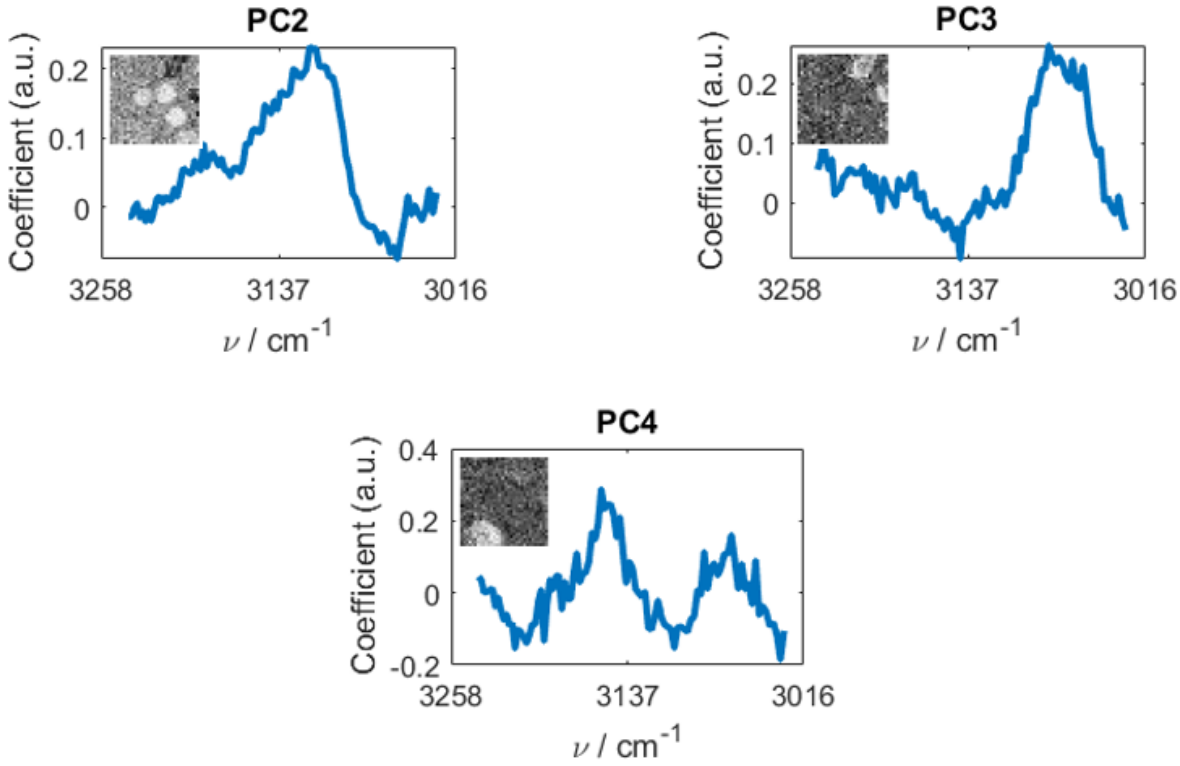

Figure 57 **- PCA results showing spectra and pictures showing associated deconvolved area of picture associated with only one kind of plastic- PMMA (PC2), LDPE (PC3) and PS (PC4)**

As a final demonstration of the capabilities of the ANDi SC source for CARS, the polarisation-selective ability is shown by using polar-CARS [154] on a Thymine sample. Hence, as thymine and lipids have similar Raman resonance frequencies, the ANDi SC source would also support lipid membrane imaging with polar-CARS (Figure 58).

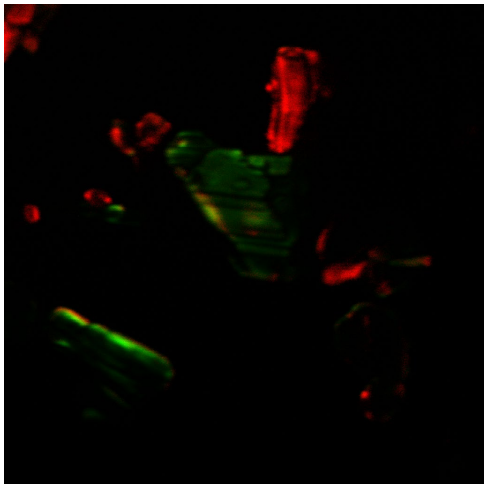

Figure 58 - polar-CARS of Thymine crystals, where green and red are signals for two orthogonal polarisation of incoming pump/Stokes beams (parallel to each other)

4.6 Summary

In summary, we show for the first time that a length-optimized ANDi microstructured fibre can be used (retrofitted) with the typical workhorse, 100 fs Ti:Sa seed laser from multiphoton fluorescence imaging setups, to realize a simple yet powerful source for spectral-focusing CARS and concurrent SHG/SFG and two-photon fluorescence microscopy in an epi-detection geometry. Rapid and accurate tuning between resonances was achieved by changing the relative delay of pump and Stokes pulses via a motorized high-precision linear stage. Minor challenges remain such as polarization noise documented in Ref. [155], but a polarization-maintaining version of the fibre could be used in the future, subject to availability from the manufacturer. Numerical simulations of the interaction between pump and Stokes showed clearly the influence of the dispersion from the optics on the nonlinear chirp of the pump and Stokes hence providing crucial guidance on the length of glass to be used for GDD equalization in the Stokes beam. The resulting spectral resolution achieved was ~30-40 cm^{-1}, which is close to the maximum achievable considering the spectrum used and stretching of pulses. The continuum was generated from a 9 cm length of fibre and imaging was achieved at Raman frequencies from 900-3200 cm^{-1}, i.e. spanning the fingerprint region and the CH-stretching region, both of which are critical for bio-samples., when seeded by our standard 100 fs Ti:Sa laser.

We build on the understanding of the length dependent properties of the continuum from Ref. [156] (also partially discussed in [157]) and transferred the capability, used in Ref. [106], that incorporated an expensive pulse shaper to perform multimodal epi-imaging, but we use only glass blocks for matching the chirp of the pump and Stokes pulse, as in Ref. [61]. Hence we have reduced cost and complexity while still enabling high Raman resolution to be achieved throughout the CARS spectral ranges targeted. Critical to our work was the use of a MOF with precisely tailored length, chosen by a combination of experimental work and detailed numerical simulations instead of the approximate analytical approaches used in earlier work [57] [56]. Overall, our approach provides several benefits at reduced complexity while at the same time it enables imaging of clinically relevant thick samples.

5 ANDI FIBRE COHERENT SUPERCONTINUUM FOR MULTIPLE FLUOROPHORE TPEF IMAGING

5.1 Introduction

For the nonlinear TPEF using different fluorophores, different wavelengths are needed to target different excitation ranges [158]. These wavelengths, which are typically in the range 700-1000 nm are usually provided either by Ti:Sapph lasers or by fs laser driven OPOs. However, the most popular laser sources do not provide the wide wavelength range (only 10-20 nm pulse bandwidths are required for a pulse temporal width of order of 100 fs) hence one output can be used to excite only one of the fluorophores. As different parts of the sample require different labelling agents [7] this shows the need for a broadband laser source for multiple TPEF excitation in order for rapid imaging. That shows potential overlap with the other Supercontinuum work presented in previous chapters, and motivated us to pursue the potential for applying our source to this kind of bioimaging.

Existing solutions for that purpose are use of MaiTai-type Ti:Sa lasers, which are tuneable between multiple wavelengths. However the time it takes to change the emission is long in comparison with image acquisition times (order of seconds vs order of μs per pixel). Other systems use arrays of CW lasers, but that lacks the advantage of TPEF. Current supercontinuum-based sources for multi-wavelength fluorescence provide incoherent, hard to compress output whereas the ANDi fibre coherent spectrum can be potentially compressed (transform limited pulse FMHW duration of pulse around 200 nm broad is of order of 10 fs [108]). Therefore this is a niche for the TPEF market that can be targeted with the ANDi SC system.

The optimum laser pulse has to be intense enough for optimum SHG and TPEF excitation, but not intense enough to cause damage within the tissue. The influence of pulse duration for bioimaging has been investigated e.g. in [159]. Clearly visible is that the optimum pulse duration is in the fs, rather than the ps range. This is much shorter than the pulses used in SF-CARS case, raising the need for compression.

A lot of work in the field has been done by the Dantus group in the USA [160], which resulted in a commercially developed SLM for phase and amplitude modulation, resulting in close to transform-limited pulses at the focal point of the microscope. Important step forward in compression of a broadband laser pulse was also done by Heidt [108].

There has been work done on the compression without the need for an SLM previously, most notably by Jeff Squier [161], who developed GRISM technology in order to obtain flat phase pulses, potentially showing the way towards gratings and prisms as a potential useful tools in compressing a broadband pulse. However, using of simple prisms decreases the cost of the setup as well as alignment difficulty considerably, so for our application based design it was deemed useful to try to quantify signal improvement, that can be provided with that approach.

In order to optimise the compression, the pulse duration has to be quantified. However, the characterisation of a broadband pulse poses problems in itself. One possible solution, angle-dithered approach, has been developed by Trebino [115] which resulted in a broadband FROG, however that technology is not available to us. The autocorrelation of a pulse at the focal point of the microscope is also challenging, because of small (<200 μm) working distance of the objective and the necessity for a thin crystal. Because of that limitations, autocorrelation (see **5.3.3 Compression experiments for SC generated at 1055 nm** with a thick crystal) and SHG emission intensity (see **5.3.4 Theory vs experimental results for compression of SC generated at 800 nm)** have been applied in the work.

Two sources has been used for the SC generation in the fibre – 1055 nm fibre-based source, and a 800 nm Ti:Sapph laser. These wavelengths were chosen as popular, commercial sources very often operate in this regime, consistent with mentioned TPEF excitation range.

The work on 1055 nm pumped fibre has been done during the first year of my PhD. That source has not been equipped with an imaging platform, therefore one was constructed, as detailed in 5.2. However, the signal emission from the sample was very low, which raised the requirement of compression. Preliminary imaging data has been then recorded and analysed.

The compression was then progressed parallel to the CARS work, which was prioritized as most promising for significantly benefiting researchers due to its label free nature (see **4 Application of tailored-continuum from ANDi-fibre for label-free bioimaging with SF-CARS.**

The work on the 800 nm pumped fibre was done following the work on CARS. The main focus has been optimising the pulse duration at the focal point of the microscope, using SHG emission as the benchmark. Modest improvements over the 800 nm laser output did not merit proceeding to fluorescence intensity measurement or imaging. Compression experiments are detailed in section 5.3 and 5.4.

Presence of dispersion in the microscope optics and dispersion management in the compressor is made hard due to broad spectrum involved. For such a broadband pulse, even slight misalignements or chirp undercompensation can cause orders of magnitude changes in duration

. It had far less influence in the SF-CARS experiment, where broadband pulses were already of the order of picoseconds, and therefore less prone to temporal broadening .

In order to partially account for that, the behaviour of the broadband pulse in the optical system has been analysed, and modelling code has been applied to simulate the effect of the prism pair, a proven technology used to pre-compensate for the chirp at the focal point of the microscope [162].

Some guidance has been provided through the analytic approach of Fork and Shank [120], but narrowband pulse approximation was not valid for our purposes. Therefore, the model used for CARS work has been upgraded to include a prism compressor to account for the dispersion of the microscope optics.

The possibility of reducing the detrimental influence of higher order residual chirps through selective compression of just a portion of the SC spectrum is detailed in section 5.5.

5.2 SC excited multi-wavelength fluorescence with 1055 nm pump laser

In order to explore the potential of TPEF imaging using the SC, an experiment was conducted to show that the two photon emission of fluorescent markers Rhodamine 6G (peak two-photon absorption close to 800 nm [163] [164]) and Cy5 (two-photon absorption above 1000 nm) was possible concurrently. To that end, fluorophore solution was placed in the beam and the signal was detected at the edge of the cuvette.

A side collection setup of the TPEF signal (which was attempted at first) is much less efficient than transmissive collection, on the account of aberration caused by the edge of the optical cuvette. Even collection of the signal in transmission is challenging as two photon emission is more probable to detect at the front surface of the fluid, because the self-re-absorption of the signal by the solution can decrease the amount of fluorescence detected if the propagation path includes many fluorescent molecules [165].

Therefore, robust spectroscopy required a thin sample holder in a transmission setup. The fluid cell for the purpose of the experiment was filled firstly with Rhodamine, then with Cy5 aqueous solutions. The laser was isolated from the signal using a dichroic filter. The final setup is presented in Figure 59.

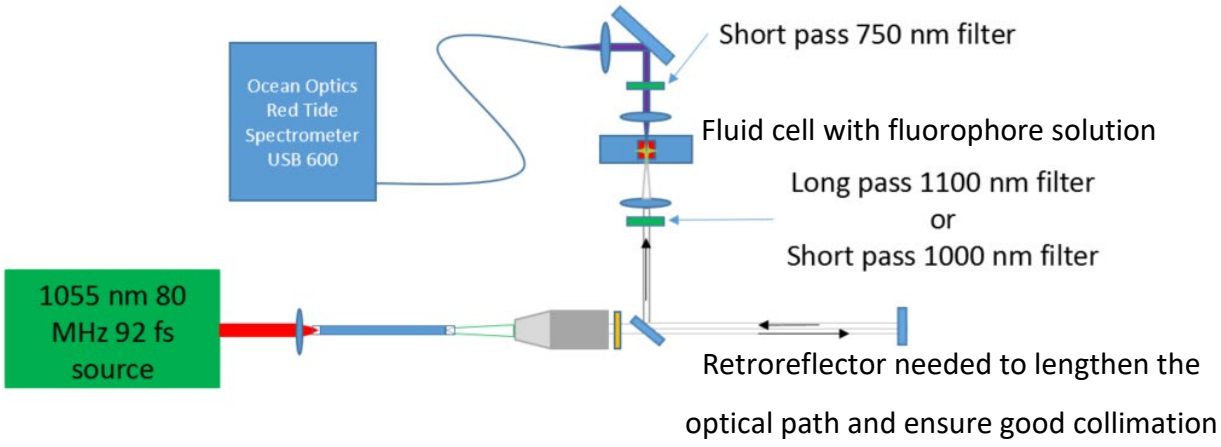

Figure 59 – Fluorescence spectroscopy setup built on basis of 1055 nm source. Long pass/short pass interchangeable filters, permit isolation of different spectral ranges of SC.

Figure 60 shows the Two Photon Absorption Cross Section curves superimposed on the 100 mW spectrum out of 85 mm NKT ANDi fibre. This length was chosen for all the 1055 nm pumped TPEF imaging results shown in this thesis because it produced the appropriate spectral bandwidth to excite both Cy5 and Rhodamine 6G and had a phase profile suitable for pulse compression with a pair of SF11 prisms. The research in [108] suggests that the compressibility of the pulse is achieved when the propagation distance is equal to wavebreaking length, as the high-order chirp is minimised, so that the phase distortion is closest to being purely quadratic. As the prism compressor corrects most of the second-order phase distortion, that output is preferred for that compression method. This leads to the conclusion that the best pulse compression will be achieved if the length of pulse propagation in the fibre would be equal to the wavebreaking distance. In order to estimate if the bandwidth of such a pulse would be appropriate for our purpose, the WB bandwidth for the seed pulse parameters available from our 1055nm laser source was estimated and calculations showed it was necessary to change the length of the fibre, so that one can still achieve acceptable 200-300 nm broadening, and still achieve mostly second order chirp. The length of the fibre used in the experiment was on that basis set to 85 mm.

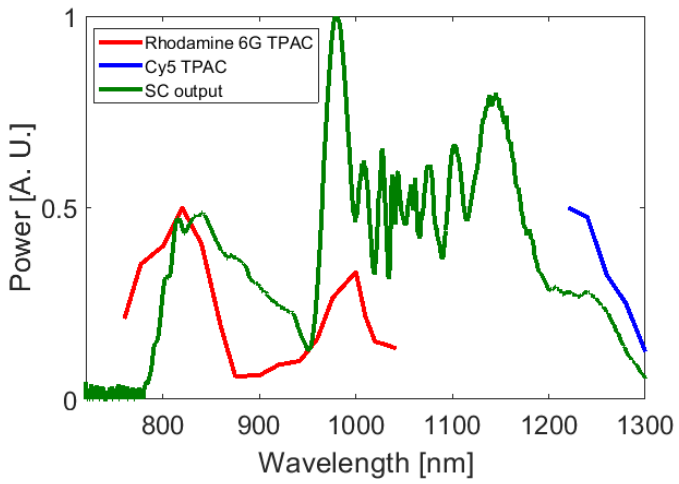

Figure 60 - Two Photon Absorption Cross Section (TPAC) Curves superimposed on the 100 mW emission spectrum out of 85 mm NKT ANDi fibre

Figure 60 gives limited information about the TPEF cross-section of both used fluorophores, however it was experimentally checked that while the Rhodamine 6G fluorescence has been excited by the 1055 nm beam, that was not the case with the Cy5. However, using filtered supercontinuum it was possible to excite and record spectra from both of these fluorophores. This plot illustrates one of the most important practical aspects of the coherent supercontinuum – the capability of targeting multiple fluorophores at the same time.

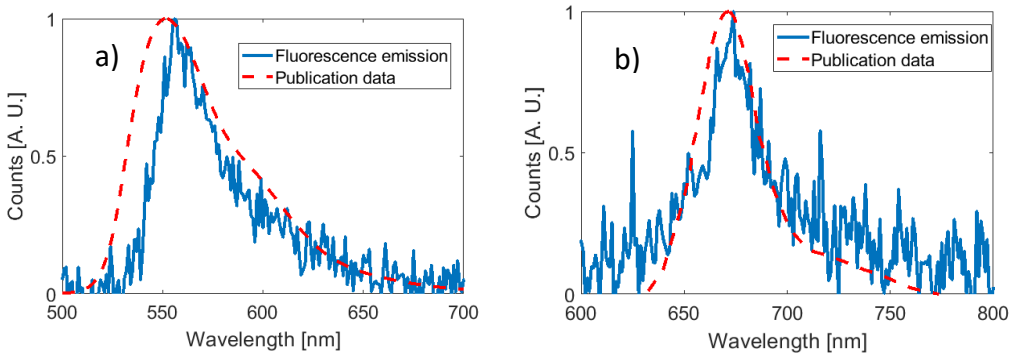

Figure 61 - Recorded fluorescence emission spectra (averaged, background subtracted) excited using selected spectral ranges of the supercontinuum for Rhodamine 6G (a) and Cy5 (b). Experimental data (cosmic ray spikes removed) are overlaid with the published fluorescence profiles.

The data from the experiment is shown on Figure 61. Rhodamine 6G was excited with wavelengths shorter than 1000 nm (100 mW out of the generated SC power), and Cy5 was excited with wavelengths longer than 1100 nm (150 mW of the generated SC power). The dashed line shows the published Rhodamine [166] and Cy5 [167] emission spectra for comparison.

The small shift between the predicted and registered fluorescence profile is most probably caused by the difference in the solvent used- the published data used ethanol, and in described experiment we used water. Different solvents have been shown to cause shifts in the fluorescence profile [168].

In order to record the above fluorescence signal using uncompressed SC as the pump source, the acquisition times had to be of the order of 40-50 seconds, due to the chirp.
The resulting emission intensity in was of up to the order of 3x larger while using the much shorter pulses from the pump laser rather than using SC for the same average power.

This result shows that the advantage from SC overlapping with the excitation of Rhodamine is mitigated by the decreased peak power available. It was therefore decided to recompress the SC to improve the TPEF excitation efficiency.

5.2.1 Methods

The next experimental step was to apply the SC for 2D scanning fluorescence setup.

The detector was an iDus CCD camera mounted on the Shamrock 303i spectroscope. The camera was cooled to -80 degrees in the setup, which considerably reduced background, so that longer acquisitions could be taken without background oversaturating the camera.

The coordination of scanning stage and the spectrometer was achieved using an in-house made algorithm in LabView. The LabView program controlled the movement of the stage according to set step size. After each step was taken, the spectroscope was triggered through the generation of DAQ TTL trigger signal, and the acquisition was conducted. The Kinetic Series mode provided by Andor Solis software made it possible to start acquisition series of predetermined length, each acquisition triggered by software.

After the setup was aligned, the piezo-controlled scanning stage was installed. The focusing 40x objective (NA=0.64) and the signal collimating 10x objectives were then placed in the system. The high numerical aperture objective lens provided higher intensity at the excitation point, and the high NA signal collection provided wide collection angle of incoherent signal emitted in all directions. Firstly, the pump laser was attenuated considerably, and then the beam was aligned with the spectroscope. Then, the sample was inserted. The glass slide with deposited fluorophore Rhodamine 6G (so called ‘island film’ [169]) was placed orthogonal to the path of the beam. The final imaging setup is shown in Figure 62.

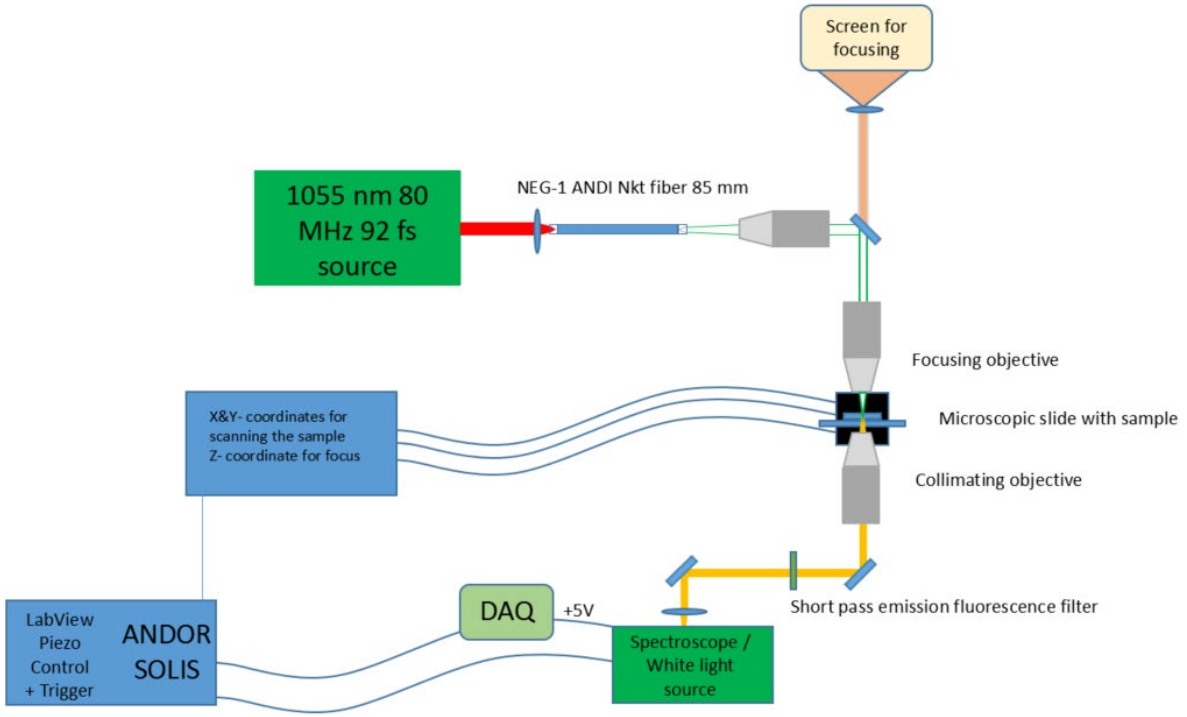

Figure 62 – Scanning microscopy setup based on SC fibre pumped with 1055 nm 90 fs laser source.

For rough focusing on the sample, a white light source was applied in a back transmission setup, so that the image of the sample was projected on the screen. Focusing was possible via the micrometric displacement in Z direction, and the sharp image of the slide surface visible on the white screen was an indicator of accurate position of sample in relation to the focal spot (see 4.4 Imaging experiments**)**.

The average power used for this preliminary investigation was **50 mW**. The acquisition time used was 10 seconds per pixel. A 10x10 grid was acquired, which with a step size 0.5 µm corresponds to the 5 µm by 5 µm square area. The spot size from the 40x objective with Numerical Aperture 0.65 was calculated to be of the order of 2 µm. Algorithm applied was that the stage was moved in a way that the sample will be scanned as shown in Figure 63. After each movement, the trigger signal was sent to the spectroscope, and a spectrum was automatically saved for each of the points of a pre-defined grid, parameters of which (step size, number of steps, acquisition series length were set by user using the assembled code. Acquisition time had to also be coordinated between spectroscope and the mechanical stage-

each time after a move is triggered, a delay equal to acquisition time is applied. Afterwards, the setup requires no operator intervention. Next, assembly of an image is conducted using customized MatLab code which assigns spectral intensity (number of counts) to the position of the focal spot as relative to the sample.

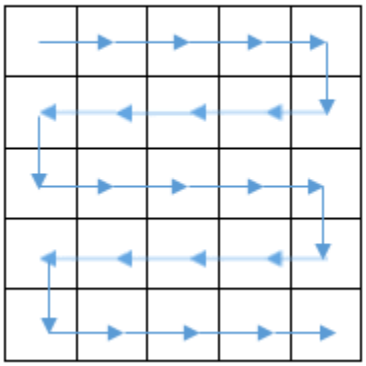

Figure 63 - The path of scanning beam across the sample (schematics)

5.2.2 Two Photon Excited Fluorescence (TPEF) imaging results

Spectrum acquired from one point of the grid is shown in Figure 64, together with superimposed background.

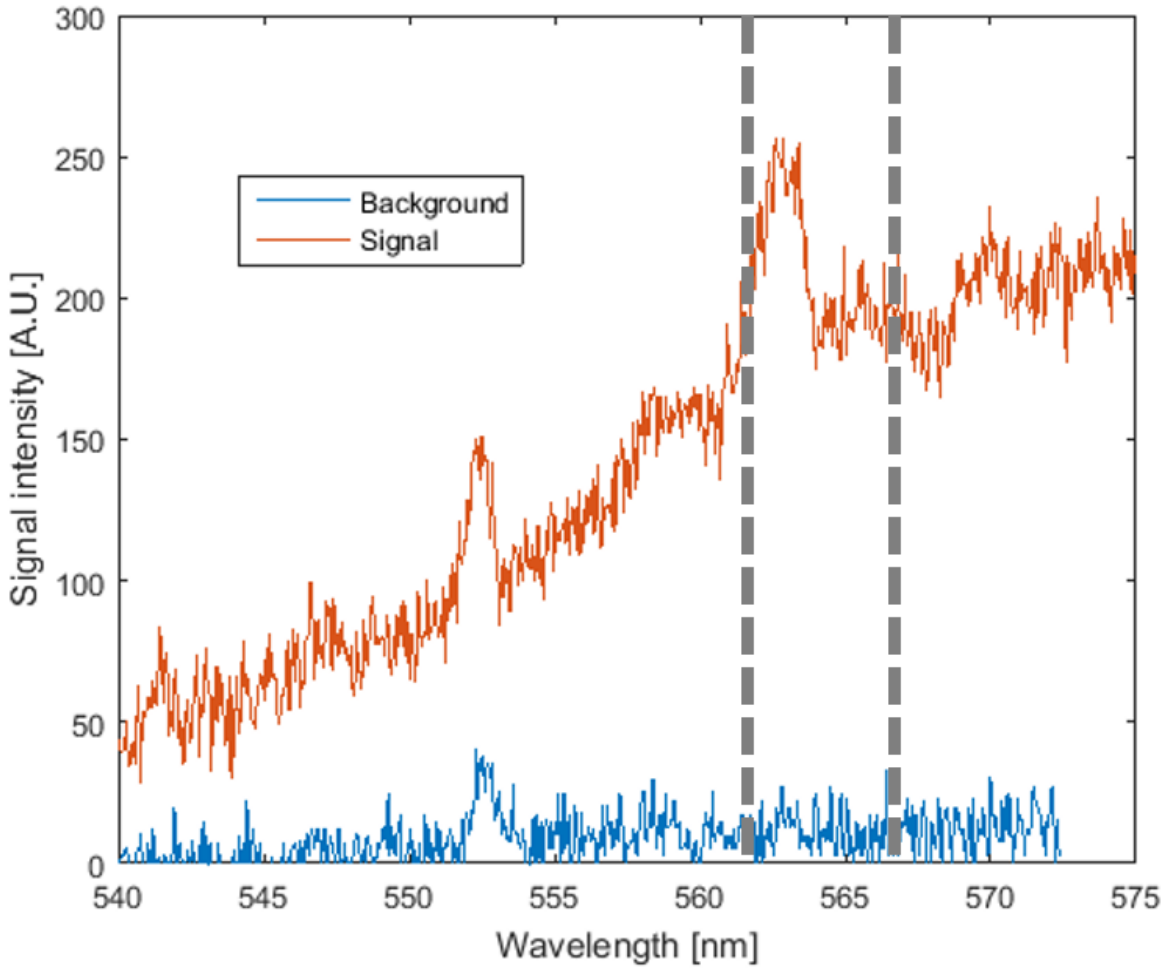

Figure 64 - Spectrum acquired during scanning, superimposed with background spectrum

Background was acquired under the same experimental conditions- presence of a glass slide, but without fluorophore present. The image was constructed by isolating the 562-567 nm range and analysing the total counts in this range. This resulted in the image shown in Figure 65.

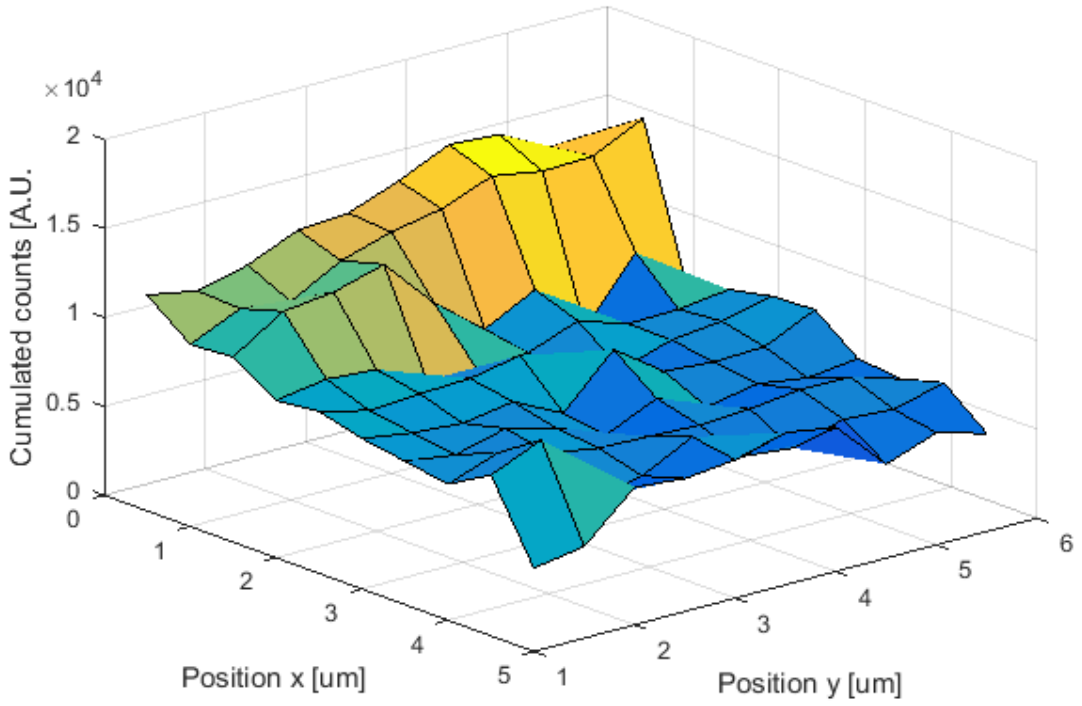

Figure 65 – Spectral intensity fluorescent image of the artificially prepared fluorophore-rich sample

There is some doubt whether we can conclusively claim that we have observed TPEF. One of the factors influencing this statement is the low signal to noise ratio, obstructing fluorescence characteristics. The stability of the position of the focus on the slide has also been put in question, as no repeatability study of it has been done after the beam has been focused on the sample. Another possible reason is that the light pulse out of the fibre was additionally temporally broadened after passing through 3 microscope objectives, to the degree that Two Photon Emission is extremely low, as the pulse peak power would be 3 times lower than at the fibre output because of the additional chirp of order of 1600 fs^2, caused by the collimating and focusing objectives. Therefore, it would be natural as a next step to repeat the experiment using successfully compressed beam.

5.3 Compression results

5.3.1 Novel prism compression code applied

An in-house code was written by the author to assess how the broadband SC pulse is being compressed using prism setup, and is presented in the appendix. Previous approaches to prism compression did assume spectrally narrow pulse, e.g. 2 nm spectral width in the fundamental paper [120]. The narrowband condition is not fulfilled in our case. What was novel in our simulation was the geometrical approach to beam paths, first time to our knowledge taking into account higher order dispersion effects in a way more accurate than previous analytical approaches.

Chirp at the fibre output and the predicted phase distortion from the microscope optics was established via the simulation, chirp of the prisms was modelled and the optimum prism distance for compression of broadband pulse was calculated, then the pulses were optimised experimentally.

The refractive index for both prisms (SF11) and the dispersive material at the path of the supercontinuum (approximated as BK7) have been calculated on a 0.1 nm grid for wavelengths within the SC spectrum using formula and factors from the Schott catalogue [143], and from that the optical path differences between wavelengths have been calculated, and from that the temporal phase distortion has been calculated. From the shape of phase distortion, chirps of multiple order have been established.

The pulse temporal shape upon exiting the fibre is taken into account. Influence of phase distortion from the glass on path of the beam and the phase distortion caused by the prism compressor is taken into account, and the resulting peak power and temporal FMHW duration was quantified. The SHG signal from compressed pulse was then predicted as dependent on the prism separation. Spectral breadth of supercontinuum strongly influences the possibility of compression of a given pulse- both as limited by the third order chirp and by the size of the second prism. The size of the prism is responsible for clipping of some spectral components

from the edge of the spectrum, which with spectrally broad pulses and large relative prism distances is especially significant, hence large prisms with 4 cm sides have been used.

5.3.2 Compression simulations for 1055 nm

The simulation code was originally applied for calculating the pure 2nd order GDD that lead to highest peak power- to simplify the calculation, higher order chirp caused by the compressor itself has not been considered. The compression software (written by P. Horak) was then applied for simulating best possible chirp correction of the pulse. The phase distortion extracted from the simulation after post-processing and fitting the polynomial to the spectral phase plot is shown on Figure 66. The trailing edge of the simulated compressed pulse confirms the presence of uncompensated third-order-dispersion effects [170] (Figure **67**). The pump pulse parameters used in simulation were as follows: pulse width 92 fs, repetition rate 80 MHz, central wavelength 1055 nm. These parameters correspond to pump laser pulse parameters used in later simulations.

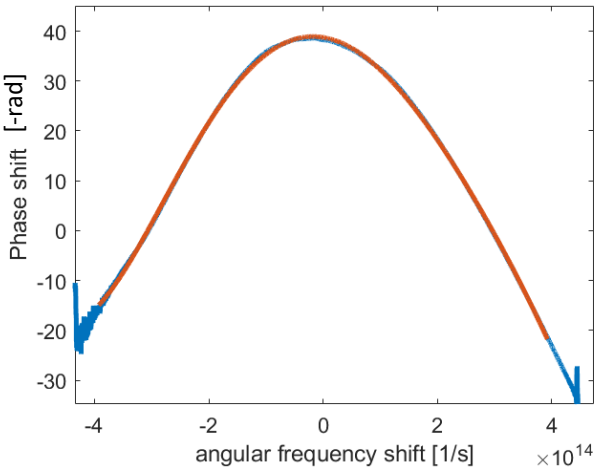

Figure 66 - Phase shift in radians at the output of simulated 85 mm ANDi fibre piece (100 mW average power, blue) and fitted polynomial approximation (orange). On basis of polynomial fitting GDD= 504 fs²

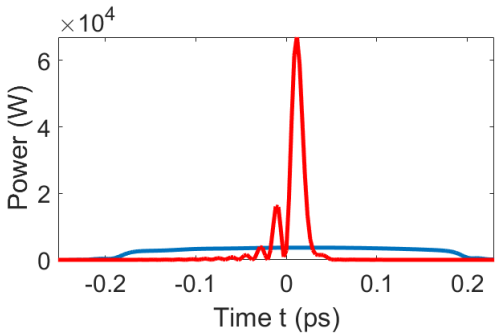

Figure 67 - The simulated SC out of 85 mm ANDi fibre piece (100 mW average power) pulse shape after applying compensation tuned to the extracted pure quadratic phase distortion (red) and original shape (blue)

The approximations used by Fork & Shank in estimation of their phase distortion are given under assumption that the wavelength spread in the input pulse was small (for the 2 nm spectral width the spread at the output of first prism is significantly lower than 10 deg, allowing for small angle approximation). In case of spectral spread involved in achieved SC generation (ca. 200nm) the simplification breaks down. Hence a numerical approach was implemented in order to calculate continuous phase profile for the prism compressor. The optical path calculated for the prism setup is consistent with simplified approach of Fork & Shank for central frequency, but starts to diverge for the side lobes of the spectrum. Moreover, the broad spectral range is causing additional problems experimentally- after being dispersed by the 1st prism, the beam is highly divergent. For the prism separation considered in this work, this causes clipping of the spectrum, as it spreads over a larger distance than the length of the side of the second prism causing spectral filtering, and needs to be considered in the simulation.

Some approximations had to be used for this simulation. The two prism facets have to be parallel to each other in order for the formulas to appropriately describe reality. The consequences of misalignment of prisms have been discussed extensively in [171], which include e.g. uncompensated spectral spread.

5.3.3 Compression experiments for SC generated at 1055 nm

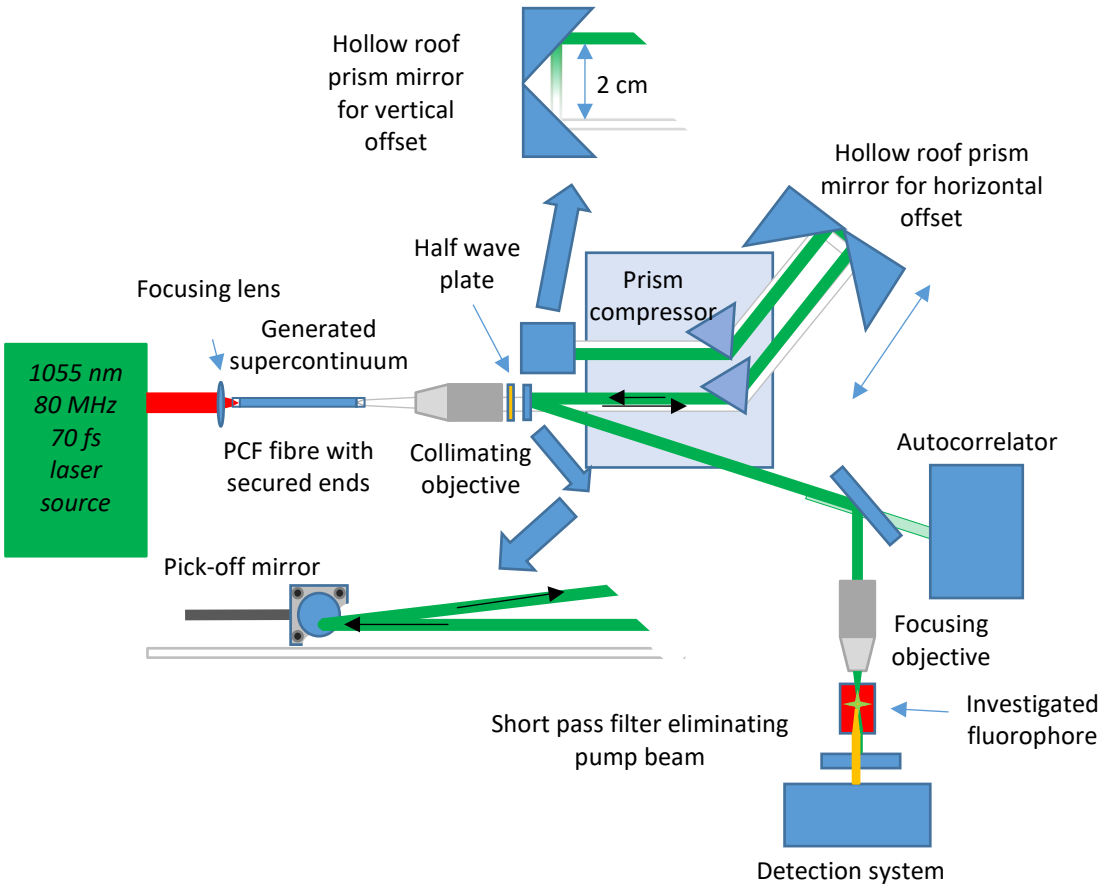

Figure 68 - compression setup for 1055 nm pumped SC

A compression set-up has been built (Figure 68) in order to reduce the temporal duration of spectrally broadened supercontinuum pulse. The prisms applied in this setup were made out of SF11 glass. Gold coated hollow roof mirrors were used as retroreflectors, because of their good reflectivity across the spectral range of interest. The compression has been assessed with a SHG intensity autocorrelation measurements. The precision in prism separation adjustment was provided by using a micrometre positioner and a linear stage.

Autocorrelation of this SC light was then conducted. The best compression has resulted in measurements of above 44 fs deconvolved FMHW duration (while assuming Gaussian pulse

shape). That proves, that tailoring of SC using prism setup was partially successful, at the same time presenting proof of the SC having high coherence. Then, the dependence of the pulse compression on the prism separation was plotted (Figure **69**).

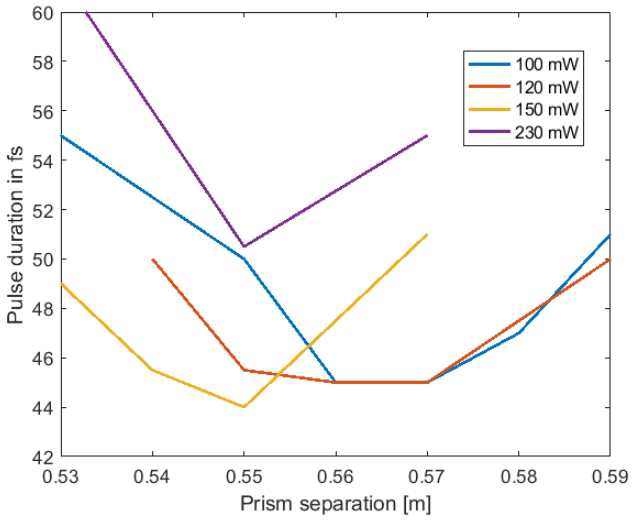

Figure 69 **- Dependence of the compressed pulse time width in respect to the prism separation for different powers of generated SC**

The prism separation required for pulse compression diverged from the simulation predictions, suggesting that high-order chirp from both the dispersive elements in the beam path and the prism compressor itself needs to be considered.

5.3.4 Theory vs experimental results for compression of SC generated at 800 nm

Firstly, the compression of 10 nm bandwidth Mai Tai beam, centred at 800 nm has been attempted. A pulse width of 130 fs has been measured using the intensity autocorrelator. The pulse after propagation through the amount of glass in the path of the beam would be 190 fs at the focal point of the microscope, as assessed through simulation. Having established this pulse duration of the pump laser before and after the microscope optics as a datapoint for comparison, the next step was to attempt to better it via SC pulse compression has been on Figure 70.

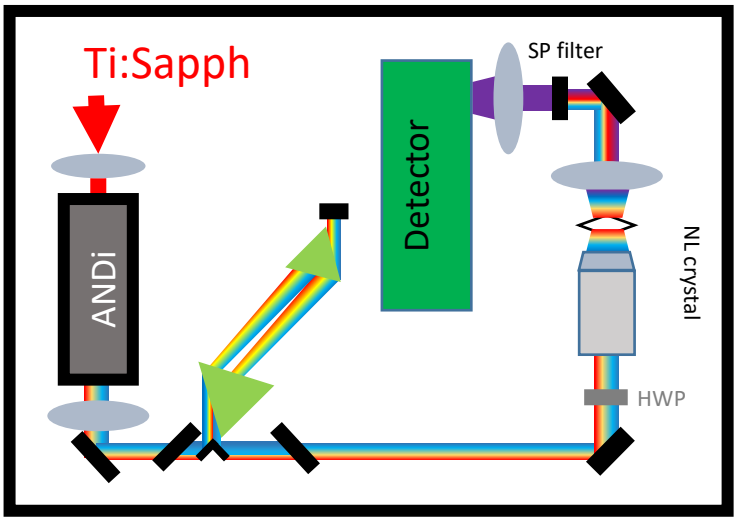

Figure 70 – Setup for quantification of compression of the SC generated from 800 nm pump beam

As a metric of our pulse duration, SHG signal intensity averaged over the whole investigated sample has been taken both for the simulations (Figure 72, Figure 73) and for the experimental results presented (Figure **76**, Figure **77**). The 'uncompressed laser' is the MaiTai 190 fs laser pulse of same average power as the SC in question. The SHG excited by that recompressed MaiTai pulses has been also simulated and measured experimentally (Figure **75**, Figure 79).

The SHG output power values are calculated assuming the phase matching bandwidth of the crystal covers the whole spectrum. SF11 prism pairs with 4 cm sides have been used. The beam spot at the entry to the first prism has been not wider than 5 mm, hence the insertion

of the beam into the apex of the first prism was not larger than 3 mm. Experimentally, the beam was steered as close to the apex of the first prism as possible without clipping it.

The pulse duration has been reduced greatly thanks to the prism compressor, but due to the uncompensated higher order chirps, a lot of the power has been smeared out in the tail of the pulse. Hence the improvement of the signal is not as prominent as it would be concluded with just half-width maximum alone, but is consistent with the SHG excited through integration over the whole of the pulse. The simulated SHG excited by the pulse is calculated as follows- the form of the pulse in time is integrated over its whole duration – intensity at each of the 1 fs long fragments is squared, and the total is summed up. This approach proved to work much better than just taking the peak power of the pulse or the pulse width. One can see that on the illustration Figure 71.

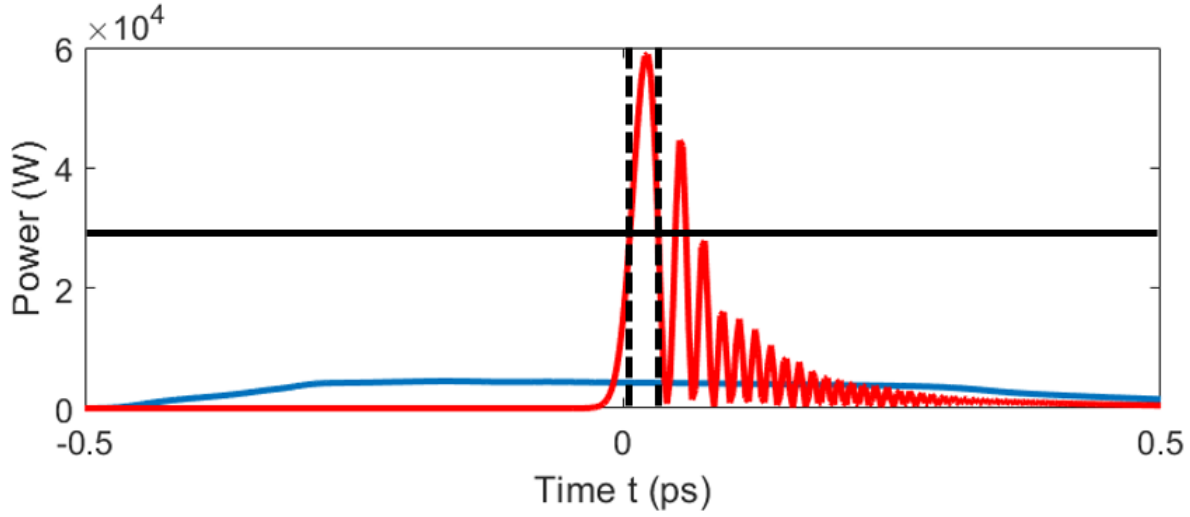

Figure 71 - Simulated pure quadratic compression of compressed (red, uncompressed in blue) broadband pulse - dashed line signifies Half Width of the pulse, visualising significant amount of power spread outside of that range, raising the need for integral SHG emission quantification. Simulation parameters – seed 800 nm, SC generated in 85 mm piece at 280 mW power.

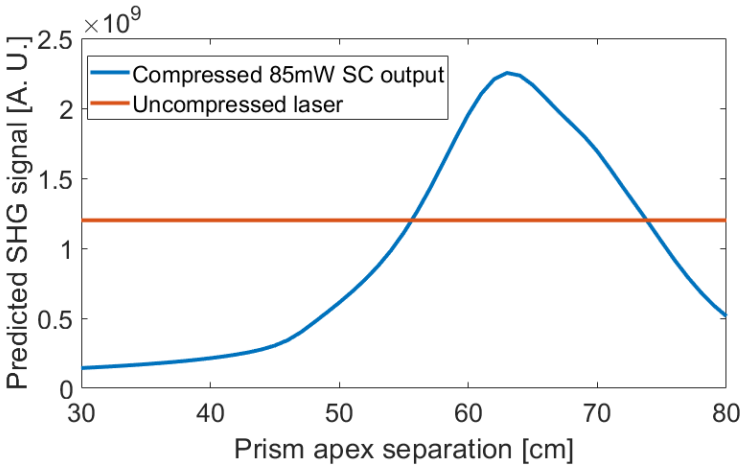

Figure 72 - Compression simulation for the 85 mW output from the 9 cm fibre quantified through predicted SHG emission from BaTiO crystal

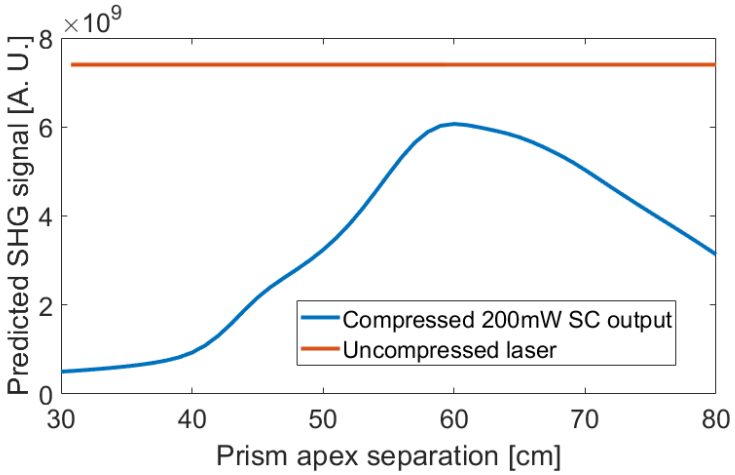

Figure 73 - Compression for the 200 mW output from the 9 cm fibre quantified through predicted SHG emission from BaTiO crystal. In spite of the compression, predicted SHG emission is lower than uncompressed MaiTai output.

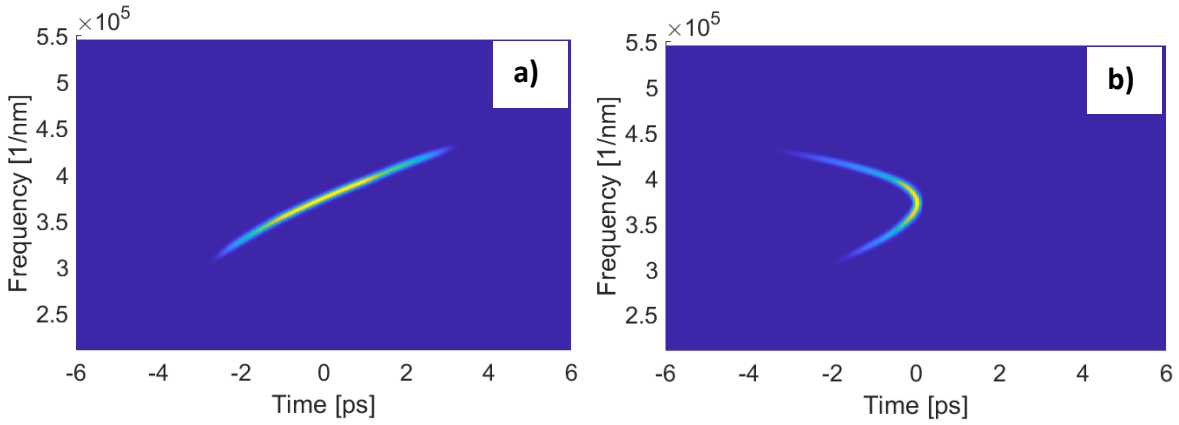

Figure 74 - 200 mW SC pulse at the focal point before (a) and after (b) compression

Here we see the time-frequency shape of the uncompressed and compressed pulse, as assessed through the simulation (see Figure 74). One can see the parabolic shape, caused by chirp of orders higher than second. Table below gives an indication of these chirp values characterising broadband, 280 mW pulse out of the fibre, after propagation through optical path, and at the prism compressor for 62 cm prism separation. One can see that although the second order chirp will be compensated fully, there is a big uncompensated third order phase distortion, exacerbated by the compressor itself. Values established computationally.

GDD	**2nd order [fs^2]**	**3rd order [fs^3]**	**4th order [fs^4]**	**5th order [fs^5]**
Material dispersion	3146	753	-64	49
Fibre output	818	379	-64	122
Compressor	-3937	-6236	-3136	-702
Total	27	-5104	-3264	-531

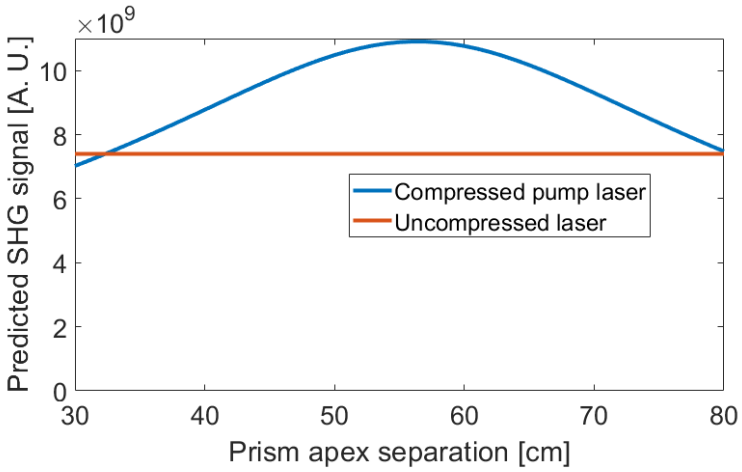

Figure 75 **- Compression simulation for the 800 nm Ti:Sapph pulse quantified through predicted SHG emission from BaTiO crystal**

Important thing to consider here is the influence of the uncertainty regarding the shapes of the spectral phase. The whole supercontinuum is being much more chirped when propagating undivided. When divided, the phase distortion is more linear for pump and Stokes separately, therefore the stretch in time is smaller as well.

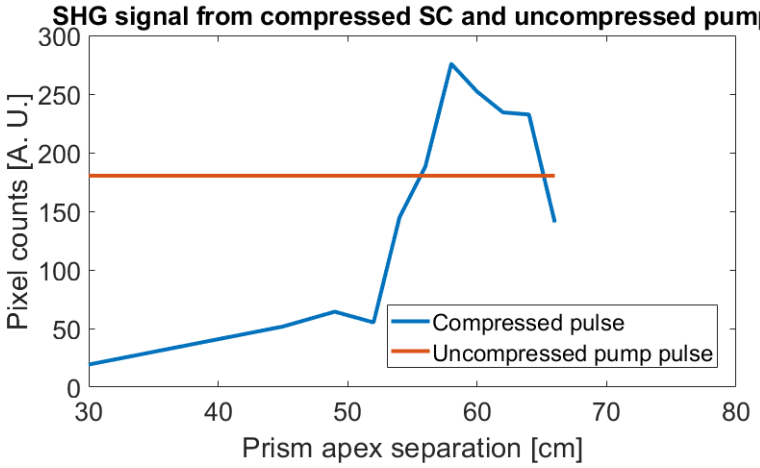

Figure 76 **– Compression experimental results for the 85 mW output from the 9 cm fibre quantified through registered strength of SHG emission from BaTiO crystal**

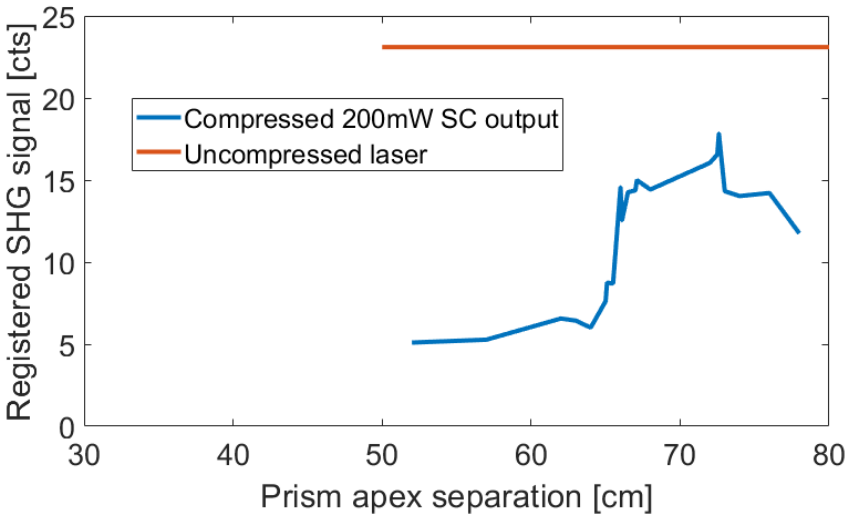

Figure 77 **- Compression experimental results for the 200 mW output from the 9 cm fibre quantified through registered strength of SHG emission from BaTiO crystal**

During acquisition, special care had to be taken to take into account the influence of broadband transmittivity and PMT sensitivity across wavelengths, which influences signal registered- the same peak power can give drastically different signal for 700 and for 800 nm (350 nm and 400 nm at the detection respectively).

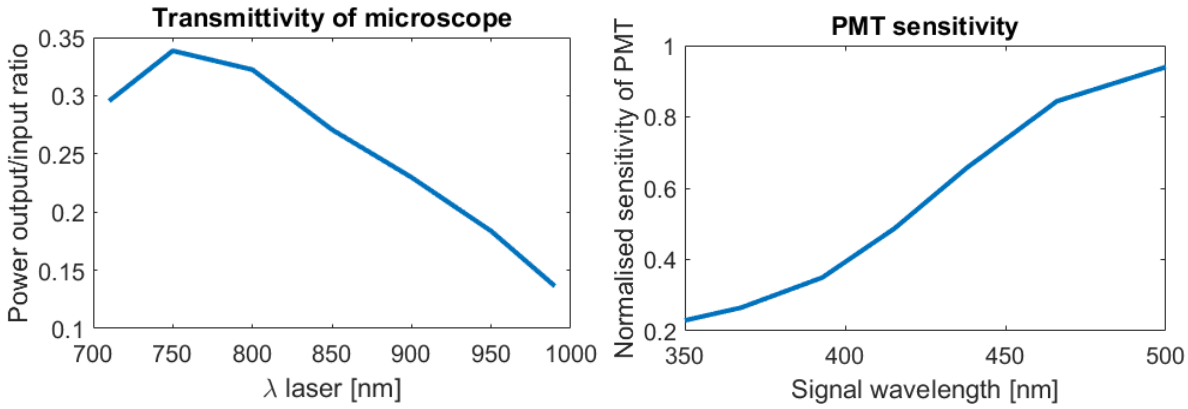

Figure 78 - Broadband characteristics of excitation (left) and SHG/SFG detection (right) system

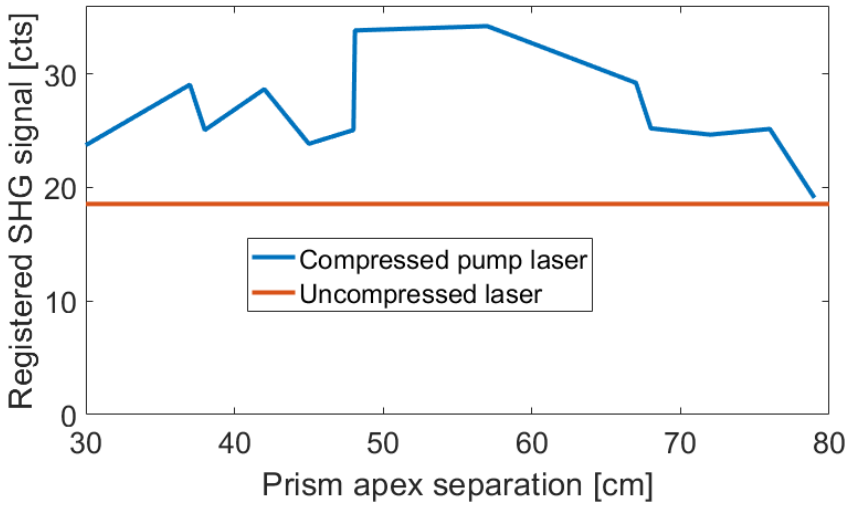

Figure 79 - Compression experimental results for the 800 nm Ti:Sa beam quantified through registered strength of SHG emission from BaTiO crystal

The SHG signal emission driven with the compressed supercontinuum/laser beam has been compared with the signal generated through the use of uncompressed 800 nm MaiTai laser, using the same beam diameter and polarisation. This way, a quantitative estimation of quality of compression can be made, as plotted on the abovementioned figures.

Moreover, a quantification of decrease of the signal coming from the SHG emission generated on a collagen-rich mouse tail sample has been attempted. Image has been registered for the different amounts of glass added on the path of the beam, for the same microscopy setup

with the same dispersive influence on the broadband pulse, without any compression. The results are being presented on Figure 80 .

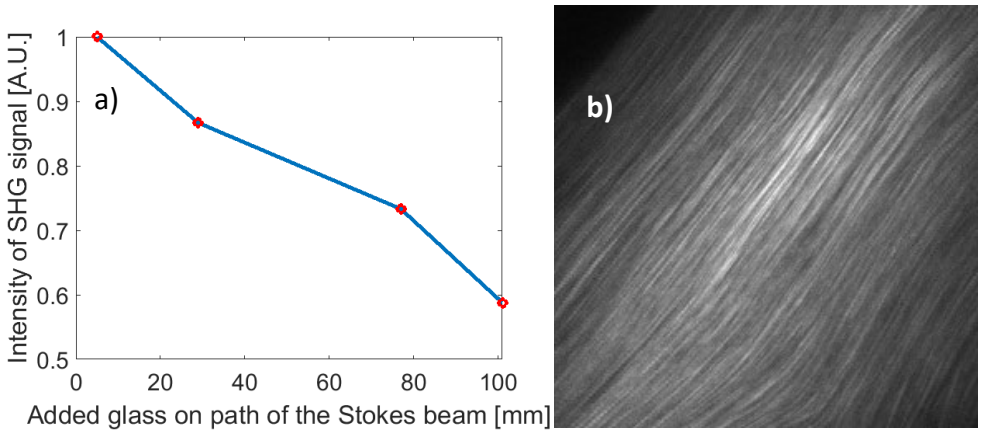

Figure 80 - Quantification of chirp influence on SHG signal (a) and the sample picture for the first data point (b)

5.3.5 Application of compressed SC

Because of the spectrally narrow acceptance bandwitdth of the 0.5 mm thick (ca. 25 nm) used crystal a time shape measured by SHG intensity autocorrelation could not give meaningful results for our broadband pulse.

The other possibility for difficulties arising while applying a compressed spectrum is clipping of the spectrum caused by using prisms too small for that purpose. The angular range of refracted light out of the first prism is very big which causes clipping of edge frequencies at the second prism**,** therefore the design was modified incorporating the 4 cm size, largest available on the market. It was barely sufficient for that purpose, so one would need to possibly consider custom-manufactured prisms. However, that would increase the cost of the setup considerably.

Provided only a moderate amount of power is lost, this disadvantage could be turned into an advantage, as this presents the possibility of spectral filtering out the edges of the spectrum, which eliminates the largest phase distortion.

5.4 Compression of user-selected spectral ranges within the SC

It has been suggested before, that for the purpose of multi-wavelength nonlinear imaging (including 5-color-iCARS), the division of the broadband laser pulse may be necessary in order to achieve high peak power [172] [40]. This is caused by the dispersive properties of the materials, causing nonlinear chirp in the broadband pulse during its propagation throughout the optics. As discussed in previous chapters, that change in dispersion can be partially compensated by insertion of chirp equalising blocks. However, this kind of tailoring is suitable for stretching the pulse appropriately. For applications like Second Harmonic Generation or Two Photon Fluorescence an opposite is needed- the phase distortion of the pulse at the focal point needs to be compensated and pre-compensated so that the peak power at the sample plane will be maximized. Because of the high-order chirp caused partly by the material dispersion, and partly by the compressor itself (already known to be detrimental) the compression of the pulse was far from the optimal transform-limited duration. However, one can get around it by compressing each of the pulses separately. Measurements have been conducted on Stokes alone and Pump and Stokes coinciding at the sample. The Second Harmonic from the pump alone could not been detected because of the properties of the filter, but the Sum Frequency between the two could easily be detected. Therefore, we have simultaneous emission of SHG and SFG from pump and Stokes interaction which was orders of magnitude higher than the emissions concurrent with the SF-CARS imaging. That shows the clear way of easily extending the capabilities of designed system- if one found interesting details in one of the modalities, it would be possible to switch quickly to higher-power pulses. One would make the CARS modality application impossible, but would increase the contrast in the resulting SHG and TPEF images greatly.

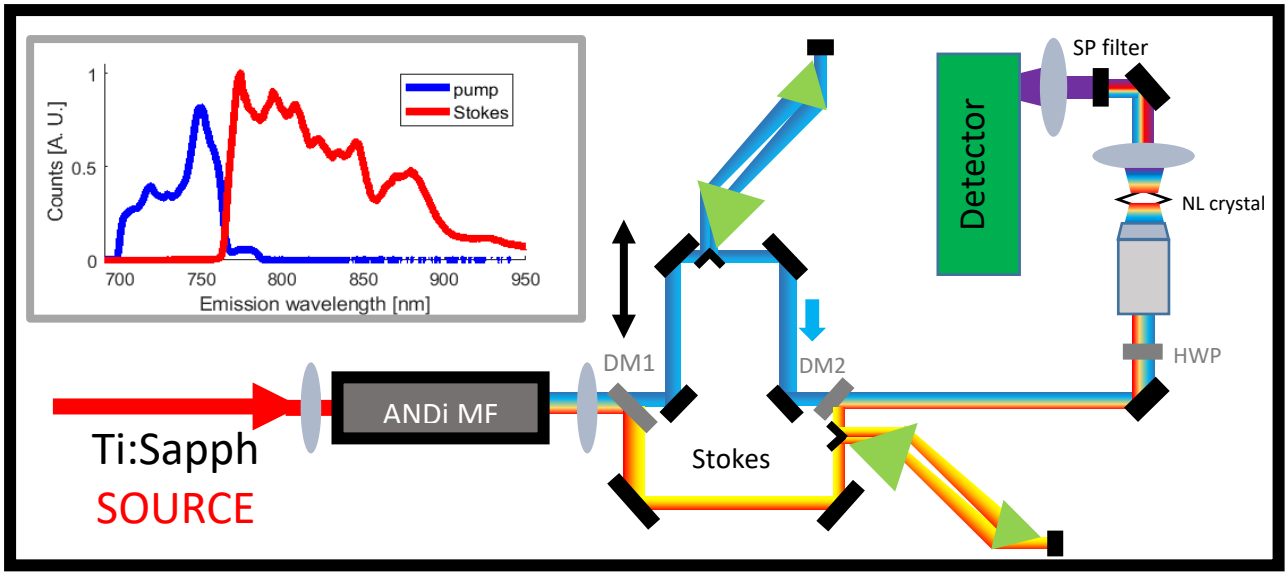

Figure 81 - multi-prism-pair compression of spectrally divided pulse

To that purpose, a setup was constructed, as presented on Figure 81.

For the Stokes beam compression, there has been an improvement noted. For prism separation of 57 cm and ca. 0.8 mW at the focal point, the intensity of SHG excited by Stokes was 6x higher than intensity of SHG excited by narrowband MaiTai 100 fs pulse at 800 nm (average number of counts of 260 vs 40), showing that considerable compression has been achieved. For pump, because of its narrowband character the improvement was not noted, however it can change should the spectral division be shifted towards the longer wavelengths, providing two pulses of comparable spectral breadth. Registered SHG images excited with both compressed Stokes and MaiTai 130 fs pulse are presented on Figure **82**.

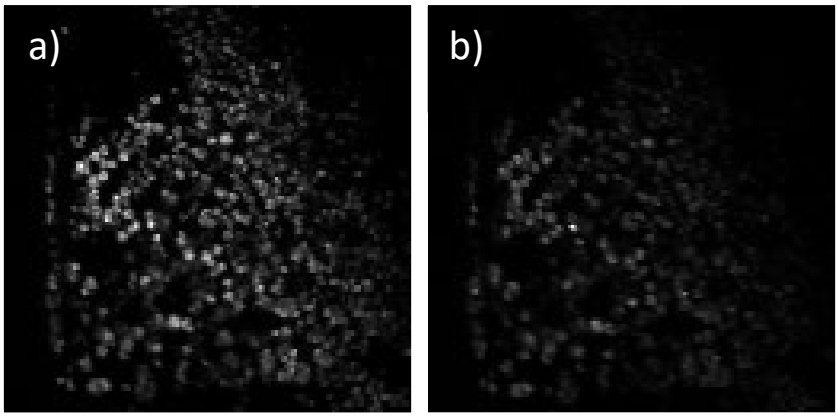

Figure 82 **- SHG emission registered on the BaTiO crystal for a) Compressed Stokes b) uncompressed MaiTai Ti:Sapph laser.**

5.5 Summary

Expanding on the application of SC in the supporting modality of TPEF, the SC has been used to excite the multi-photon fluorescence out of the two different labels. This presents additional possibility for this complementary modality – namely targeting two substances with very different absorption curves, so as to image differently labelled structures when using labels. However, the weak signal emitted from the sample while using this modality led us to consider possible enhancement in the form of compression. Two different compression setups have been constructed, and pulse compression has been investigated. For 1055 nm seeded SC, the pulse FMHW duration has been measured through intensity autocorrelation, and the SC has been applied in a TPEF imaging modality. For 800 nm seeded SC, the pulse duration has been indirectly measured through SHG emission from the sample at the focal point of the microscope, but no imaging has been done. The supercontinuum has been imperfectly compressed, failing to achieve predicted transform-limited pulse duration, mostly caused by uncompensated higher order chirp, showing clear disadvantage in comparison to SLM-based approaches, but in spite of that presents a clear potential for a low-cost extension to fibre-based SF-CARS imaging setup.

6. SUMMARY

Overall, the project applied the knowledge gathered by multiple physics groups working in the fields of nonlinear fibre optics and nonlinear laser microscopy/nonlinear bioimaging.

Firstly, existing sources suitable for nonlinear, label-free bioimaging have been analysed. Then, the need for an optimised supercontinuum source has been addressed by appropriately tailoring a microstructured fibre pumped by two different fs lasers for that purpose. The results of this investigation across the parameter space are presented in chapter 3. Chapter 4 presents application of the tailored source for biomedical multimodal imaging, which has been published in a peer-reviewed journal. The results show successful acquisition of CARS, SHG/SFG and TPEF signals from biological tissue. The final results chapter presents an extension to the project by using the broadband (and therefore, short transform-limited duration) characteristic of the pulse and de-chirp it using a simple prism compressor geometry. Therefore, a capability to target multiple fluorophores is presented as a way to increase capabilities of the setup. A clear step towards clinical application of the investigated techniques has been made.

7. FUTURE WORK POSSIBLE USING THE SYSTEM

7.1 1st goal– SRS imaging conducted using AOM modulation

The low inherent RIN noise of ANDi fibres (see Figure 83) is not above the noise levels for a typical SRS experiment [173]. The conducted measurements of RIN conducted in the scope of this project confirm that assumptions.

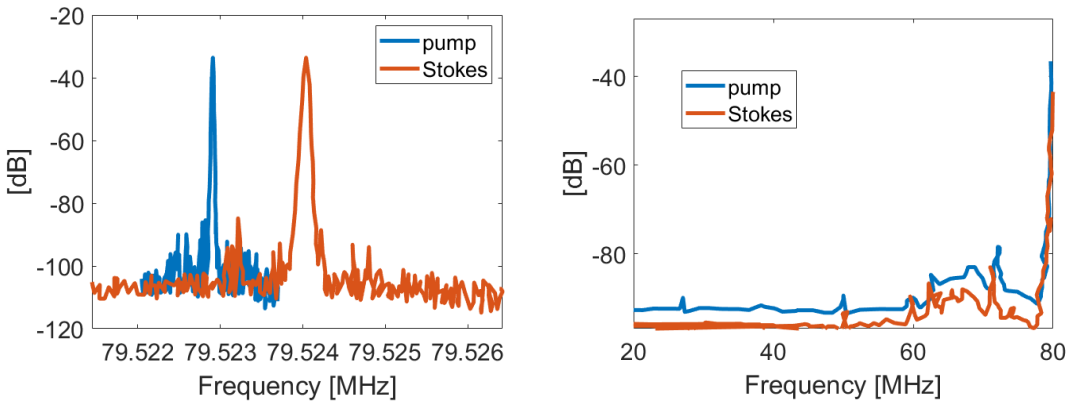

Figure 83 - RIN measurements of pump and Stokes after the SC division presenting low noise levels in comparison with central peak of laser frequency (70 dB difference between the peak and noise floor).

In order to achieve a narrowband pulse, to be applied in 3-color CARS setup, an AOTF can be used. Furthermore, if using this AOTF as modulator, and not only filter, we could introduce additional modulation for purpose of application in SRS.

7.2 2nd goal – Novel glass fibre- based SC generation for ps systems

As discussed in [174], chalcogenide glasses, already established in photonics applications [80] can be successfully used to develop highly nonlinear fibres. Up to now there has not been recorded supercontinuum generation in chalcogenide fibres with wavelength as short as 1 µm, but there exist already materials possible to construct such a fibre [175]. Possibilities of generating Supercontinuum with a ps pulsed laser have been investigated across the parameter space of the fibre. If that would be successful, this would be an important avenue to pursue in order to extend the capabilities of picosecond based pulsed laser system, currently used for CARS. Therefore, one would be able not only to convert existing fluorescence setup, but also existing CARS systems to SF-CARS capable setups.

The dispersion curve of both fibres (for NEG-1 from specification, for GLS glass from the bulk material refractive index characterisation) has been presented on the Figure 84.

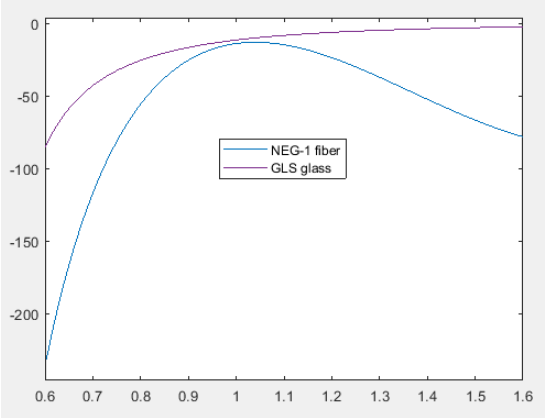

Figure 84 - Dispersion for ANDi and novel glass fibre

We conducted predicted broadening simulations with following parameters- 2 ps Gaussian pulse, 1032 nm pulse and 80 MHz repetition rate (consistent with specification of APE system at the IfLS). The parameter space has been explored to establish minimum requirement for efficient broadening – parameters investigated have been coupled power (Figure 85), fibre length (Figure 86) and core size (Figure 87), which are showed below.

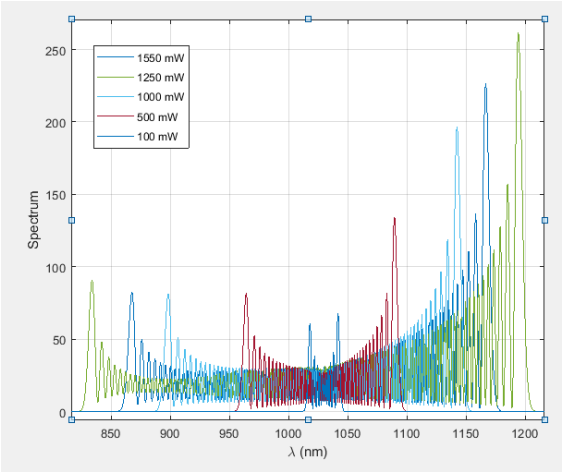

Figure 85 - For 20 µm core diameter, 0.3 dB/cm loss and 20 cm length

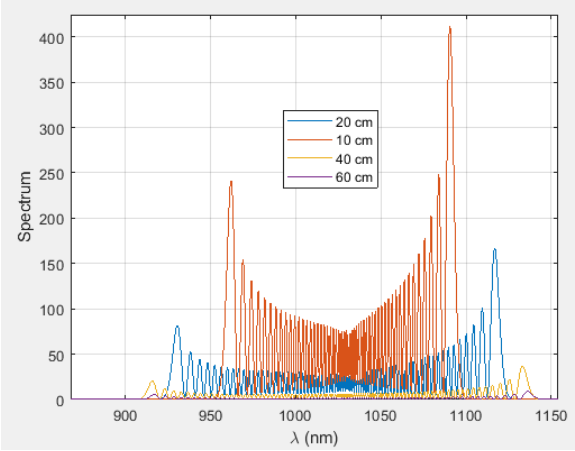

Figure 86 - For 750 mW, 20 µm core diameter and 0.3 dB/cm loss

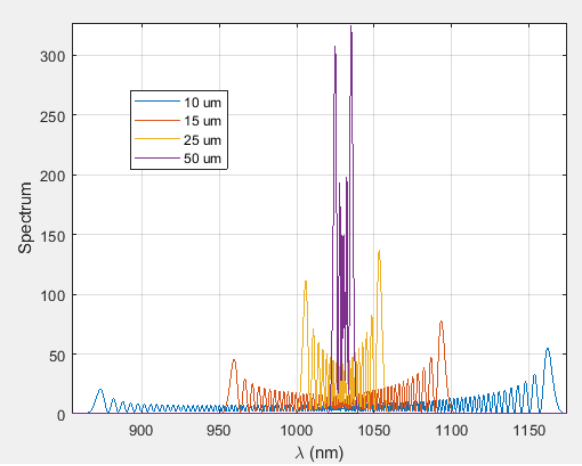

Figure 87 - For 2000 mW and 0.3 dB/cm loss

On basis of this exploration, we established that the low loss is essential- even with the small core, large loss will successfully attenuate the output. If both low loss and small core (at least 20 µm) can be achieved and light can be coupled, then simulations are valid, and an attempt to couple power and spectrally investigate the output can be made.

7.3 3rd goal – Further development of SC compression – possibly introducing multi-colour CARS approach

As already suggested in [40], division of a pulse into spectral fragments improves the possibility of compression, as we avoid higher-order dispersion effects.

A serious disadvantage of 3-color CARS as compared with 2-color CARS is, that the 2-color excitation and probing still takes place, therefore the 3-color emission, while using the NRB-reducing delayed probing effect, will still be much lower than 2-color.

However, if one should need to implement 3-color CARS, one would be able to use the AOTF tunable filter to tailor MaiTai emission so that spectral breadth will be <1 nm. Naturally, that would reject a lot of the power of the laser. One would also probably need to implement transmission modality, as per weakness of the signal.

7.4 4th goal – Integration of the source in an endoscopy setup

Using development of hollow-core fibre probe, one can try and implement the developed source in an all-fibre system. It was first used for high power laser delivery for biomedical purposes in 2004 [176]. Hollow core fibres have also been demonstrated to compress the pulses, opening doors to this application [177]. Non-linear microscopy has been also successfully conducted in such fibreized setup [178].

One of such fibres, available to us, is Nested Antiresonant Nodeless Hollow Core fibre [80]. This hollow-core fibre has demonstrated optimal transmission properties, as presented on Figure 88. This shows that it can be used for successful guidance of both pump and Stokes of pulse generated by our setup. Hollow core geometry ensures highly preserved temporal shape of the pulse, which is of big importance for all the relevant imaging modalities.

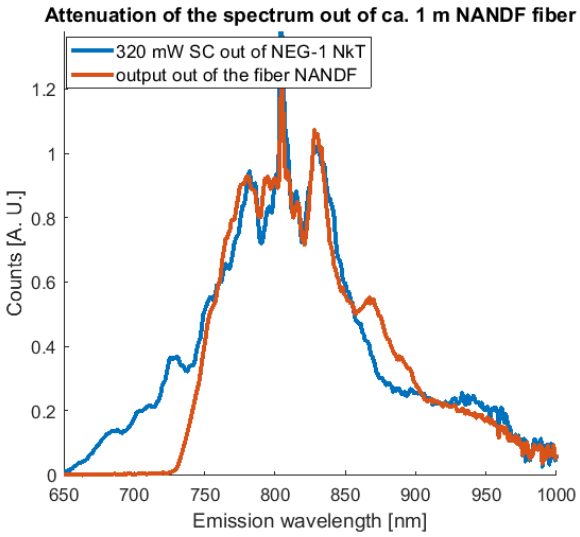

Figure 88 - Transmission of the NANDF fibre as shown by comparison of input and output spectrum

This opens doors to potential application of our developed source for an all-fibre imaging system- SC source in order to generate laser pulse, hollow core fibre as a guiding medium (adjustable length for one of them would fulfil the function of a delay line), and a piezoelectric based scanning head could form a robust imaging system, competitive to currently used commercial applications. An important outlook into the problem of splicing PCF and step-index fibre has been discussed in [179].

APPENDIX- COMPRESSION CODE (WRITTEN BY CANDIDATE)

```
%Insertion of the beam in 1st and 2nd prism (P1 and Pins) in micrometers
along the side, going from the apex
clear all
close all
P1=2000;
Pins=2000;
matlength=0.*10.^4; %um
lambda_central=0.8; %um %1.109 originally
ce=2.9979*1e14; %speed of light in micrometers per second

alfa=60; %apex angle of the prism
alfa_prim=90-(alfa/2); %base angle of the prism, under assumption it has a
middle axis of symmetry
Lp=30;
separation=Lp*10000; %prism separation along the path of 1055 nm beam in um

P1prim=P1*sind(alfa)/(sind(alfa_prim)); %projection of path P2 in the first
prism upon the base
angle1=56.045; %angle for 1.055 um
%angle1=55.745 %angle for 800 nm for 200 um insertion

wangular_central=2*3.14*ce/lambda_central;
size=40000; %size of the longer side of the prism


%From Schott glass catalogue for SF11

B1=1.73759695;
B2=0.313747346;
B3=1.898781010;
C1=0.01318870700;
C2=0.0623068142;
C3=155.2362900;



start=0.600; %for wavelength

stop=1.00;

space=0.0001;


lam=(start:space:stop); %vector of wavelengths in the vacuum
noel=length(lam); %number of elements of lam vector, containing different
wavelenths separated by space
%else
  %  wangular=(start2:space2:stop2)*10^12;%vector of angular frequencies
separated by space2
  %  noel=length(wangular);

%calculation of group refractive indices for each of the frequencies
```

```
zet=1;

%preallocations
en=zeros(1,noel);
lambda_from_angular=zeros(1,noel);
angarr2=zeros(1,noel);
angarr3=zeros(1,noel);
angarr4=zeros(1,noel);
angarr5=zeros(1,noel);
angarr6=zeros(1,noel);
angarr7=zeros(1,noel);
angarr8=zeros(1,noel);
Pb_arr=zeros(1,noel);
side_small_arr=zeros(1,noel);
Parr=zeros(4,noel)';
a1_arr=zeros(1,noel);
a2_arr=zeros(1,noel);
a3_arr=zeros(1,noel);
eng2=zeros(1,noel);


i=1;

lambda_1055=lambda_central;
n_1055= sqrt(((B1*lambda_1055^2)/(lambda_1055^2-C1))+
((B2*lambda_1055^2)/(lambda_1055^2-C2))+((B3*lambda_1055^2)/(lambda_1055^2-
C3)) +1);
angle2_1055=rad2deg(asin(sind(angle1)/n_1055));
angle3_1055=alfa-angle2_1055;
angle4_1055=rad2deg(asin((sind(angle3_1055))*n_1055));
sep_orto=separation*cosd(angle4_1055)/(cosd(alfa/2));
displ_1055=(-1)*sep_orto*cosd(alfa_prim+angle4_1055)/(cosd(angle4_1055));
outs_1055=P1prim*cosd(alfa_prim+angle2_1055)/(cosd(angle3_1055));
displ_apex=Pins+displ_1055+outs_1055;



%For each wavelength/frequency n is calculated, and then calculation of
angles follow, and for every angle the data is saved in an array for each
frequency/wavelength

%Angle1- incoming angle onto side of 1st prism, angle2- angle of the beam
in the 1st prism, angle3 - incoming angle onto 2nd side of 1st prism,
angle4- angle of the beam outgoing from the 1st prism, angle5 - angle
incoming onto 1st side of 2nd prism, angle6- angle of the beam out of 1st
side of 2nd prism, angle7- incoming angle onto 2nd side of 2nd prism,
angle8- outgoing beam angle with the 2nd side of 2nd prism, omicron-
helpful angle between the path of the beam and the line parallel to bases
of prisms.
while i<(noel+1)


lambda=lam(i);

%temporary central wavelentgth in um
```

```
n= sqrt(((B1*lambda^2)/(lambda^2-C1))+ ((B2*lambda^2)/(lambda^2-
C2))+((B3*lambda^2)/(lambda^2-C3)) +1);
en(i)=n;
angle2=rad2deg(asin(sind(angle1)/n));
angarr2(i)=angle2;
angle3=alfa-angle2;
angarr3(i)=angle3;
angle4=rad2deg(asin((sind(angle3))*n));
angarr4(i)=angle4;

angle5=angle4;
angarr5(i)=angle5;
angle6=rad2deg(asin(sind(angle5)/n));
angarr6(i)=angle6;
angle7=alfa-angle6;
angarr7(i)=angle7;
angle8=rad2deg(asin((sind(angle7))*n));
angarr8(i)=angle8;

P2=P1prim*cosd(alfa/2)/cosd(angle3); %path of beam in the first prism
outs=P1prim*cosd(alfa_prim+angle2)/cosd(angle3);
P3=sep_orto*cosd(alfa/2)/cosd(angle4); %path between the prisms
displ=(-1)*sep_orto*cosd(alfa_prim+angle4)/cosd(angle4);
Pb=displ_apex-displ-outs; %insertion of the beam from apex of 2nd prism

% if (Pb<0 || Pb>size) %loop to determine if spectrum fits inside the prism
- between the apex and the end
%     'stop';
%     return
% end

Pb_prim=Pb*sind(alfa)/sind(alfa_prim); %projection of path P5 onto the line
parallel to base of prism
Pb_arr(i)=Pb;
P5=Pb_prim*cosd(alfa/2)/cosd(angle7); %path of the beam in the second prism
shift=Pb_prim*cosd(alfa_prim+angle6)/cosd(angle7); %shift of the beam on
the outgoing facet in respect to its position at incoming facet

side_small=size-(Pb+shift);

side_small_arr(i)=side_small;

%condition for stopping- spectrum does not fit inside the prisms

% if (side_small<0 || side_small>size) %loop to determine if spectrum fits
inside the prism - between the apex and the end
%     'stop';
%     return
% end



Proof=side_small*sind(angle8);
```

```
angle=[angle1 angle2 angle3 angle4 angle5 angle6 angle7 angle8];
P=[P2 P3 P5 Proof];
Parr(i,:)=P;

Popt=2*[P2*n P3 P5*n Proof]; %optical path length considering phase
refractive index
%a1,a2,a3- analytical coefficients for possible comparisons
a1 = -((2*B1*lambda)/(- lambda^2 + C1) + (2*B2*lambda)/(- lambda^2 + C2) +
(2*B3*lambda)/(- lambda^2 + C3) + (2*B1*lambda^3)/(C1 - lambda^2)^2 +
(2*B2*lambda^3)/(C2 - lambda^2)^2 + (2*B3*lambda^3)/(C3 -
lambda^2)^2)/(2*(1 - (B2*lambda^2)/(C2 - lambda^2) - (B3*lambda^2)/(C3 -
lambda^2) - (B1*lambda^2)/(C1 - lambda^2))^(1/2)) ;
a2 = - ((2*B1*lambda)/(- lambda^2 + C1) + (2*B2*lambda)/(- lambda^2 + C2) +
(2*B3*lambda)/(- lambda^2 + C3) + (2*B1*lambda^3)/(C1 - lambda^2)^2 +
(2*B2*lambda^3)/(C2 - lambda^2)^2 + (2*B3*lambda^3)/(C3 -
lambda^2)^2)^2/(4*(1 - (B2*lambda^2)/(C2 - lambda^2) - (B3*lambda^2)/(C3 -
lambda^2) - (B1*lambda^2)/(C1 - lambda^2))^(3/2)) - ((2*B1)/(- lambda^2 +
C1) + (2*B2)/(- lambda^2 + C2) + (2*B3)/(- lambda^2 + C3) +
(10*B1*lambda^2)/(C1 - lambda^2)^2 + (10*B2*lambda^2)/(C2 - lambda^2)^2 +
(8*B1*lambda^4)/(C1 - lambda^2)^3 + (10*B3*lambda^2)/(C3 - lambda^2)^2 +
(8*B2*lambda^4)/(C2 - lambda^2)^3 + (8*B3*lambda^4)/(C3 -
lambda^2)^3)/(2*(1 - (B2*lambda^2)/(C2 - lambda^2) - (B3*lambda^2)/(C3 -
lambda^2) - (B1*lambda^2)/(C1 - lambda^2))^(1/2));
a3 = - (3*((2*B1*lambda)/(- lambda^2 + C1) + (2*B2*lambda)/(- lambda^2 +
C2) + (2*B3*lambda)/(- lambda^2 + C3) + (2*B1*lambda^3)/(C1 - lambda^2)^2 +
(2*B2*lambda^3)/(C2 - lambda^2)^2 + (2*B3*lambda^3)/(C3 -
lambda^2)^2)^3)/(8*(1 - (B2*lambda^2)/(C2 - lambda^2) - (B3*lambda^2)/(C3 -
lambda^2) - (B1*lambda^2)/(C1 - lambda^2))^(5/2)) - ((24*B1*lambda)/(C1 -
lambda^2)^2 + (24*B2*lambda)/(C2 - lambda^2)^2 + (24*B3*lambda)/(C3 -
lambda^2)^2 + (72*B1*lambda^3)/(C1 - lambda^2)^3 + (72*B2*lambda^3)/(C2 -
lambda^2)^3 + (48*B1*lambda^5)/(C1 - lambda^2)^4 + (72*B3*lambda^3)/(C3 -
lambda^2)^3 + (48*B2*lambda^5)/(C2 - lambda^2)^4 + (48*B3*lambda^5)/(C3 -
lambda^2)^4)/(2*(1 - (B2*lambda^2)/(C2 - lambda^2) - (B3*lambda^2)/(C3 -
lambda^2) - (B1*lambda^2)/(C1 - lambda^2))^(1/2)) - (3*((2*B1*lambda)/(-
lambda^2 + C1) + (2*B2*lambda)/(- lambda^2 + C2) + (2*B3*lambda)/(-
lambda^2 + C3) + (2*B1*lambda^3)/(C1 - lambda^2)^2 + (2*B2*lambda^3)/(C2 -
lambda^2)^2 + (2*B3*lambda^3)/(C3 - lambda^2)^2)*((2*B1)/(- lambda^2 + C1)
+ (2*B2)/(- lambda^2 + C2) + (2*B3)/(- lambda^2 + C3) +
(10*B1*lambda^2)/(C1 - lambda^2)^2 + (10*B2*lambda^2)/(C2 - lambda^2)^2 +
(8*B1*lambda^4)/(C1 - lambda^2)^3 + (10*B3*lambda^2)/(C3 - lambda^2)^2 +
(8*B2*lambda^4)/(C2 - lambda^2)^3 + (8*B3*lambda^4)/(C3 -
lambda^2)^3))/(4*(1 - (B2*lambda^2)/(C2 - lambda^2) - (B3*lambda^2)/(C3 -
lambda^2) - (B1*lambda^2)/(C1 - lambda^2))^(3/2));
ng=n/(1+(lambda/n)*a1); %for low dispersion
a1_arr(i)=a1;
a2_arr(i)=a2;
a3_arr(i)=a3;
eng2(i)=ng;



i=i+1;
end
```

```
Parr2=2.*Parr; %two times Path, because of roundtrip
Parr2=Parr; %one time as no retroreflector in the new setup
Path_physical=Parr2(:,1)+Parr2(:,2)+Parr2(:,3)+Parr2(:,4);
Path_air=Parr2(:,2)+Parr2(:,4);
Path_glass=Parr2(:,1)+Parr2(:,3);


    %calculation according to Fork and Gordon formula for dispersion, for
    %comparison

Path_total=Path_air(1:end)+(Path_glass(1:end).*(en'));
TOF=Path_total./ce;
TOF_diff=diff(TOF);

wangular=2*pi*ce./lam;
wangular_diff=(2*pi*ce./lam)-(2*pi*ce/lambda_central);


phase=Path_total'.*2.*3.14./lam;
phase_mat=matlength*en.*2.*3.14./lam;
phase_diff=phase_mat+phase;
Y5=polyfit(wangular_diff,phase,5);
Y4=polyfit(wangular_diff,phase_diff,5);
Y3=polyfit(wangular_diff,phase_mat,5);
%saving the coefficients to a file for later retrieval
s_date='31_03_2019_';
s_lambda=num2str(lambda_central*1e3);
s_base='_nm_Wavelength_for_fitting_CalculatedPolynomial_material_prism_sep'
;
s_end='.txt';
name=strcat(s_date,s_lambda,s_base,num2str(Lp),'angle',num2str(angle1),s_en
d);
fileID=fopen(name,'w')
Yw=Y5; %polynomial to writing to file
Yw(end-2)=Yw(end-2)*1e30;
Yw(end-3)=Yw(end-3)*1e45;
Yw(end-4)=Yw(end-4)*1e60;
Yw(end-5)=Yw(end-5)*1e75;
fprintf(fileID,'%6.2f %6.2f %6.2f %6.2f',Yw(end-5:end-2))


Y2=polyfit(wangular_diff,phase,5);
Y2(end-1)=0;
Y2(end)=0;
Y3(end-1)=0;
Y3(end)=0;
Y4(end-1)=0;
Y4(end)=0;
Ygrek2=polyval(Y2,wangular_diff);
Ygrek3=polyval(Y3,wangular_diff);
Ygrek4=polyval(Y4,wangular_diff);


P_diff=diff(Path_total);
P_diff2=diff(P_diff);
```

```
P_diff3=diff(P_diff2);
P_diff2_lam=P_diff2/(space*space);
P_diff3_lam=P_diff3/(space*space*space);
FITTED=polyfit(lam(4:end)',P_diff3_lam,5);
FITTED_F=polyval(FITTED,lam);
beta3_formula=((-
3).*(10^45).*((lam(3:end)').^4).*P_diff2_lam(1:end)./(4*pi*pi*ce*ce*ce))+((
-1).*(10^45).*((lam(3:end)').^5).*FITTED_F(3:end)'./(4*pi*pi*ce*ce*ce));
%chirp in fs3
P_diff2_formula=(((4.*(a2_arr+(2*en-(en.^(-3))).*(a1_arr.^2))).*Pins)-
(8.*a1_arr.*a1_arr.*separation));
P_diff3_formula=(4.*a3_arr.*Pins)-(24.*a1_arr.*a2_arr.*separation);
beta3_formula2=((-
3).*(10^45).*((lam(1:end)).^4).*P_diff2_formula(1:end)./(4*pi*pi*ce*ce*ce))
+((-
1).*(10^45).*((lam(1:end)).^5).*P_diff3_formula(1:end)./(4*pi*pi*ce*ce*ce))
;
%Calculation on basis of formula in 1984 Fork Gordon paper
Dispersion=(lam(3:end)').*P_diff2./(ce.*Path_physical(3:end).*space.*space)
;
GVD=Dispersion.*(lam(3:end)').*(lam(3:end)')/(2*pi*ce); %GVD in s2/m- there
should be (-) sign
beta2=(10^30)*GVD.*Path_physical(3:end); %GDD in fs2
%beta calculation on basis on basis of beta2 formula in Fork & Shank paper

beta2_formula=(10^30)*((lam(3:end)').^3).*P_diff2_lam./(2*pi*ce*ce); %chirp
in fs2
beta2_formula2=(10^30)*((lam(1:end)).^3).*P_diff2_formula./(2*pi*ce*ce);

n_diff=diff(en);
n_diff2=diff(n_diff);
a1_new=n_diff/space ;%analytical formulas give results same as the
numerical
a2_new=n_diff2/(space*space);

Y2_vec=ones(1,noel);
Y2_vec=Y2_vec.*Y2(end-2)*2*10^30;
Y3_vec=ones(1,noel);
Y3_vec=Y3_vec.*Y2(end-3)*6*10^45;

figure(500)
plot(lam(3:end)',beta2_formula)
hold on
plot(lam(1:end)',beta2_formula2)
plot(lam',Y2_vec);
title('Quadratic phase distortion d^2 phase / dw^2')
legend('From numerical path derivative calculations','From Fork&Shank path
calculations','Extracted from phase change');
ylabel('quadratic numeric vs formula vs retrieved from phase [fs2]');
s12='\quadvs';
%s13=strcat(s11,s12);
%print(s13,'-dpng')


figure(999)
plot(lam(3:end)',beta3_formula)
hold on
```

```
plot(lam(1:end)',beta3_formula2)
plot(lam',Y3_vec);
title('Cubic phase distortion d^3 phase / dw^3')
legend('From numerical path derivative calculations','From Fork&Shank path
calculations','Extracted from phase change');
ylabel('cubic numeric vs formula vs retrieved from phase [fs3]');
s12='\cub3vs';
%s13=strcat(s11,s12);
%print(s13,'-dpng')
mGDD=(a2_arr.*matlength.*(lam.^3).*10.^30)./(2.*pi.*ce.*ce); %fs2/um
mTODD=matlength*(((-
3).*(10^45).*((lam(1:end)).^4).*a2_arr(1:end)./(4*pi*pi*ce*ce*ce))+((-
1).*(10^45).*((lam(1:end)).^5).*a3_arr(1:end)./(4*pi*pi*ce*ce*ce)));
% Dispersion=-2*3.14*ce.*GVD./(lam.*lam); %Dispersion in fs2/(um*s*mm)
% Dispersion2=Dispersion*10^18; %Dispersion in ps/(nm*km)


figure(9991)
wangular_diff_to_lambda=2*pi*ce ./ (wangular_diff +
2*pi*ce/lambda_central);
plot(wangular_diff_to_lambda,Ygrek2);
figure(9992)
plot(wangular_diff,Ygrek2);
set(9992,'Name','Phase from compressor')
figure(9993)
set(9993,'Name','Phase after compensation')
plot(wangular_diff,Ygrek4);
figure(9998)
set(9998,'Name','Phase from material + from compressor')
plot(wangular_diff,Ygrek3);
hold on
plot(wangular_diff,(-1)*Ygrek2);

chirpp=2*Yw(end-2)
```

BIBLIOGRAPHY

[1] X. Chen and et al., “Second harmonic generation microscopy for quantitative analysis of collagen fibrillar structure,” *Nature protocols,* vol. 7, no. 4, pp. 654-669, 2012.

[2] “Histology Procedure Manuals,” [Online]. Available: http://library.med.utah.edu/WebPath/HISTHTML/MANUALS/MANUALS.html. [Accessed 15 06 2016].

[3] “An Introduction to Routine and Special Staining,” [Online]. Available: http://library.med.utah.edu/WebPath/HISTHTML/MANUALS/MANUALS.html. [Accessed 15 06 2016].

[4] M. B. Fenn and et al., “Raman Spectroscopy for Clinical Oncology,” *Advances in Optical Technologies,* 2011.

[5] T. Gottschal and et al., “Fiber-based light sources for biomedical applications of coherent anti-Stokes Raman scattering microscopy,” *Laser & Photonics Reviews,* vol. 9, no. 5, pp. 435-451, 2015.

[6] W. R. Zipfel et al., “Nonlinear magic: multiphoton microscopy in the biosciences,” *Nature biotechnology,* vol. 21, no. 11, pp. 1369-1377, 2003.

[7] C. Kleusch et al, “Fluorescent Lipids: Functional Parts of Fusogenic Liposomes and Tools for Cell Membrane Labeling and Visualization,” *Molecules,* vol. 17, no. 1, pp. 1055-1073, 2012.

[8] R. Alford et al., “Toxicity of Organic Fluorophores Used in Molecular Imaging: Literature Review,” *Molecular Imaging,* vol. 8, no. 6, 2009.

[9] K. Carlsson et al., “Three-dimensional microscopy using a confocal laser scanning microscope,” *Optics Letters,* vol. 10, no. 2, pp. 53-55, 1985.

[10] J. E. Iglesias and et al., “A computational atlas of the hippocampal formation using ex vivo, ultra-high resolution MRI: Application to adaptive segmentation of in vivo MRI,” *NeuroImage,* vol. 115, pp. 117-137, 2015.

[11] M. L. Gabriele et al., “Optical Coherence Tomography: History, Current Status, and Laboratory Work,” *Investigative Ophthalmology & Visual Science,* vol. 52, no. 5, pp. 2425-2436, 2011.

[12] M. S. Grinolds et al., “Subnanometre resolution in three-dimensional magnetic resonance imaging of individual dark spins,” *Nature nanotechnology,* vol. 9, no. 4, pp. 279-284, 2014.

[13] P. Lasch et al., Biomedical Vibrational Spectroscopy, John Wiley & Sons, 2008.

[14] R. Tsenkova, “Aquaphotomics: Dynamic Spectroscopy of Aqueous and Biological Systems Describes Peculiarities of Water,” *Journal of Near Infrared Spectroscopy,* vol. 17, no. 6, pp. 303-313, 2009.

[15] D. I. Ellis and et al., “Metabolic fingerprinting in disease diagnosis: biomedical applications of infrared and Raman spectroscopy,” *Analyst,* vol. 131, p. 875–885, 2006.

[16] H. Haken et al., “Raman effect,” in *Molecular Physics and Elements of Quantum Chemistry*, Berlin, Springer, 1994, pp. 199-200.

[17] X. S. Xie et al., “Theory of Coherent Raman Scattering,” in *Coherent Raman Scattering Microscopy*, Taylor & Francis Group, LLC, 2013, pp. 3-42.

[18] “Raman scattering,” [Online]. Available: https://www.doitpoms.ac.uk/tlplib/raman/raman_scattering.php. [Accessed 20 05 2017].

[19] G. Petrov et al., “Comparison of coherent and spontaneous Raman,” *Proceedings of the National Academy of Sciences,* vol. 104, no. 19, pp. 7776-7779, 2007.

[20] C. H. Camp Jr et al., “Chemically sensitive bioimaging with coherent Raman scattering,” *Nature Photonics,* vol. 9, p. 295, 2015.

[21] P. D. Maker et al., “Study of Optical Effects Due to an Induced Polarisation Third Order in the Electruc Field Strength,” *Physical Review,* vol. 3A, no. 137, pp. A801-A818, 1969.

[22] M. D. Duncan et al., “Scanning coherent anti-Stokes Raman microscope,” *Optics Letters,* vol. 8, no. 7, pp. 350-352, 1982.

[23] A. Zumbusch et al., “Three-Dimensional Vibrational Imaging by Coherent Anti-Stokes Raman Scattering,” *Physical Review Letters,* vol. 82, no. 20, pp. 4142-4145, 1999.

[24] M. Müller et al., “Coherent anti-Stokes Raman Scattering Microscopy,” *ChemPhysChem,* vol. 8, no. 15, pp. 2156-2170, 2007.

[25] C. Evans and et al., “Coherent Anti-Stokes Raman Scattering Microscopy: Chemical Imaging for Biology and Medicine,” *Annual Review of Analytical Chemistry,* vol. 1, no. 1, pp. 883-909, 2008.

[26] E. Bélanger et al., “In vivo evaluation of demyelination and remyelination in a nerve crush injury model,” *Biomedical Optics Express,* vol. 2, no. 9, pp. 2698-2708, 2011.

[27] T. Le et al., “Coherent anti-Stokes Raman scattering imaging of lipids in cancer metastasis,” *BMC Cancer,* vol. 9, pp. 42-42, 2009.

[28] S. Konorov et al., “In Situ Analysis of Living Embryonic Stem Cells by Coherent Anti-Stokes Raman Microscopy,” *Analytical Chemistry,* vol. 79, no. 18, pp. 7221-7225, 2007.

[29] J. Smus et al., “Tracking adipogenic differentiation of skeletal stem cells by label-free chemically selective imaging,” *Chemical Science,* vol. 6, pp. 7089-7096, 2015.

[30] C. Evans and et al., “Chemical imaging of tissue in vivo with video-rate coherent anti-Stokes Raman scattering microscopy,” *Proceedings of the National Academy of Sciences of the United States of America,* vol. 102, no. 46, p. 16807, 2005.

[31] Y. Jung et al., “Longitudinal, 3D In Vivo Imaging of Sebaceous Glands by Coherent Anti-Stokes Raman Scattering Microscopy: Normal Function and Response to Cryotherapy,” *Journal of Investigative Dermatology,* vol. 135, no. 1, pp. 39-44, 2015.

[32] N. J. Turro, Modern molecular photochemistry, University Science Books, 1991.

[33] A. M. Weiner, “Ultrafast Nonlinear Optics: Second Order,” in *Ultrafast Optics*, John Wiley & Sons, INC., 2009, pp. 198-257.

[34] C. Thiel, “Four-Wave Mixing and its Applications,” December 2000. [Online]. Available: https://www.researchgate.net/publication/241258853_Four-Wave_Mixing_and_its_Applications. [Accessed 22 March 2020].

[35] H. Tu et al., “Coherent anti-Stokes Raman scattering microscopy: overcoming technical barriers for clinical translation,” *Journal of Biophotonics,* vol. 7, no. 1-2, pp. 9-22, 2014.

[36] D. P. S. G. d. Costa, “3.3.1. CARS Signal Generation in Forward- and Epi-Direction,” in *Hyperspectral Coherent Anti-Stokes Raman Scattering (CARS) Imaging, diploma thesis*, Stuttgart, Universitaet Stuttgart, 2019, pp. 19-22.

[37] J.-X. Cheng and et al., “Coherent anti-Stokes Raman scattering microscopy: instrumentation, theory and applications,” *J. Phys. Chem. B,* vol. 108, no. 3, pp. 827-840, 2004.

[38] H. Lotem et al., “Interference between Raman resonances in four-wave difference mixing,” *Physical Review A,* vol. 14, no. 5, p. 1748, 1976.

[39] C. W. Freudiger et al., “Label-Free Biomedical Imaging with High Sensitivity by Stimulated Raman Scattering Microscopy,” *Science,* vol. 322, no. 5909, pp. 1857-1861, 2008.

[40] T. Monfort, “Non linear photonics: developments & applications in biomedical imaging,” University of Southampton, Southampton, 2018.

[41] M. Brinkmann et al., “Portable all-fiber dual-output widely tunable light source for coherent Raman imaging,” *Biomedical Optics Express,* vol. 10, no. 9, pp. 4437-4449, 2019.

[42] Y. J. Lee et al., “Characterization of three-color CARS in a two-pulse broadband CARS spectrum,” *Optics Letters,* vol. 32, no. 22, pp. 3370-3372, 2007.

[43] J. G. Porquez et al., “Spectrally-broad coherent anti-Stokes Raman scattering hyper-microscopy utilizing a Stokes supercontinuum pumped at 800 nm,” *Biomedical Optics Express,* vol. 7, no. 10, pp. 4335-4345, 2016.

[44] G. Nteroli and et al., “Developments on using supercontinuum sources for high resolution multi-imaging instruments for biomedical applications,” in *European Conferences on Biomedical Optics*, Munich, 2019.

[45] J. Y. Lee et al., “Three-color multiplex CARS for fast imaging and microspectroscopy in the entire CHn stretching vibrational region,” *Optics Express,* vol. 17, no. 25, pp. 22281-22295, 2009.

[46] C. H. Camp Jr et al., “High-speed coherent Raman fingerprint imaging of biological tissues,” *Nature photonics,* vol. 8, no. 8, pp. 627-634, 2014.

[47] Y. Lee et al., “Optimized continuum from a photonic crystal fiber for broadband time-resolved coherent anti-Stokes Raman scattering,” *Optics Express,* vol. 18, no. 5, pp. 4371-4379, 2010.

[48] R. Selm et al., “Ultrabroadband background-free coherent anti-Stokes Raman scattering microscopy based on a compact Er:fiber laser system,” *Optics Letters,* vol. 35, no. 19, pp. 3282-3284, 2010.

[49] B. Masters et al., “II.1 TWO-PHOTON EXCITATION FLUORESCENCE SPECTROSCOPY,” in *Handbook of Biomedical Nonlinear Optical Microscopy*, Oxford University Press, 2008, p. 85.

[50] A. Diaspro, Confocal and Two-Photon Microscopy: Foundations, Applications and Advances, vol. 38, Wiley-Liss, 2001, pp. 97-166.

[51] S. G. d. Costa, “Second Harmonic Generation,” in *Hyperspectral Coherent Anti-Stokes Raman Scattering (CARS) Imaging*, 2019, p. 28.

[52] S.-W. Chu and et al., “Studies of chi(2)/chi(3) tensors in submicron-scaled bio-tissues by polarization harmonics optical microscopy,” *Biophysical journal,* vol. 86, no. 6, pp. 3914-23922, 2004.

[53] I. Gusachenko et al., “Numerical simulation of polarization-resolved second harmonic microscopy in birefringent media,” *Physical Review A,* vol. 88, no. 5, p. 053811, 2013.

[54] P. Pantazis et al., “Second harmonic generating (SHG) nanoprobes for in vivo imaging,” *Proceedings of the National Academy of Sciences of the United States of America,* vol. 107, no. 33, pp. 14535-14540, 2010.

[55] T. Hellerer et al., “Spectral focusing: High spectral resolution spectroscopy with broad-bandwidth laser pulses,” *Applied Physics Letters,* vol. 85, no. 1, pp. 25-27, 2004.

[56] M. Mohseni et al., “Resolution of spectral focusing in coherent Raman imaging,” *Optics Express,* vol. 26, no. 8, pp. 10230-10241, 2018.

[57] R. Cole and et al., “Interplay of pulse bandwidth and spectral resolution in spectral-focusing CARS microscopy,” *Journal of the Optical Society of America B,* vol. 35, no. 4, pp. 842-850, 2018.

[58] L. Brückner et al., “Enhancement of coherent anti-Stokes Raman signal via tailored probing in spectral focusing,” *Optics Letters,* vol. 40, no. 22, pp. 5204-5207, 2015.

[59] A. F. Pegoraro, “Optimally chirped multimodal CARS microscopy based on a single Ti:sapphire oscillator,” *Optics Express,* vol. 17, no. 4, pp. 2984-2996, 2009.

[60] W. Langebein et al., “Coherent anti-Stokes Raman micro-spectroscopy using spectral focusing: theory and experiment,” *Journal of Raman Spectroscopy,* vol. 49, no. 7, pp. 800-808, 2009.

[61] I. Pope et al, “Simultaneous hyperspectral differential-CARS, TPF and SHG microscopy with a single 5 fs Ti:Sa laser,” *Optics express,* vol. 21, no. 6, pp. 7096-7106, 2013.

[62] E. S. Lamb et al., “Fiber optical parametric oscillator for coherent anti-Stokes Raman scattering microscopy,” *Optics letters,* vol. 38, no. 20, pp. 4154-4157, 2013.

[63] J. G. Porquez and et al., “Comparison of two photonic crystal fibers for supercontinuum-Stokes spectral-focusing-CARS hyperspectroscopy,” *OSA Continuum,* vol. 1, no. 4, pp. 1385-1399, 2018.

[64] Y. Liu et al., “Broadband nonlinear vibrational spectroscopy by shaping a coherent fiber supercontinuum,” *Optics Express,* vol. 21, no. 7, pp. 8269-8275, 2013.

[65] R. R. Alfano, The Supercontinuum Laser Source, New York: Springer, 2016.

[66] R. W. Boyd, Nonlinear optics, Amsterdam/London: Academic Press, 2003.

[67] J.-C. Diels and et al., Ultrashort Laser Pulse Phenomena : Fundamentals, Techniques, and Applications on a Femtosecond Time Scale, Elsevier Science & Technology, 2006.

[68] A. M. Weiner, "Dispersion and dispersion compensation," in *Ultrafast optics*, New Jersey, Wiley & Sons, Incl, 2009, pp. 147-151.

[69] M. C. K. Wiltshire et al., "Chiral Swiss rolls show a negative refractive index," *Journal of Physics: Condensed Matter,* vol. 21, no. 29, 2009.

[70] K. S. Kim et al., "Measurement of the nonlinear index of silica-core and dispersion-shifted fibers," *Optics Letters,* vol. 19, no. 4, pp. 257-259, 1994.

[71] G. Agrawal, "Supercontinuum generation," in *Nonlinear Fiber Optics*, Elsevier, 2013, pp. 553-602.

[72] R. R. Alfano et al., "Observation of Self-Phase Modulation and Small-Scale Filaments in Crystals and Glasses," *Physical Review Letters,* vol. 24, no. 11, pp. 592-594, 1970.

[73] F. Shimizu, "Frequency Broadening in Liquids by a Short Light Pulse," *Physical Review Letters,* vol. 19, no. 19, pp. 1097-1100, 1967.

[74] T. K. Gustafson et al., "Self-Modulation, Self-Steepening, and Spectral Development of Light in Small-Scale Trapped Filaments," *Physical Review,* vol. 177, no. 1, pp. 306-313, 1969.

[75] I. Deutsch, "Physics 531: Atomic Physics," [Online]. Available: http://info.phys.unm.edu/~ideutsch/Classes/Phys531F11/Atomic%20Units.pdf. [Accessed 2020].

[76] R. Stolen, "Nonlinearity in Fiber Transmission," *Proceedings of the IEEE ,* vol. 68, no. 10, pp. 1232 - 1236, 1980.

[77] J. Senior, Optical Fiber Communications: Principles and Practice, Harlow: Prentice-Hall, 1992.

[78] T. A. Birks et al., "Full 2-D photonic bandgaps in silica/air structures," *Electronics Letters,* vol. 31, no. 22, pp. 1941-1943, 1995.

[79] P. S. J. Russell, “Photonic-Crystal Fibers,” *Journal of Lightwave Technology,* vol. 24, no. 12, pp. 4729-4749, 2006.

[80] F. Poletti, “Nested antiresonant nodeless hollow core fiber,” *Optics Express,* vol. 22, pp. 23807-23828, 2014.

[81] C. Lin et al., “New nanosecond continuum for excited-state spectroscopy,” *Applied Physics Letters,* vol. 28, no. 4, pp. 216-218, 1976.

[82] Clarivate Analytics, “Web of Science,” [Online]. Available: http://wcs.webofknowledge.com/. [Accessed 09 09 2019].

[83] “Fiber Optics Basics,” [Online]. Available: https://www.newport.com/t/fiber-optic-basics. [Accessed 25 05 2017].

[84] A. Hartung et al., “Design of all-normal dispersion microstructured optical fibers for pulse-preserving supercontinuum generation,” *Optics Express,* vol. 19, no. 8, pp. 7742-7749, 2011.

[85] T. A. Birks et al., “Endlessly single-mode photonic crystal fiber,” *Optics Letters,* vol. 22, no. 13, pp. 961-963, 1997.

[86] D. Mogilevtsev et al., “Group-velocity dispersion in photonic crystal fibers,” *Optics Letters,* vol. 23, no. 21, pp. 1662-1664, 1998.

[87] J. M. Dudley and et al., Supercontinuum generation in optical fibers, Cambridge: University Press, 2010.

[88] J. Price et al., “UV generation in a pure-silica holey fiber,” *Applied Physics B,* vol. 77, p. 291–298, 2003.

[89] J. Limpert et al., “High-power air-clad large-mode-area photonic crystal fiber laser,” *Optics Express,* vol. 11, no. 7, pp. 818-823, 2003.

[90] K. Saitoh et al., “Chromatic dispersion control in photonic crystal fibers: application to ultra-flattened dispersion,” *Optics express,* vol. 11, no. 8, pp. 843-852, 2003.

[91] J. Herman et al., “Experimental evidence for supercontinuum generation by fission of higher-order solitons in photonic fibers,” *Physical Review Letters,* vol. 88, no. 17, p. 173901, 2002.

[92] D. Anderson et al., “Wave breaking in nonlinear-optical fibers,” *Journal of the Optical Society of America B,* vol. 9, no. 8, pp. 1358-1361, 1992.

[93] G. Agrawal, Nonlinear Fiber Optics, Academic Press, 2007.

[94] E. R. Andresen et al., “Picosecond anti-Stokes generation in a photonic-crystal fiber for interferometric CARS microscopy,” *Optics Express,* vol. 14, no. 16, pp. 7246-7251, 2006.

[95] F. Poletti et al., “Description of ultrashort pulse propagation in multimode optical fibers,” *Journal of the Optical Society of America B,* vol. 25, no. 10, pp. 1645-1654, 2008.

[96] A. F. Pegoraro, “Hyperspectral multimodal CARS microscopy in the fingerprint region,” *J. Biophotonics,* vol. 7, no. 1-2, pp. 49-58, 2014.

[97] H. Mikami, “Compact and fully collinear light source for broadband multiplex CARS microscopy covering the fingerprint region,” *Optics express,* vol. 23, no. 13, pp. 17217-17222, 2015.

[98] P. Leproux et al., “New opportunities offered by compact sub-nanosecond supercontinuum sources in ultra-broadband multiplex CARS,” *Journal of Raman Spectroscopy,* vol. 42, no. 10, pp. 1871-1874, 2011.

[99] “Biomedical Imaging using Surface-Enhanced Stimulated Raman Scattering Microscopy based on Supercontinuum Laser,” [Online]. Available: http://gtr.rcuk.ac.uk/projects?ref=EP%2FI014470%2F1. [Accessed 21 05 2017].

[100] A. B. Garcia, “Numerical Study of Highly Nonlinear Photonic Crystal Fiber with Tunable Zero Dispersion Wavelengths,” *Journal of Electromagnetic Analysis and Applications,* vol. 7, no. 5, pp. 141-151, 2015.

[101] A. Mussot et al., “Tailoring CW supercontinuum generation in microstructured fibers with two-zero dispersion wavelengths,” *Optics express,* vol. 15, no. 18, pp. 11553-11563, 2007.

[102] L. Xing, “Optimization of supercontinuum sources for ultra-broadband t-cars spectroscopy,” *Chinese Physics Letters,* vol. 28, no. 3, 2011.

[103] Karasawa et al., “Generation of intense ultrabroadband optical pulses by induced phase modulation in an argon-filled single-mode hollow waveguide,” *Optics Letters,* vol. 25, no. 3, pp. 183-185.

[104] J. M. Dudley et al., “Supercontinuum generation in photonic crystal fiber,” *Reviews of Modern Physics,* vol. 78, no. 4, p. 1135, 2006.

[105] K. M. Hilligsoe et al., “Supercontinuum generation in a photonic crystal fiber with two zero dispersion wavelengths,” *Optics Express,* vol. 12, no. 6, pp. 1045-1054, 2004.

[106] H. Tu, “Stain-free histopathology by programmable supercontinuum pulses,” *Nature Photonics,* vol. 10, no. 8, pp. 534-540, 2016.

[107] A. Volkmer et al., “Vibrational Imaging with High Sensitivity via Epidetected Coherent Anti-Stokes Raman Scattering Microscopy,” *Physical Review Letters,* vol. 87, no. 2, p. 023901, 2001.

[108] A. M. Heidt et al., “High quality sub-two cycle pulses from compression of supercontinuum generated in all-normal dispersion photonic crystal fiber,” *Optics express,* vol. 19, no. 15, pp. 873-13879, 2011.

[109] M.-L. V. Tse et al., “Supercontinuum generation at 1.06 μm in holey fibers with dispersion flattened profiles,” *Optics Express,* vol. 14, no. 10, pp. 4445-4451, 2006.

[110] D. S. Shreesha Rao et al., “Ultra-low Noise Supercontinuum Generation with Flat-near Zero All Normal Dispersion Pure Silica Fiber at GHz Reptition Rate,” in *Advanced Photonics 2018 (BGPP, IPR, NP, NOMA, Sensors, Networks, SPPCom, SOF)*, Zurich, 2018.

[111] J. Knight, “Silica fibres for supercontinuum generation,” in *Supercontinuum generation in optical fibers*, New York, Cambridge University Press, 2010.

[112] S. Demmler et al., “Generation of high quality, 1.3 cycle pulses by active phase control of an octave spanning supercontinuum,” *Optics Express,* vol. 19, no. 21, pp. 20151-20158, 2011.

[113] X. Gu et al., “Frequency-resolved optical gating and single-shot spectral measurements reveal fine,” *Optics Letters,* no. 27, p. 1174, 2002.

[114] A. B. Shafer et al., “Optimization of the Czerny–Turner Spectrometer,” *Journal of the Optical Society of America,* vol. 54, no. 7, pp. 879-887, 1964.

[115] P. O’Shea et al., “Increased-bandwidth in ultrashort-pulse measurement using an angle-dithered nonlinear-optical crystal,” *Optics Express,* vol. 7, no. 10, pp. 342-349, 2000.

[116] S. Toenger et al., “Interferometric autocorrelation measurements of supercontinuum based on two-photon absorption,” *Journal of the Optical Society of America B,* vol. 36, no. 5, pp. 1320-1326, 2019.

[117] A. E. Siegman, Lasers, 1986.

[118] H. Linnenbank et al., “A robust and rapidly tunable light source for SRS/CARS microscopy with low intensity noise,” *opticsjournal.net,* 2019.

[119] A. M. Weiner, “Ultrafast optical pulse shaping: A tutorial review,” *Optics Communications,* vol. 284, no. 15, pp. 3669-3692, 2011.

[120] R. L. Fork et al., “Compression of optical pulses to six femtoseconds by using cubic phase compensation,” *Opticss Letters,* vol. 12, no. 7, pp. 483-485, 1987.

[121] “Prism Compressor for Ultrashort Laser Pulses,” Technology and Applications Center Newport Corporation, [Online]. Available: https://www.newport.com/medias/sys_master/images/images/h25/h7f/8797242818590/Prism-Compressor-for-Ultrashort-Laser-Pulses-App-Note-29.pdf. [Accessed 21 05 2017].

[122] H. Lin et al., “Spectroscopic stimulated Raman scattering imaging of highly dynamic specimens through matrix completion,” *Light: Science & Applications,* vol. 7, p. 17179, 2018.

[123] J. Lancis et al., “Chromatic compensation of broadband light diffraction: ABCD-matrix approach,” *JOSA A,* vol. 21, no. 10, pp. 1875-1885, 2004.

[124] J.-X. Cheng et al., “An Epi-Detected Coherent Anti-Stokes Raman Scattering (E-CARS) Microscope with High Spectral Resolution and High Sensitivity,” *The Journal of Physical Chemistry B,* vol. 105, no. 7, pp. 1277-1280, 2001.

[125] K. Herdzik et al, “Comparison of SC fibers for fs Ti:Sapphire based hyperspectral CARS microscopy,” in *2019 Conference on Lasers and Electro-Optics Europe and European Quantum Electronics Conference*, Munich, 2019.

[126] Newport, “femto WHITE CARS specification,” [Online]. Available: https://www.newport.com/f/supercontinuum-fiber-module-femtowhite. [Accessed 14 03 2020].

[127] N. Photonics, “NKT-1050-NEG1 Nonlinear Crystal Fiber,” [Online]. Available: http://ainnotech.com/ainnotech/pdf/04/1_3/6NKT_NL-1050-NEG-1_Nonlinear%20Photonic%20Crystal%20Fiber.pdf. [Accessed 14 03 2020].

[128] CGCRI, *Fiber specification,* 2016.

[129] L. Xu et al., Yb-fiber amplifier pumped idler-resonant PPLN optical parametric oscillator producing 90 femtosecond pulses with high beam quality, Applied Physics B, 2014.

[130] R. Head et al., “Supercontinuum Generation with femtosecond pulse fiber amplified VECSELs,” *SPIE LASE. International Society for Optics and Photonics,* pp. 860608-860608, 2013.

[131] A. A. Amorim et al., “Sub-two-cycle pulses by soliton self-compression in highly nonlinear photonic crystal fibers,” *Optics letters,* vol. 34, no. 24, pp. 3851-3853, 2009.

[132] M. Falconieri et al., “Characterization of supercontinuum generation in a photonic crystal fiber for uses in multiplex CARS microspectroscopy,” *Journal of Raman Spectroscopy,* 2019.

[133] A. Loredo-Trejo et al., “Polarization Modulation Instability in All-Normal Dispersion Microstructured Optical Fibers With Quasi-Continuous Pump,” *IEEE Photonics Journal,* 2019.

[134] S. R. Domingue et al., “Overcoming temporal polarization instabilities from the latent birefringence in all-normal dispersion, wave-breaking-extended nonlinear fiber supercontinuum generation,” *Optics Express,* vol. 21, no. 11, pp. 13305-13321, 2013.

[135] D. Dobrakowski et al, “Birefringence of nonlinearity in all-normal dispersion photonic crystal fibers,” *Journal of Optics,* 1 11 2019.

[136] K. Herdzik et. al, “Multimodal spectral focusing CARS and SFG microscopy with a tailored coherent continuum from a microstructured fiber,” *Applied Physics B,* no. 126, April 2020.

[137] J. Porquez et al., “Brighter CARS hypermicroscopy via spectral surfing of a Stokes supercontinuum,” *Optics Letters,* vol. 42, no. 12, pp. 2255-2258, 2017.

[138] B. Li et al., “Dual/differential coherent anti-Stokes Raman scattering module for multiphoton microscopes with a femtosecond Ti:sapphire oscillator,” *J. Biomed. Opt.,* vol. 18, no. 6, p. 066004, 2013.

[139] A. Heidt et al., “Limits of coherent supercontinuum generation in normal dispersion fibers,” *Journal of the Optical Society of America B,* vol. 34, no. 4, pp. 764-775, 2017.

[140] T. Pologruto et al., “ScanImage: Flexible software for operating laser scanning microscopes,” *BioMedical Engineering OnLine,* p. 13, 2003.

[141] Y. Liu et al., “Broadband CARS spectral phase retrieval using a time-domain Kramers–Kronig transform,” *Optics Letters,* vol. 34, no. 9, pp. 1363-1365, 2009.

[142] C.-S. Liao et al., “Stimulated Raman spectroscopic imaging by microsecond delay-line tuning,” *Optica,* vol. 3, no. 12, pp. 1377-1380, 2016.

[143] Schott North America, “Optical Glass Data Sheets,” 2014. [Online]. Available: https://www.schott.com/advanced_optics/us/abbe_datasheets/schott-datasheet-all-us.pdf. [Accessed 2018].

[144] H. A. Rinia et al., “Quantitative Label-Free Imaging of Lipid Composition and Packing of Individual Cellular Lipid Droplets Using Multiplex CARS Microscopy,” *Biophysical Journal,* vol. 95, no. 10, pp. 4908-4914, 2008.

[145] T. Khan et al., “Metabolic Dysregulation and Adipose Tissue Fibrosis: Role of Collagen VI,” *Molecular and Cellular Biology,* vol. 29, no. 6, p. 1575, 2009.

[146] Y. Urasaki et al., “Imaging Immune and Metabolic Cells of Visceral Adipose Tissues with Multimodal Nonlinear Optical Microscopy,” *PLOS ONE,* vol. 7, no. 6, p. e38418, 2012.

[147] S. Huang et al., “Two-photon fluorescence spectroscopy and microscopy of NAD(P)H and flavoprotein,” *Biophysical journal,* vol. 82, no. 5, pp. 2811-2825, 2002.

[148] Y. Cao et al., “Three-dimensional volume fluorescence-imaging of vascular plasticity in adipose tissues,” *Molecular metabolism,* vol. 14, pp. 71-81, 2018.

[149] N. Alkhouli et al., “The mechanical properties of human adipose tissues and their relationships to the structure and composition of the extracellular matrix,” *American Journal of Physiology-Endocrinology and Metabolism,* vol. 305, no. 12, pp. E1427-E1435, 2013.

[150] C. Di Napoli and et al., “Quantitative Spatiotemporal Chemical Profiling of Individual Lipid Droplets by Hyperspectral CARS Microscopy in Living Human Adipose-Derived Stem Cells,” *Analytical Chemistry,* vol. 88, no. 7, pp. 3677-3685, 2016.

[151] A. Divoux and et al., “Fibrosis in Human Adipose Tissue: Composition, Distribution, and Link With Lipid Metabolism and Fat Mass Loss,” *Diabetes,* vol. 59, no. 11, p. 2817, 2010.

[152] Y. Lee et al., “Quantitative Image Analysis of Broadband CARS Hyperspectral Images of Polymer Blends,” *Analytical Chemistry,* vol. 83, no. 7, pp. 2733-2739, 2011.

[153] L. Zada et al., “Fast microplastics identification with stimulated Raman scattering microscopy,” *Journal of Raman Spectroscopy,* vol. 49, no. 7, pp. 1136-1144, 2018.

[154] G. W. H. Wurpel et al., “Imaging orientational order and lipid density in multilamellar vesicles with multiplex CARS microscopy,” *Journal of Microscopy,* vol. 218, pp. 37-45, 2005.

[155] Y. Liu et al., “Suppressing Short-Term Polarization Noise and Related Spectral Decoherence in All-Normal Dispersion Fiber Supercontinuum Generation,” *Journal of Lightwave Technology,* vol. 33, no. 9, pp. 1814-1820, 2015.

[156] L. Hooper et al., “Coherent supercontinuum generation in photonic crystal fiber with all-normal group velocity dispersion,” *Optics Express,* vol. 19, no. 6, pp. 4902-4907, 2011.

[157] K.-C. Li et al., “Simple approach to three-color two-photon microscopy by a fiber-optic wavelength convertor,” *Biomedical Optics Express,* vol. 7, no. 11, pp. 4803-4815, 2016.

[158] X. C. et al., “Multiphoton fluorescence excitation: New spectral windows for biological nonlinear microscopy,” *PNAS,* vol. 93, no. 10, pp. 10763-10768, 1996.

[159] T. S. et. al., “Effect of pulse duration on two-photon excited fluorescence and second harmonic generation in nonlinear optical microscopy,” *Journal of Biomedical Optics,* vol. 11, no. 2, 2006.

[160] G. Rasskazov et al., “Mitigating self-action processes with chirp or binary phase shaping,” *Optics Letters,* vol. 41, no. 1, pp. 131-134, 2016.

[161] J. J. Field et al., “Quartic-phase-limited grism-based ultrashort pulse shaper,” *Optics Letters,* vol. 32, no. 21, pp. 3101-3103, 2007.

[162] Y. Shaked et al., “The Prism-Pair: Simple Dispersion Compensation and Spectral Shaping of Ultrashort Pulses,” *International Journal of Experimental Spectroscopic Techniques,* vol. 1, no. 2, 2016.

[163] A. Nag et al., “Solvent effect on two-photon absorption and fluorescence of rhodamine dyes,” *Journal of Photochemistry and Photobiology A: Chemistry,* vol. 206, no. 2, pp. 188-197, 2009.

[164] S. Li et al., “Conjugated-Polymer-Based Red-Emitting Nanoparticles for Two-Photon Excitation Cell Imaging with High Contrast,” *Langmuir,* vol. 30, no. 26, pp. 7623-7627, 2014.

[165] M. Ghosh et al., “Fluorescence self-quenching of tetraphenylporphyrin in liquid medium,” *Journal of Luminescence,* vol. 141, pp. 87-92, 2013.

[166] S. Prahl and et al., Oregon Medical Laser Centre, [Online]. Available: https://omlc.org/spectra/PhotochemCAD/html/083.html. [Accessed 2019].

[167] AAT Bioquest, “Spectrum viewer,” [Online]. Available: https://www.aatbio.com/spectrum/Cy5_cyanine_5. [Accessed 30 September 2019].

[168] N. Mataga and et al., “Solvent Effects upon Fluorescence Spectra and the Dipolemoments of Excited Molecules,” *Bulletin of the Chemical Society of Japan,* vol. 29, no. 4, pp. 465-470, 1956.

[169] P. Cheng et al., “Enhancement of ZnO light emission via coupling with localized surface plasmon of Ag island film,” *Applied Physics Letters,* vol. 92, no. 041119, 2008.

[170] G. Agrawal, “Third Order Dispersion,” in *Nonlinear Fiber Optics*, John Wiley & Sons, Inc., 2013, p. 71.

[171] L. Arissian et al., “Carrier to envelope and dispersion control in a cavity with prism pairs,” *Physical Review A,* vol. 75, no. 1, 2007.

[172] T. Monfort, Interviewee, *Discussions on compression of pulses.* [Interview]. 2018.

[173] C. W. Freudiger et al., “Stimulated Raman scattering microscopy with a robust fibre laser source,” *Nature Photonics,* vol. 8, pp. 153-159, 2014.

[174] J. Price et al., “Mid-IR Supercontinuum Generation From Nonsilica Microstructured Optical Fibers,” *IEEE Journal of Selected Topics in Quantum Electronics,* vol. 13, no. 3, pp. 738-749, 2007.

[175] A. Ravagli et al., “Ga-La-S-Se glass for visible and thermal imaging,” *Advanced Optical Technologies,* vol. 6, no. 2, pp. 131-136, 2017.

[176] S. O. Konorov et al., “Laser ablation of dental tissues with picosecond pulses of 1.06-μm radiation transmitted through a hollow-core photonic-crystal fiber,” *Applied Optics,* vol. 43, no. 11, pp. 2251-2256, 2004.

[177] I. B. Gonzalo et al., “All-Fiber-Based All-Normal Dispersion Supercontinuum Source Using a Femtosecond Fiber Laser with Hollow-Core Fiber Pulse Compression,” in *Advanced Photonics 2018 (BGPP, IPR, NP, NOMA, Sensors, Networks, SPPCom, SOF)*, Zurich, 2018.

[178] J. Trägårdh et al., “Label-free CARS microscopy through a multimode fiber endoscope,” *Opt. Express 27,* pp. 30055-30066, 2019.

[179] X. Chen and et al., “High coupling efficiency technology of large core hollow-core fiber with single mode fiber,” *Optics Express,* vol. 27, no. 23, pp. 33135-33142, 2019.

[180] M. V. Padalkar et al., “Wavelength-dependent penetration depth of near infrared radiation into cartilage.,” *Analyst,* vol. 140, no. 7, pp. 2093-2100, 2015.

[181] G. Agrawal, “Optical Wave Breaking,” in *Nonlinear Fiber Optics*, Elsevier Inc., 2013, pp. 102-105.

[182] A. F. Pegoraro et al., “All-fibre CARS microscopy of live cells,” *Opics express,* vol. 17, no. 23, pp. 20700-20706, 2009.

[183] N. A. Mortensen, “Effective area of photonic crystal fibers,” *Optics express,* vol. 10, no. 7, pp. 341-348, 2002.

[184] C. Xia, “Mid-Infrared Supercontinuum Laser System and its Biomedical Applications,” 2009. [Online]. Available: https://deepblue.lib.umich.edu/handle/2027.42/62250. [Accessed 23 05 2017].

[185] D. Long, The Raman Effect, John Wiley & Sons, Ltd, 2002.

[186] W. M. Tolles et al., “A review of the theory and application of coherent anti-Stokes Raman spectroscopy (CARS),” *Applied Spectroscopy,* vol. 31, no. 4, pp. 253-271, 1977.

[187] H. P. T. Nguyen and et al., “Highly coherent supercontinuum generation in chalcogenide all-solid hybrid microstructured optical fibers (JM5A.18),” in *Laser Congress 2019 (ASSL, LAC, LS&C)*, 2019.

[188] N. S. Trivedi and et al., “Quantitative Analysis of Pc 4 Localization in Mouse Lymphoma (LY-R) Cells via Double-label Confocal Fluorescence Microscopy,” *Photochemistry and Photobiology,* vol. 71, no. 5, pp. 634-639, 2007/2000.

[189] P. V. Kelkar and et al., “Time-domain optical sensing,” *Electronics Letters,* vol. 35, no. 19, pp. 1661-1662, 1999.

[190] B. J. Eggleton and et al., “Chalcogenide photonics,” *Nature Photonics,* vol. 5, pp. 141-148, 2011.

[191] A. Ellis and et al., “RotaryFROG: geometry for measuring amplitude and phase of weak broadband laser pulses,” *Optics Letters,* vol. 34, no. 4, pp. 404-406, 2009.

[192] N. Firestone and et al., “Laser Focus World,” 1 June 2019. [Online]. Available: https://www.laserfocusworld.com/lasers-sources/article/14035451/resolving-damage-ambiguity-and-laserinduced-damage-threshold-lidt-complications. [Accessed 31 August 2019].

[193] M. W. Davidson et al., “Optical Microscopy,” *Encyclopedia of Imaging Science and Technology,* 2002.

[194] J. G. Fujimoto et al., “Optical coherence tomography: an emerging technology for biomedical imaging and optical biopsy,” *Neoplasia (New York, N.Y.),* vol. 2, no. 1-2, pp. 9-25, 2000.

[195] K. Isobe et al., “Multi-Spectral Two-Photon Excited Fluorescence Microscopy Using Supercontinuum Light Source,” *Japanese Journal of Applied Physics,* vol. 44, no. 4, pp. L167-L169.

[196] P. Maker et al., “Study of Optical Effects Due to an Induced Polarization Third Order in the Electric Field Strength,” *Physical Review,* vol. 137, no. 3A, pp. A801-A818, 1965.

[197] J. T. Manassah et al., “Spectral distribution of an ultrafast supercontinuum laser source,” *Physics Letters A,* vol. 107, no. 7, pp. 305-309, 1985.

[198] I. Rocha-Mendoza et al., “Coherent anti-Stokes Raman microspectroscopy using spectral focusing with glass dispersion,” *Applied Physics Letters,* vol. 93, no. 20, p. 201103, 2008.

[199] C. Steuwe et al., “Surface Enhanced Coherent Anti-Stokes Raman Scattering on Nanostructured Gold Surfaces,” *Nano Letters,* vol. 11, no. 12, pp. 5339-5343, 2011.

[200] G. Yang et al., “Spectral broadening of ultrashort pulses in a nonlinear medium,” *Optics Letters,* vol. 9, no. 11, pp. 510-512, 1984.

[201] K. C. Zhou et al., “Optical coherence refraction tomography,” *Nature Photonics,* 2019.

[202] G. D. Ly et al., “The mitochondrial membrane potential (Δψm) in apoptosis; an update,” *Apoptosis,* no. 8, p. 115–128, 2003.

[203] D. F. Baxter et al., “A Novel Membrane Potential-Sensitive Fluorescent Dye Improves Cell-Based Assays for Ion Channels,” *Journal of Biomolecular Screening,* vol. 7, no. 1, pp. 79-85, 2002.

[204] U. Gerckens et al., “Optical Coherence Tomography (OCT),” *Herz,* vol. 28, no. 6, p. 496–500, 2003.

[205] W. Liu et al., “General analysis of SRS-limited high-power fiber lasers and design strategy,” *Optics Express,* vol. 24, no. 23, pp. 26715-26721, 2016.

[206] A. Faruqi et al., “CCD detectors in high-resolution biological electron microscopy.,” *Quarterly Reviews of Optics,* vol. 33, no. 1, pp. 1-27, 2000.